الجمهورية الجزائرية الديمقراطية الشعبية

People’s Democratic Republic of Algeria
Ministry of Higher Education and Scientific Research

SETIF 1 UNIVERSITY- FERHAT ABBAS

FACULTY OF TECHNOLOGY

Thesis submitted to the Department of Electronics

for the award of the *Doctorate* Degree

Field: Science and Technology

Specialization: Telecommunications **Option: Telecommunication Systems**

By

Ms. Labiba CHIOUKH

THESIS TITLE

Modeling and Confrontation of Dielectric Mixing Laws through Numerical Simulation and Experimental Characterization of Titanate-Based Composite Materials

Defended on 08 / 04 / 2026 before the Jury:

Nourredine AMARDJIA	**Professor**	**Univ. Ferhat Abbas Setif 1**	**President**
Nacerdine BOUZIT	**Professor**	**Univ. Ferhat Abbas Setif 1**	**Thesis Supervisor**
Habib KHOUNI	**M.C.A**	**Univ. Ferhat Abbas Setif 1**	**Co-supervisor**
Nacerdine BOUROUBA	**Professor**	**Univ. Ferhat Abbas Setif 1**	**Examiner**
Miloud BENTOUMI	**M.C.A**	**Univ. M’sila**	**External Examiner**
Haddi BAKHTI	**M.C.A**	**Univ. M’sila**	**External Examiner**

Academic Year

2025-2026

Laboratory of Scientific Instrumentation "LIS"

Acknowledgments

﴿ وَإِذْ تَأَذَّنَ رَبُّكُمْ لَئِن شَكَرْتُمْ لَأَزِيدَنَّكُمْۖ وَلَئِن كَفَرْتُمْ إِنَّ عَذَابِي لَشَدِيدٌ ﴾

[إبراهيم: 7]

First and foremost, I want to express my deepest gratitude to Allah, the Most Merciful, the Most Compassionate. He alone granted me the strength to keep going during difficult times, the patience when I was overwhelmed, and the clarity when everything felt uncertain. Without His guidance, mercy, and support, none of this would have been possible.

This journey officially began in April 2021, the day I was honored to pass the doctoral entrance exam. Since then, every step has been a mixture of challenges, learning, and unforgettable human and scientific experiences.

I would like to acknowledge **Mr. Nacerdine Bouzit** *for proposing the research topic of this doctoral work. I also acknowledge* **Mr. Habib Khouni** *for his scientific input, notably for suggesting the idea that resulted in the publication of a research article related to this thesis. I sincerely thank them for their valuable advice and constant availability. Their respective contributions are duly recognized.*

I am also grateful to **Mr. Nacerdine Bourouba** *for being available to answer my theoretical questions, providing clear and precise explanations that helped improve my understanding of the theoretical foundations of this research.*

I would like to express my sincere thanks to **Mr. Nourredine Amardjia** *for serving as the chair of the jury for this thesis.*

My thanks also go to the members of the thesis jury, **Mr. Miloud Bentoumi** and **Mr. Haddi Bakhti**, who honored me by agreeing to evaluate this work and for their time, constructive feedback, and presence.

To my **parents, Yazid and Chafiaa**, thank you from the bottom of my heart. Everything I have achieved is because of you. Your prayers, your encouragement, and your visible and invisible sacrifices carried me through. You are the foundation of my strength and motivation.

In 2022, I worked on several conferences, contributed to the preparation of a scientific paper, and co-supervised the projects of two Master's students alongside my colleagues from the laboratory, **Dr. Rabeh Delfouf, Dr. Abdelhalim Brahimi**, and **Dr. Djahida Djouada**, whom I thank for their support. These years were an important step in my research journey, helping me develop both my scientific and teamwork skills.

In November 2023, I had the opportunity to complete a research internship in Spain at the University of Zaragoza. I am especially grateful to **Mr. Juan Pablo Martinez**, who welcomed me into his laboratory and made this experience academically enriching and personally rewarding.

On a more personal note, I spent five years in the university residence with two incredible girls, **Rebeiha Allaoua** and **Nedjma Boulelli** who became true friends. We shared many joyful, stressful, and emotional moments together. I especially want to thank my friend **Nedjma Boulelli** for her constant support, encouragement, and for always being there during challenging times, which made these years much more meaningful and memorable.

During this time, I also worked as a part-time TD instructor in the **ST department** for three years. I am sincerely grateful to the professors there, who welcomed me as a full member of the team rather than just a temporary teacher.

I also wish to express my appreciation to those who assisted me with practical matters: in particular, **Dr. Charaf Eddine Chelloug**, for his constant support and help, especially with currency exchange, a thoughtful gesture that greatly facilitated the purchase of software necessary for my research.

Pr. Ghalia Gaber, from Al-Azhar University in Egypt, a remarkable woman who supported and advised me during difficult moments. Your kindness and encouragement gave me strength.

Finally, my deepest love and thanks go to my sister **Bochra**, my brothers **Ala and Mohammed**, my best friend **Amel**, and my little niece, **sadja**, the light of our family. Thank you for being who you are and for your presence in my life.

This thesis is the result of a long journey filled with effort, challenges, and faith. To every person who crossed my path and left a mark, thank you from the depths of my soul.

"This is not the end, just the beginning. But for today... I did it."

Dedications

To my parents; whose
Foundation was loam,
Doctorate was labor,
Science was wisdom,
And greatest creation was love.

This achievement, from beginning to end, belongs to you.

Your daughter, Labiba

TABLE OF CONTENTS

Acknowledgments

Dedications

LIST OF FIGURES

1 MODELING THE DIELECTRIC PROPERTIES OF COMPOSITE MATERIALS

2 ELECTROMAGNETIC CHARACTERIZATION OF DIELECTRIC MATERIALS

3 EXPERIMENTAL RESULTS AND MODELING OF BINARY AND TERNARY COMPOSITES

4 CHARACTERIZATION AND MODELING OF DIELECTRIC COMPOSITES BY FINITE ELEMENT METHOD

LIST OF TABLES

NOMENCLATURE

CTC	Capacitance Temperature Coefficient
MG	Maxwell-Garnett
SBG	Bruggeman
EMA	Effective Medium Approximation
TDR	Time-Domain Reflectometry
TDS	Time Domain Spectroscopy
TEM	Transverse Electric magnetic
TE	Transverse Electric
TM	Transverse Magnetic
MTB	Microwave Test Bench
FEM	Finite Element Method
RE	Resin Epoxy
BT	Barium Titanate
CT	Calcium Titanate
FE	Manganese-Zinc Ferrite
WR	Rectangular Waveguide
N	Normal Distribution
LN	Log-normal distribution
R	Rayleigh distribution
RC	Resin-Ceramic composites

General Introduction

The study of composite materials has become a major research focus over the past several decades due to their ability to provide physicochemical and electrical properties tailored to the specific requirements of diverse applications [1]. A composite material typically consists of two or more distinct phases, which may be arranged randomly or in an ordered structure [2,3]. The constituent phases are selected according to the desired application, with criteria including electrical, thermal, and mechanical properties.

Among these materials, ferroelectric polymer-ceramic composites with high dielectric permittivity [4,5] have received particular attention. These composites are widely used as structural materials due to their excellent dielectric properties across a broad frequency range, including microwaves. Additionally, they are considered promising candidates for electromagnetic wave absorbers, exploiting their ability to attenuate electromagnetic energy, a property strongly dependent on the concentration, size, and spatial distribution of the ceramic inclusions within the polymer matrix.

Effective permittivity is a complex dielectric property that describes the response of a material to an applied electric field. It depends not only on the intrinsic properties of the constituent phases, but also on the distribution, arrangement, orientation, and shape of the inclusions dispersed within the matrix. To meet current scientific and industrial requirements, significant effort is being devoted to the development of composite materials with higher effective permittivities, suitable for specific applications such as telecommunications [6,7], electromagnetic compatibility, aerospace, and microwave devices.

Since the advent of modern electromagnetism, accurately predicting the dielectric response of heterogeneous composites has remained a significant challenge. A variety of analytical models have been proposed in the literature since the early developments of post-Maxwellian electromagnetism, with varying degrees of success [8–12]. Most of these models adopt a quasi-static approximation, in which the polarization properties of the material are analyzed under the interaction of a long-wavelength electromagnetic field. The theoretical description of electromagnetic wave propagation in heterostructures is inherently complex due to the multi-scale nature of local fluctuations, both spatial and temporal, associated with material inhomogeneities. Nevertheless, under the long-wavelength approximation, where small-scale variations are neglected, the concept of an effective medium becomes well-defined, allowing the dielectric response of the heterogeneous system to be represented as an average over a representative volume of the material [13].

Historically, the development of models for composite permittivity can be categorized into several stages. Initially, researchers proposed phenomenological or empirical “mixing laws,” which express the effective permittivity of a heterogeneous mixture as a function of the permittivities and volume fractions of its constituent phases. Although these laws provide simple estimates, they fail to capture the underlying physics of interactions between inclusions or between inclusions and the matrix, and they provide limited information regarding the microstructural characteristics of the material. Consequently, their validity is generally restricted to dilute systems, and they are often not transferable between different composite systems.

A subsequent class of models, grounded in electrodynamics, introduced theoretical formulations based on the concepts of local and mean fields. Notably, the Maxwell-Garnett (MG) and Bruggeman (SBG) approaches provided a first-principles framework to overcome the limitations of purely empirical mixing laws. Between the 1960s and 1980s, concepts from statistical physics were incorporated to describe more accurately the dielectric behavior of dielectric/conductor mixtures. In such systems, abrupt transitions in conductivity are observed at specific particle concentrations, known as critical percolation thresholds. The application of scaling laws and critical exponents enables detailed characterization of the variations in permittivity and conductivity near these thresholds. However, these advanced models are often challenging to validate experimentally, as they require a large number of measurements in the vicinity of the critical concentration and detailed information on the morphology of the composite.

In parallel, during these same decades, methods emerged that define limits not as a precise evaluation of the actual quantities, but as an interval within which the values of these quantities are permissible. More recently, numerical electromagnetism methods based on Monte Carlo methods, finite elements… etc., have appeared. Given that it is impossible to conduct an exact electromagnetic study for most heterogeneous materials of a random type, for which the spatial distribution of phases is described by probabilistic laws, because this would require knowledge of the local electric field at every point of the material (and in general, the details of the microscopic arrangement of the various constituents are impossible to know precisely), only an approach in terms of moments is relevant. Moreover, even if it were possible to know the morphology of the material "exactly," the analytical calculation would be impossible to perform. However, a number of theoretical approaches, based on simplifications or approximations, do exist. From an electromagnetic transport perspective, this type of modeling is highly dependent on the ratio between a typical inclusion size and the electromagnetic wavelength. The fundamental assumption is that this typical size is much smaller than the wavelength or any other absorption scale, such as the skin thickness. The effective permittivity is then the permittivity of a hypothetical homogeneous material that behaves identically to the real heterogeneous material with respect to electromagnetic wave transport. The principle of the existence of an effective permittivity is absolutely fundamental, as it underlies much work on the electromagnetic modeling of mixtures using numerical approaches [13,14].

The introduction of numerical computation methods, such as the finite element method (FEM), which forms the methodological basis of our study, has profoundly transformed the analysis of composite materials. These approaches allow us to obtain precise results that serve to verify the validity of mixing laws, identify their limitations, and, when necessary, propose improvements or new formulations better suited to complex composites.

Computational electromagnetism has also clarified the application domains of analytical models and produced useful results for optimizing materials according to specific needs. Furthermore, these methods make it possible to explore composite structures that are difficult, or even impossible, to fabricate experimentally, thus paving the way for the design of innovative materials.

Advances in the numerical modeling of effective dielectric permittivity show that these techniques can provide estimates closer to real values than those obtained from classical mixing laws. Rooted in applied mathematics, numerical methods aim to solve complex physical models in an approximate but controlled manner. Their use in the study of composites offers significant time and cost savings, while also enabling detailed analysis of the effects related to the shape, distribution, and concentration of inclusions.

Previous research conducted at the Scientific Instrumentation Laboratory (LIS) has primarily focused on studying the dielectric behavior of composite materials under quasi-static and microwave conditions, relying on experimental characterization methods using various measurement setups.

Within this framework, the present thesis marks a significant methodological shift by introducing, for the first time within the laboratory, a numerical modeling approach based on the finite element method (FEM). This approach constitutes a complementary and strategic step both before and after experimentation, enabling a better understanding of the physical mechanisms governing the dielectric behavior of composites, while offering significant time and cost savings from both a scientific and industrial perspective.

The research focuses primarily on the study of the dielectric properties, and more specifically the effective permittivity, of binary dielectric composites based on epoxy resin and titanate-type ceramic inclusions. The analysis is conducted using a two-dimensional numerical model, performed under quasi-static conditions, with the finite element method. Particular attention is paid to the realistic representation of the composite microstructure, notably through the numerical generation of random distributions of ellipsoidal inclusions.

The main objective of this thesis is to develop a comprehensive numerical model to analyze the influence of the composite microstructure on its dielectric behavior. To this end, the impact of several key parameters is systematically studied, such as the permittivity of the inclusions, the surface fraction, the particle size, and their statistical distribution within the matrix. This approach aims to highlight the relationships between the microstructure and the effective permittivity of the composite material.

The results obtained through numerical simulation are then compared with available experimental data and with predictions derived from classical and modified dielectric mixing laws. This comparison makes it possible to evaluate the domains of validity of these theoretical models and to highlight the interest of advanced numerical approaches as a reference tool for predicting the dielectric behavior of composite materials.

This thesis is structured in four main parts.

The first part presents a literature review of the fundamental concepts necessary for understanding the dielectric properties of heterogeneous materials. It aims to establish the theoretical framework for composites and the models describing their electromagnetic behavior.

The second part describes the experimental characterization methods applied to two types of composites: binary and ternary. Two techniques are implemented: X-band rectangular waveguide measurement and time-domain reflectometry. This part also introduces the finite element method used to calculate the effective permittivity of composite materials.

The third part is devoted to the experimental results obtained at microwave frequencies. The measured electrical properties, particularly the dielectric permittivities, are analyzed and compared to the predictions provided by various theoretical mixing laws.

The fourth part presents the results of the numerical simulations. Which is based on a quasi-static model of several binary composites and examines the influence of the distribution, concentration, and size of the particles included in the matrix on the material's effective permittivity. A global comparison is then established between all the cases studied, by comparing the permittivities obtained with two categories of mixing laws: classical laws that do not take microstructure into account, and laws that explicitly incorporate this microstructure.

Finally, the thesis concludes with a synthesis of the main results and contributions of this work.

CHAPTER

1 Modeling the Dielectric Properties of Composite Materials

1.1 Introduction

Dielectric and composite materials play a fundamental role in the development of modern technologies, particularly in the fields of electrical engineering, electronics, and telecommunications. Their role extends beyond electrical insulation, as they actively participate in the control, modulation and storage of electrostatic energy within numerous devices such as capacitors, antennas, transmission lines, and integrated circuits. Understanding the dielectric behavior of a material is therefore essential for designing high-performance, reliable components adapted to the constraints of high-frequency, high-voltage, or miniaturized applications. This behavior is closely dependent on the chemical nature, crystalline structure, microstructure, and interfaces present within the material, which determine how it reacts to an external electrical field by influencing its polarization, and consequently, its permittivity.

However, the study of dielectric composites cannot be limited to a single scale of analysis, as the electrical and electrostatic phenomena that occur result from complex interactions linking several levels of organization. At the atomic and molecular scale, electronic and ionic polarization is governed by the polarizability of elementary entities. At the mesoscopic scale, microstructure and local field affects appear, related to the distribution and geometry of phases in a heterogeneous material. Finally, at the macroscopic scale, these interactions translate into observable global properties, such as effective permittivity, dielectric losses, and energy storage capacity.

Thus, a multiscale approach is essential to link microscopic phenomena to the measurable macroscopic response. This integrated understanding not only explains the intrinsic behavior of dielectric materials but also enables the design and optimization of functional composites whose performances can be tailored to specific technological needs. This chapter is devoted to the study of the fundamental principles governing the polarization of dielectric materials. It first presents the basic definitions and essential properties of dielectric media, then develops the microscopic and macroscopic notions of polarization, before addressing the electrostatic equations and local field models, prerequisites necessary for understanding the mixing laws describing heterogeneous media.

1.2 Definition and Fundamental Principles

1.2.1 Dielectrics

A dielectric material is essentially a non-conductive medium, characterized by the absence or very low density of free charges. Its fundamental property lies in its ability to become polarized under the influence of an electric field, that is, to induce a limited relative displacement of the bound charges within its atomic or molecular structure [15-18]. This polarization allows dielectrics to temporarily store electrostatic energy and to locally modify the distribution of the electric field, a property described by their dielectric permittivity.

To better understand the concept and behavior of dielectric materials, it is common to study them using the parallel-plate capacitor model, which serves as the reference system for analyzing their electrical properties. A capacitor consists of two parallel conducting plates with the same geometry and identical surface area, separated by a dielectric medium. When a voltage is applied between the two electrodes, an electric field is created inside the capacitor, allowing the storage of electrostatic energy [19].

The nature of the dielectric material interposed between the plates depends on the desired properties: it can be air, mica, plastic, glass, Teflon, or ferroelectric materials. The capacitance C of a parallel-plate capacitor, representing the quantity of electric charge Q stored per unit voltage U, is expressed by the relation:

$$C=\varepsilon\frac{S}{d} \tag{1.1}$$

where S and d denote respectively the surface area of the plates and the distance between them, and ε is the permittivity of the dielectric material.

Equation (1.1) shows that the stored charge depends on:

a) the nature of the dielectric: the higher the permittivity, the greater the capacitance of the capacitor;

b) Capacitor geometry: the ratio between the plate area and the dielectric thickness.

The development of new capacitors aims to optimize these two parameters. In a context of high component integration, the objective is to increase the volumetric capacitance, either by increasing the material permittivity or by reducing the dielectric layer thickness [20,21].

Although often considered electrical insulators, dielectric materials exhibit residual conduction due to impurities and environmental conditions, resulting in dielectric losses that depend, in particular, on the frequency of the applied field, the temperature, and the material's microstructure. These characteristics directly determine their performance in electrotechnical devices, electronic circuits, and energy storage systems.

1.2.2 Composites

Many materials used in modern technologies have a non-homogeneous structure; they are called composites. By definition, a composite material results from the combination of two or more constituents of different natures, combined in such a way as to obtain a material whose overall properties surpass those that each component could offer individually [22].

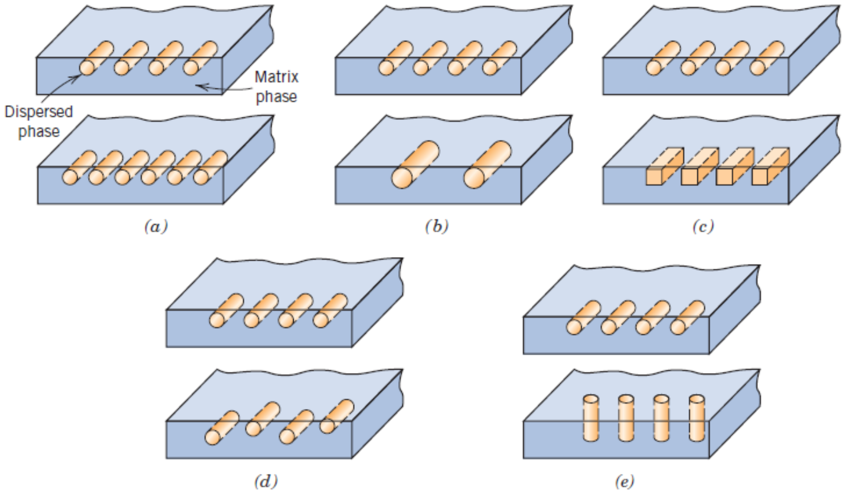

Figure 1.1: Schematic illustration of the geometrical and spatial features of dispersed-phase particles that affect composite properties: *(a)* concentration, *(b)* size, *(c)* shape, *(d)* distribution, *(e)* orientation [23].

Most composites consist of two main phases:

- a matrix, a continuous phase that ensures the cohesion of the whole,
- and a dispersed phase, generally discontinuous, which gives the composite certain specific properties.

The performance of a composite material depends both on the intrinsic properties of each phase, their relative proportions, and the geometry of the dispersed phase, that is, the shape, size, distribution, and orientation of the particles or fibers it contains (illustrated in Figure 1.1).

1.3 Microscopic and Macroscopic Concepts of Polarization

1.3.1 Electric Dipole and Dipole Moment

At the microscopic scale, the fundamental entity that describes the response of a dielectric is the electric dipole. An electric dipole is formed when two equal and opposite charges, $+q$ and $-q$, are separated by a distance vector $\vec{d}$ (Figure 1.2). There are two types of dipoles: permanent and induced. The former are always present even in the resting state (absence of external excitation). They are found in certain materials characterized by asymmetry at the molecular level where the centers of positive and negative charges do not coincide. Those belonging to the second type appear only under the effect of an external electric field applied to the dielectric material [24].

The fundamental quantity describing this system is the **dipole moment** $\vec{p}$, defined as:

$$\vec{p}=q\vec{d} \tag{1.2}$$

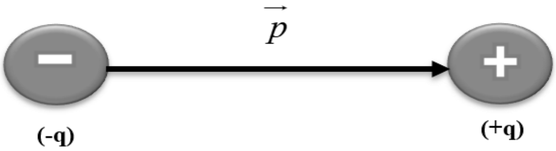

Figure 1.2: Electric dipole.

Where q is the magnitude of the charge and $\vec{d}$ is the displacement vector directed from the negative to the positive charge.

The dipole moment is a vector quantity, pointing from the negative to the positive charge, and represents both the magnitude and orientation of the dipole.

1.3.2 Macroscopic Polarization

On a macroscopic scale, the polarization $\vec{P}$ of a material corresponds to the volume density of dipole moments, that is, the vector sum of the elementary dipole moments referred to the unit volume:

$$\vec{P}=\frac{1}{V}\sum_{i=1}^{N}\vec{p_i} \approx N\left\langle \vec{p} \right\rangle \tag{1.3}$$

Where V is the volume of the dielectric, N is the number of dipoles per unit volume and $\langle \vec{p} \rangle$ is the average dipole moment.

1.3.3 Atomic or Molecular Polarizability

Polarizability is a microscopic property of an atom or molecule that quantifies how easily its electron cloud can be distorted by an external electric field [25].

When placed in a uniform static electric field, the atom or molecule develops an induced dipole moment $\overline{p}$ proportional to the local electric field $\vec{E}_{\text{local}}$:

$$\vec{p}=\alpha\vec{E} \tag{1.4}$$

and at the macroscopic scale:

$$\vec{P}=N\alpha\vec{E} \tag{1.5}$$

Where α is the molecular polarizability (SI units: $C\cdot m^2/V$), the higher α is, the more easily the atom or molecule is deformable, which contributes to a stronger macroscopic polarization.

1.3.4 Chemical Classification of Dielectric Materials and Influence on Polarization

Before addressing the different polarization mechanisms, it is important to remember that the dielectric properties of a material depend closely on its chemical nature and internal structure. Materials used as dielectrics can belong to different families depending on their atomic composition, the type of chemical bonds (ionic, covalent, or mixed), and the arrangement of atoms in the crystal lattice.

Understanding this relationship between structure, composition, and dielectric behavior is an essential step in interpreting the response of a material subjected to an external electric field. Materials can thus be classified into two broad categories: Inorganic materials and organic materials.

a) Inorganic Materials

Inorganic materials are characterized by a well-ordered crystalline structure, whose symmetry and the nature of the chemical bonds (ionic or covalent) largely determine their electrical and dielectric properties. Depending on the presence or absence of a center of symmetry in their crystal lattice, some of these materials exhibit piezoelectric behavior: they develop electrical polarization when subjected to mechanical stress, due to the displacement of charges in the unit cell [26-27].

A typical example of an inorganic material is barium titanate ($BaTiO_3$), belonging to the family of ferroelectric ceramics. Its perovskite-type crystalline structure (Figure 1.3) is composed of barium (Ba^{2+}), oxygen (O^{2-}), and titanium (Ti^{4+}) ions, the latter occupying a slightly off-center position in the oxygen octahedron. This displacement of the Ti^{4+} cation generates a spontaneous dipole moment, responsible for permanent internal polarization, even in the absence of an external electric field.

Under the effect of an applied electric field, the dipoles orient themselves preferentially, producing an observable macroscopic polarization. This property gives $BaTiO_3$ ferroelectric behavior, i.e., the ability to reverse the direction of its polarization under the action of a sufficiently intense electric field [26]. However, when the temperature exceeds a critical value called the Curie temperature, the crystalline structure becomes cubic and symmetrical; the material then loses its spontaneous polarization and becomes paraelectric.

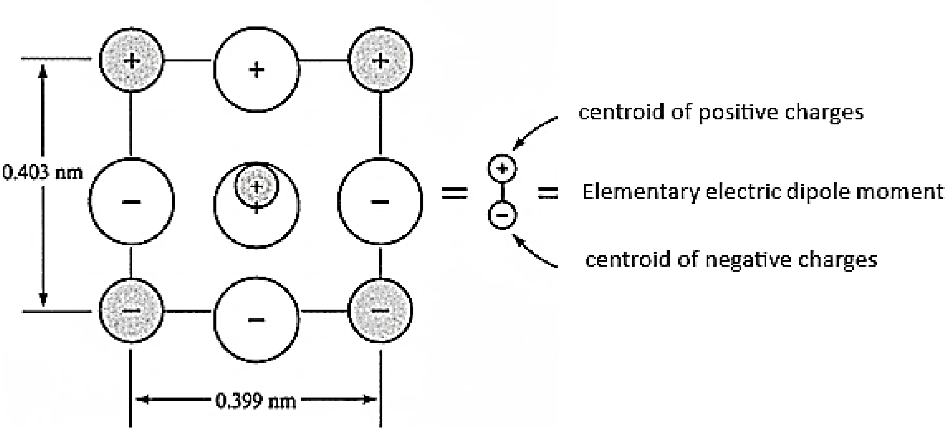

Figure 1.3: Schematic representation of the BaTiO3 quadratic unit cell.

Thanks to these characteristics, inorganic materials such as $BaTiO_3$ are widely used in electronics and electrical engineering, particularly for the manufacture of ceramic capacitors, piezoelectric sensors, and electromechanical actuators. Their strong response to an electric field or mechanical stress makes them essential elements in high-performance devices.

b) Organic Materials

Organic materials, primarily composed of molecular chains based on carbon, hydrogen, oxygen, and nitrogen, are characterized by an amorphous or semi-crystalline structure and the presence of flexible covalent bonds. These properties give them high mechanical flexibility, low density, and a good ability to be processed into thin films or insulating layers. Among these materials, organic polymers occupy a prominent place in dielectric applications [28-29].

Epoxy resin [30] is a representative example of an organic material of great technological interest. This thermosetting polymer offers numerous qualities:

- excellent adhesion to most substrates,
- excellent toughness and chemical resistance,
- low shrinkage during polymerization, ensuring good dimensional stability,
- good electrical and dielectric properties,
- absence of volatile matter during the curing phase.

From an electrical perspective, polarization in organic materials primarily results from the orientation of permanent dipoles present in the polymer chain. Polar functional groups (such as hydroxyl (OH) or epoxide groups) can align under the influence of an external electric field, resulting in orientable polarization. This response depends on the temperature, the frequency of the applied field, and the molecular mobility of the chain segments.

Thus, polar polymers such as epoxy resin can exhibit, under certain field and temperature conditions, a non-zero macroscopic polarization, similar to that observed in some ferroelectric materials. However, unlike ceramics such as $BaTiO_3$, the polarization of organic materials is generally reversible and dependent on molecular flexibility, rather than an ordered crystalline structure [31].

Thanks to their unique combination of mechanical, chemical, and dielectric properties, organic materials such as epoxy resin are now widely used as insulating materials, matrices for dielectric composites, and encapsulants in electronic devices.

1.4 Mechanisms and Types of Polarization

The effect of dielectric polarization was discovered by Michael Faraday in 1837, marking the starting point of the modern understanding of the electrical properties of insulators.

Polarization mechanisms are numerous and occur at various temporal and spatial scales. Four main types are distinguished: electronic polarization, ionic polarization, dipole polarization, and interfacial (or Maxwell-Wagner) polarization.

These different mechanisms can coexist within the same material or manifest themselves independently, depending on the chemical nature and structure of the dielectric.

Furthermore, all these polarizations can be classified into two main categories according to their dynamic behavior [32-33]:

- Elastic (or resonance) polarization, which corresponds to rapid and reversible deformations of the electron cloud or ionic lattice.
- Relaxation polarization, associated with slower processes, such as the reorientation of permanent dipoles or the accumulation of charges at interfaces.

Thus, the total polarization of a material results from the superposition of the different contributions from these elementary mechanisms [34-35].

1.4.1 Electronic Polarization

Electronic polarization is a phenomenon present in all dielectric materials, without exception. It results from the deformation of the electron cloud surrounding each atom under the effect of an applied electric field. When this field acts, the center of gravity of the negative charges (electrons) shifts slightly in the opposite direction to the field, while the center of gravity of the positive charges (nucleus) shifts in the direction of the field (Figure1.4). This results in an induced dipole moment at the atomic level.

This polarization establishes itself extremely rapidly, with a characteristic time of around 10^{-15} s, and it remains effective up to very high frequencies, particularly in the ultraviolet range ($\approx 10^{14}$–10^{16} Hz).

Since electron displacement is elastic, the energy required to deform the cloud is not dissipated as heat, but temporarily stored in the electric field. Although the effect is relatively weak, it constitutes the universal polarization mechanism and the only one active at very high frequencies, contributing directly to the optical dielectric permittivity of materials.

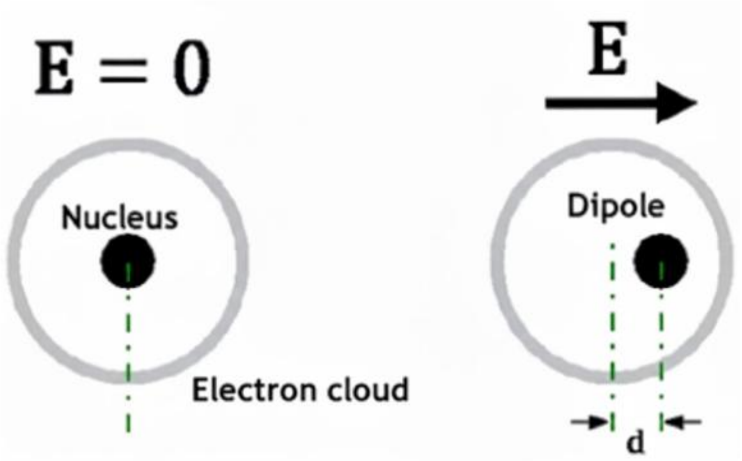

Figure1.4: Schematic representation of electronic polarization

1.4.2 Ionic Polarization

Ionic polarization, sometimes referred to as atomic polarization in certain contexts, occurs primarily in solid materials with an ionic crystalline structure, such as ceramics or inorganic compounds. It results from the relative displacement of positive ions (cations) and negative ions (anions) under the action of an applied electric field (Figure1.5). This displacement creates an induced dipole moment at the crystal lattice level. Due to the large mass of the ions, this phenomenon develops more slowly than electronic polarization, with a characteristic time of about 10^{-13} s, and it operates in the infrared frequency range ($\approx 10^{12}$–10^{13} Hz).

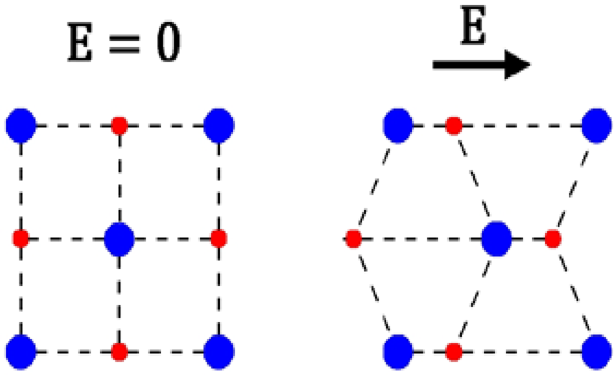

Figure 1.5: Schematic representation of ionic polarization

Ionic polarization strongly depends on the charge of the ions and the strength of the interionic bonds connecting the atoms in the lattice. Like electronic polarization, this is an elastic mechanism: it does not cause energy losses and disappears as soon as the applied field is removed. However, it induces a frequency-dependent dielectric delay, linked to the resonance of ionic motion.

This type of polarization plays a decisive role in the dielectric constant of materials at low and medium frequencies and contributes significantly to the dielectric properties of ionic and ceramic solids.

1.4.3 Orientational Polarization

Orientational polarization corresponds to the partial alignment of permanent dipoles present in polar molecules when an external electric field is applied. In the absence of a field, the dipole moments are randomly oriented, resulting in zero net polarization (Figure 1.6). Under the influence of the field, these dipoles tend to orient themselves in its direction, but their movement is limited by internal frictional forces and thermal agitation.

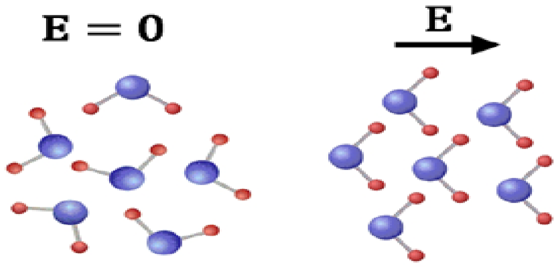

Figure 1.6: Schematic representation of orientational polarization

This type of polarization is characteristic of polar materials (such as H_2O, HCl, NH_3) and is highly temperature-dependent, decreasing as temperature increases. Orientational polarization occurs primarily in the microwave range (≈10^6–10^9 Hz) and is responsible for a significant portion of the dielectric losses associated with delayed rotations of permanent dipoles.

1.4.4 Interfacial Polarization

Interfacial polarization (or the Maxwell-Wagner-Sillaris effect [10]) appears in non-homogeneous dielectrics. This phenomenon occurs in heterogeneous materials and results from the accumulation of charges at the interface of two materials, that is, at the boundary of the two media exhibiting different dielectric conductivities and/or permittivities (Figure 1.7).

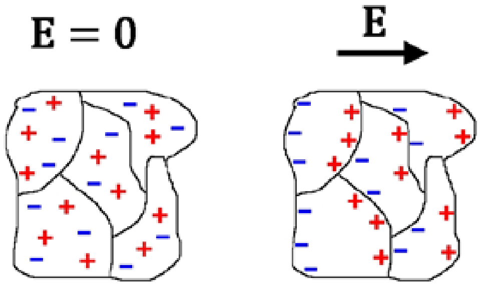

Figure 1.7: Schematic representation of interfacial polarization

This type of polarization also exhibits a relaxation characteristic; the relaxation time increases as conductivity decreases. Generally, interfacial polarization weakens in the vicinity of frequencies above acoustic frequencies in the low and mid-range frequencies, below 10^8 Hz.

Depending on the establishment time of each contribution, the aforementioned polarizations will appear successively under the effect of the electric field applied across the terminals of the material, as shown in figure 1.8. Beyond an establishment time $t > 10^3$s, a conduction phenomenon appears in the system, due to the appearance of small leakage currents caused by the movement of electric charge carriers passing through the material. This phenomenon hinders the detection of dipole relaxations at low frequencies and high temperatures. The effect of these movements is called dielectric losses [36].

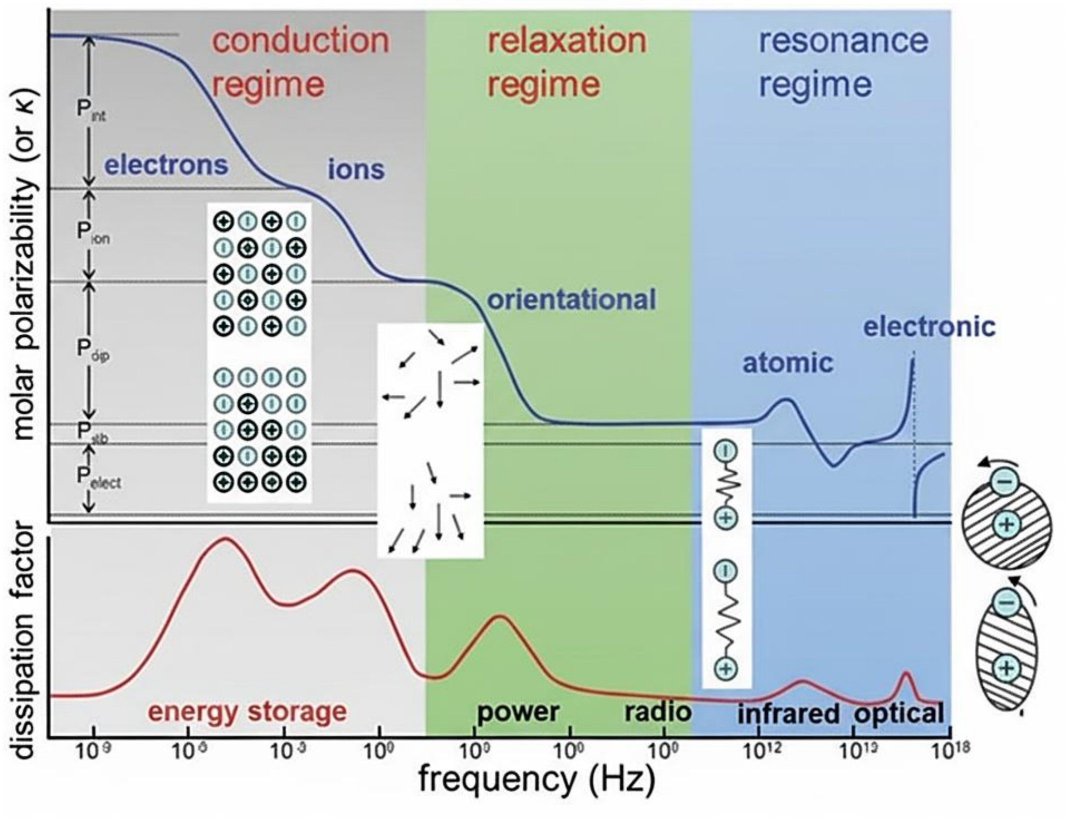

Figure 1.8: Contribution of different polarizations in a dielectric material.

1.5 Fundamental Equations of Electrostatics in Dielectric Media

The study of response of dielectric materials to an electric field relies on the fundamental equations of electrostatics, derived from Maxwell's laws in the static regime. These equations allow us to relate the distribution of dielectric charges to the polarization of the medium and the electric flux density.

1.5.1 Gauss's Law in Dielectric Media

The analysis of electrostatic behavior in dielectric media relies on Gauss's law, one of the fundamental relationships of electromagnetism [37-38].

This law establishes a direct correlation between the electric field flux through a closed surface and the total charge enclosed within the volume delimited by that surface.

In its integral form, it is written as:

$$\oint_S E.dS = \frac{Q_{int}}{\varepsilon_0} \tag{1.6}$$

Where E represents the electric field, dS the surface vector element, Q_{int} the total charge enclosed in the volume V, and ε_0 the permittivity of free space.

This relationship indicates that the outward flux of the electric field through a closed surface is proportional to the amount of charge contained in the corresponding volume.

By applying the divergence theorem, Gauss's law can be written in its differential form, called the Maxwell-Gauss equation:

$$\nabla .E = \frac{\rho}{\varepsilon_0} \tag{1.7}$$

where ρ denotes the volume charge density.

This equation states that the divergence of the electric field at a point in space is proportional to the charge density present at that point.

It is the first of Maxwell's four fundamental equations in electrostatics and rigorously describes the behavior of the field in a vacuum, where only free charges contribute to field generation.

However, when we introduce a dielectric medium, the situation becomes more complex. In such materials, the microscopic dipoles induced by the external electric field contribute additional charges and currents. This microscopic response cannot be neglected, and therefore Maxwell-Gauss equation must be reformulated to account for the presence of matter.

In a dielectric, we distinguish between two kinds of charges: free charges and bound charges. Free charges are those that can move over macroscopic distances, such as conduction electrons in metals or doped semiconductors. In insulators and dielectrics, free charges are usually absent or negligible, but when present, they are the ones directly controlled from the outside, for example by applying a voltage source.

Bound charges, on the other hand, originate from the displacement of charges inside atoms or molecules under the influence of an external electric field. When the field is applied, the negative electronic cloud is slightly displaced relative to the positive nucleus, creating microscopic dipoles. Although these dipoles are neutral as a whole, their spatial arrangement results in a redistribution of charges at the microscopic scale. This redistribution is expressed by the concept of polarization.

The bound charge density is given by:

$$\rho_{bound} = -\nabla .\vec{P} \tag{1.8}$$

where $\vec{P}$ is the polarization vector, defined as the dipole moment per unit volume.

Thus, the total charge density inside the dielectric is the sum of the free and bound contributions:

$$\rho = \rho_{Free} + \rho_{bound} \tag{1.9}$$

So, the total field inside the dielectric therefore results from the superposition of the external field and the polarization field. To account for this contribution, it is necessary to introduce the electric displacement vector, or Maxwell vector, defined by:

$$\vec{D} = \varepsilon_0 \vec{E} + \vec{P} \tag{1.10}$$

The vector $\vec{D}$ therefore represents the overall response of the material to the electric field, integrating both the contribution of the vacuum ($\varepsilon_0 \vec{E}$) and that of the polarized medium ($\vec{P}$). Its unit in the International System of Units is the coulomb per square meter *(C/m²)*.

and the generalized form of Gauss's law then becomes:

$$\nabla . \vec{D} = \rho_{Free} \tag{1.11}$$

This equation is much more practical than the original formulation, because the complicated contribution of bound charges is now hidden inside $\vec{P}$.

Figure 1.9 illustrates the application of Gauss's theorem to a parallel-plate capacitor, showing the Gaussian surface and the effect of the dielectric on the electric field inside the capacitor.

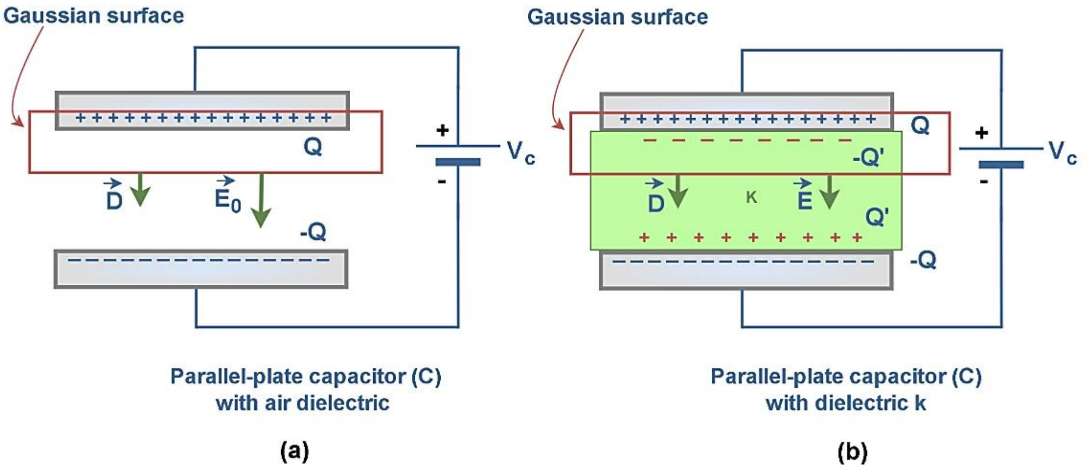

Figure 1.9: Application of Gauss's theorem to a parallel-plate capacitor

1.5.2 Electrical Susceptibility and Constitutive Relationship

To establish a quantitative link between polarization and the applied field, we introduce the concept of electric susceptibility. For a linear, isotropic, and homogeneous dielectric, the polarization vector is proportional to the local electric field:

$$\vec{P} = \varepsilon_O \chi_e \vec{E} \tag{1.12}$$

where χ_e is the electric susceptibility of the material, a dimensionless quantity that measures the ease with which the medium becomes polarized under the effect of an electric field. Substituting this relation into the expression of $\vec{D}$ we obtain:

$$\vec{D} = \varepsilon_0 (1 + \chi_e)\vec{E} = \varepsilon \vec{E} \tag{1.13}$$

The quantity $\varepsilon = \varepsilon_0 (1 + \chi_e)$ is defined as the absolute permittivity of the medium, while the ratio $\varepsilon_r = 1 + \chi_e$ is the relative permittivity, or dielectric constant. This relationship expresses that the density of the electric flux in a material depends directly on the applied electric field, weighted by the material's capacity to polarize. Thus, permittivity summarizes, at the macroscopic scale, all the microscopic polarization phenomena that occur in the dielectric.

1.6 Dielectric Permittivity and Dielectric Losses

The response of a dielectric material subjected to an alternating electric field depends on all the polarization mechanisms present in the medium. This response is described by the dielectric permittivity, a quantity that relates the applied electric field to the material's polarization. A distinction is made between absolute permittivity and relative permittivity ε_r, the latter being normalized with respect to the permittivity of free space.

$$\varepsilon_r = \frac{\varepsilon}{\varepsilon_0} \tag{1.14}$$

In the harmonic regime, the polarization does not instantaneously follow the applied field, which induces a phase shift and leads to the definition of a complex permittivity. The real part of this complex permittivity represents the electrostatic energy storage capacity, while the imaginary part reflects the dielectric losses associated with relaxation phenomena and, where applicable, the material's electrical conductivity [39-40].

$$\varepsilon_r^* = \varepsilon' - j\varepsilon'' \tag{1.15}$$

The loss tangent $tan\delta$, equal to the ratio of these two components, is a direct indicator of the energy dissipation level, while its inverse defines the quality factor *Q*. Thus, the complex permittivity, the loss tangent, and the quality factor are fundamental quantities for evaluating the dynamic behavior of a dielectric in high-frequency applications.

$$tan\delta = \frac{\varepsilon^{"}}{\varepsilon^{'}} \tag{1.16}$$

$$Q = \frac{1}{tan\delta} \tag{1.17}$$

1.7 Electrical Conductivity

Electrical conductivity is a physical quantity associated with conduction currents resulting from the movement of free charges [41]. It expresses a material's ability to allow these charges to flow under the influence of an electric field, and this transport is accompanied by energy losses responsible for the attenuation of electromagnetic waves in the propagation medium. Electrical conductivity, denoted σ, is generally expressed in Siemens per meter (*S/m*) and can, in certain applications, be considered a complex quantity.

At low frequencies (LF), the study of the ohmic behavior of the mixture is of major importance. The complex permittivity is given by the expression:

$$\varepsilon^{*}(\omega) = \varepsilon_{\infty} + \frac{\left(\varepsilon_{s} - \varepsilon_{\infty}\right)}{1 + j\omega\tau} - j\frac{\sigma_{s}}{\omega\varepsilon_{0}} \tag{1.18}$$

With τ: the relaxation time, ε_S: the static permittivity, σ_S: the static conductivity, and ε_∞: the permittivity at very high frequencies.

Where the influence of the third term is decisive in the low-frequency region.

$$\varepsilon^{"} = \frac{\sigma_{s}}{\omega\varepsilon_{0}} \tag{1.19}$$

The last relationship proves that the dielectric mixture exhibits conductive behavior at low frequencies. From equation (1.19), the conductivity of the composite can be obtained from the following relationship:

$$\sigma_{s} = \omega\varepsilon^{"}.\varepsilon_{0} \tag{1.20}$$

1.8 Parameters Influencing Relative Dielectric Permittivity

The amplitude of the applied electric field, the frequency, the temperature, the microstructure, external constraints, etc., are the parameters according to which the relative permittivity and the dissipation factor can vary.

1.8.1 Influence of the Amplitude

The variation of the electric field across the terminals of a dielectric material influences its permittivity. This is particularly true for ferroelectrics, whose spontaneous polarization can be oriented, or even reversed, by applying a sufficient electric field. Their polarization is not a linear function of the applied electric field, and a spontaneous polarization persists even in the absence of a field. This polarization exhibits hysteresis as a function of the applied electric field (Figure 1.10) [42].

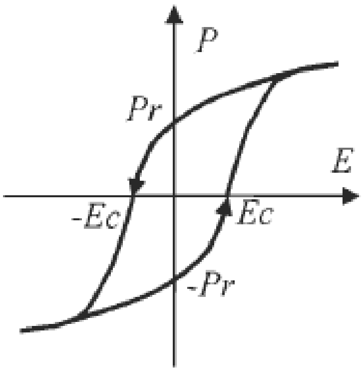

Figure 1.10: Hysteresis loop characteristic of a ferroelectric: polarization P as a function of the applied electric field E. P_r is the remanent polarization and E_c the coercive field required to cancel the spontaneous polarization [36].

1.8.2 Influence of frequency

At the lowest frequencies, the four mechanisms of polarization contribute to the relative permittivity value. As the frequency increases, the contributions of each type of polarization disappear one after the other, and the permittivity therefore decreases with frequency [43]. The polarization lags behind the electric field, resulting in energy dissipation [2].

1.8.3 Influence of grain size

Over the past few decades, the impact of grain size has been the subject of several studies. A close relationship between this parameter and the dielectric susceptibility of different materials is observed, particularly in the case of BaTiO3 [44]. The dielectric permittivity of BaTiO3 at room temperature exhibits a distinctive variation as a function of grain size, associated with the evolution of the ferroelectric domain configuration [45-47]. A maximum permittivity at room temperature can be reached with grains on the order of 0.8 to 11 µm, as shown in Figure 1.11 [44]. This is the size at which the structural distortion of the perovskite begins to decrease.

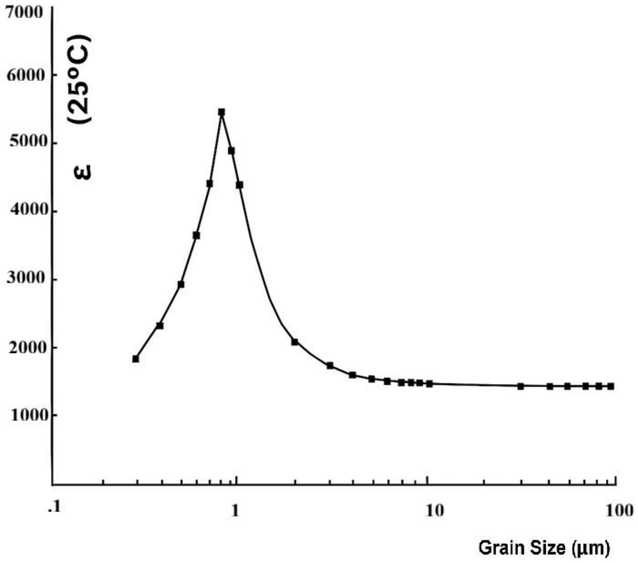

Figure1.11: Dielectric constant as a function of average grain size for BaTiO3 ceramics at 25°C.

1.8.4 Influence of temperature

The variation of relative permittivity with temperature is generally characterized by the capacitance temperature coefficient (CTC), expressed in *ppm/°C*. Temperature influences the polarization mechanisms of a material differently, particularly oriented and interfacial polarizations, which are the most sensitive: the former due to the increase in dipole mobility, the latter due to the increase in charge mobility at interfaces [42].

The effect of temperature depends strongly on the nature of the material. In polymers, approaching the glass transition temperature leads to a significant increase in permittivity, linked to the release of permanent dipole mobility. In ceramics, the emblematic example is $BaTiO_3$: increasing the temperature progressively alters its crystal lattice, shifting the relative charge centers and generating spontaneous polarization. Each crystalline phase transition is then accompanied by a reorganization of this polarization, which produces characteristic local maxima in the evolution of permittivity, as illustrated in Figure 1.12.

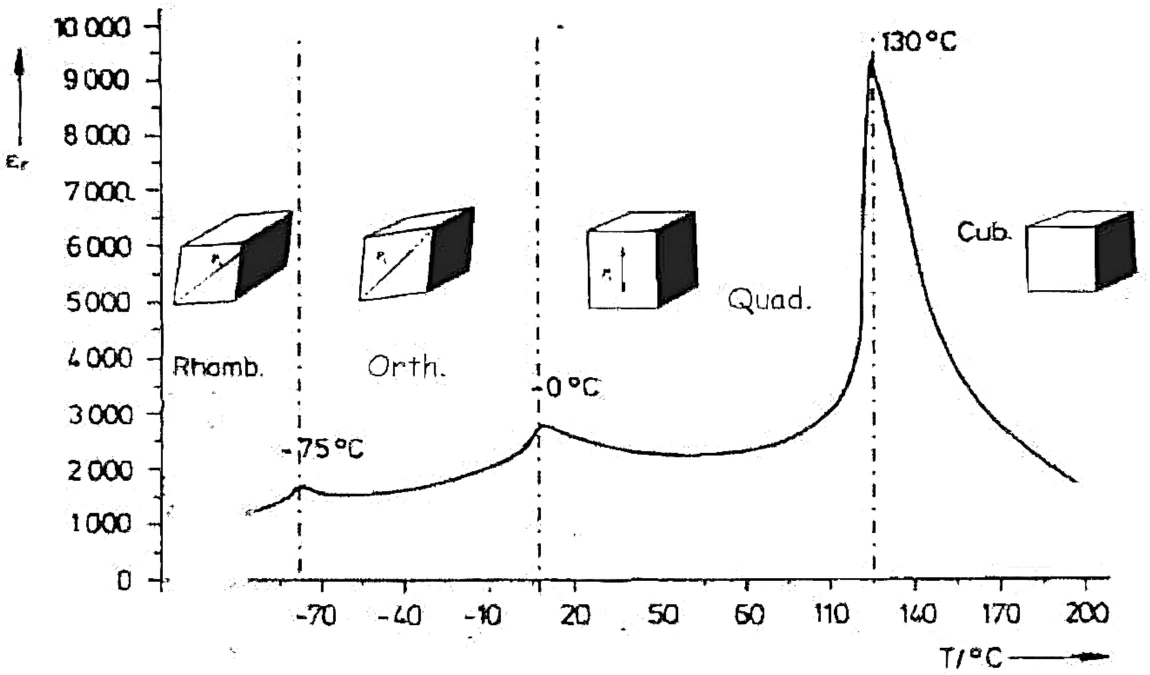

Figure 1.12: Evolution of the dielectric constant as a function of temperature in a BaTiO3 crystal.

1.9. Mixing Laws and Effective Field Models

In a homogeneous medium, permittivity does not depend on spatial variables; it has the same value at every point. This is no longer the case in a heterogeneous medium. However, when the size of the heterogeneities is small compared to the signal wavelength, the medium can be represented by an average permittivity and can be considered effectively homogeneous.

The problem then arises of relating this average (effective) permittivity to those of the different constituents (Figure 1.13). This quantity depends on the specific properties of the constituents (morphology, topology), their volume fractions, their shapes, and their sizes.

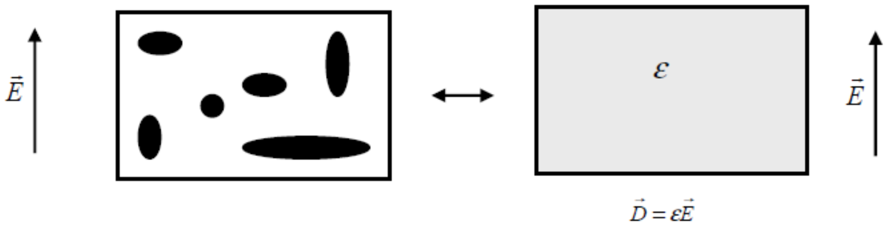

Figure 1.13: Homogenization consists of replacing the heterogeneous medium with an effective homogeneous medium that has the same dielectric properties.

In general, the effective permittivity depends on the degree of complexity of the composite structure. If the distribution of inhomogeneities is periodically distributed in the matrix, the effective permittivity can be analytically evaluated under certain conditions using various methods [48-49]. However, for media with a disordered spatial distribution of inclusions, there is no rigorous solution. The use of either numerical methods to construct the internal morphology, or phenomenological laws (mixture laws), or effective medium type approaches, or even boundary methods, which then become essential for evaluating the permittivity.

1.9.1 Quasi-Static Approach

When studying the propagation of an electromagnetic wave in a heterogeneous medium, several spatial scales must be considered. The first is the wavelength of the incident wave, to which is added the typical size of the material's heterogeneities (inclusions, pores, interfaces). An attenuation length δ (skin depth) can also be introduced, as well as characteristic transport lengths, such as the elastic mean free path $l_e = 1/(n\sigma_e)$, associated with scattering, and the absorption mean free path $l_\alpha = 1/(n\alpha_\alpha)$, related to losses. These quantities are governed by the inclusion density n and by the scattering cross sections σ_e S and absorption cross sections σ_α.

In the long wavelength (quasi-static) scenario, everything happens as if the wave propagating through the medium does not perceive the intricate details of the spatial disorder. The medium can then be considered a homogeneous medium characterized by an effective permittivity if the following conditions are met:

$$|kd| \ll 1 \tag{1.21}$$

$$|k_i d| \ll 1 \quad i = 1, 2 \tag{1.22}$$

Where $k_i = \frac{\omega}{c}\left(\varepsilon_i \mu_i\right)^{\frac{1}{2}}$ representing the wave vectors associated with the media of permittivity ε_1 and ε_2 and permeability μ_1 and μ_2; k being the wave vector in the medium and d defining a typical size of the disorder. From Eq. 21, it is easy to show that the quasi-static approach is only valid in a low-frequency regime whose upper limit in angular frequency of the excitation field is given by:

$$\frac{c}{d(\varepsilon\mu)^2} \tag{1.23}$$

In what follows, we will primarily consider heterogeneous media satisfying $d > l_a > l_e$, that is, systems for which scattering and absorption are sufficiently weak so as not to significantly disrupt the electric field distribution. Under these assumptions, losses and multiple scattering can be neglected, and the concept of the effective medium becomes fully relevant. The domain of validity of this approach is therefore directly linked to the size of the inclusions: if these become comparable to or larger than the wavelength in the material, the scattering of the incident wave becomes significant, and the effective medium approximation is no longer applicable. In this case, more advanced methods, explicitly incorporating scattering or resonance phenomena, are necessary to accurately describe the dielectric properties of composites [49].

1.9.2 Local Electric Field Theories

The study of the effective properties of heterogeneous media can be introduced particularly clearly using the concept of a local field. This approach allows for a direct link to be established between the microscopic behavior of inclusions and the macroscopic response of the composite material. Depending on the assumptions made about the average environment in which each inclusion is immersed, we find the classic Maxwell-Garnett (MG) or Bruggeman (SBG) expressions, which constitute the two reference formulations for effective medium models.

The starting point for this analysis is based on the hypothesis, derived from the Clausius-Mossotti theory, that a dielectric particle subjected to a uniform field behaves like an electric dipole. In a composite material, each inclusion is therefore influenced not only by the applied field, but also by the field resulting from the presence of other particles. The field actually experienced by an inclusion, called the local field, is thus the sum of the external field and the interaction contributions.

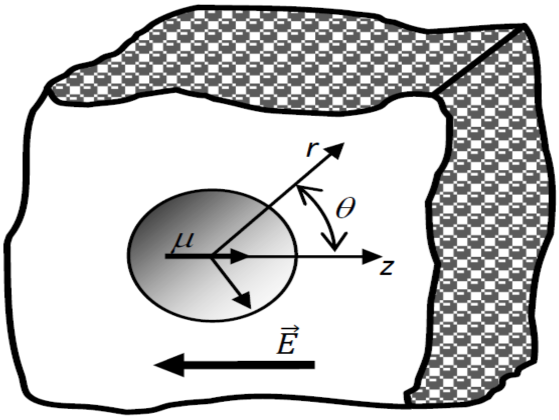

Figure 1.14: Macroscopic cavity located in an external electric field $\vec{E}$.

To determine this local field, it is common to use the Lorentz sphere principle. This involves considering an imaginary spherical cavity surrounding the particle under study (Figure 1.14). Inclusions located outside this cavity are modeled as a polarized continuum, while those inside directly influence the local field. The total field within this cavity is then the sum of the applied field, the field due to the surrounding continuum, and the field generated by the particles inside [50].

The Lorentz approximation assumes that the dipolar contribution of particles located inside the cavity is negligible. This approximation is rigorous in a complete cubic lattice and remains valid when the concentration of inclusions is sufficiently low. Multipolar contributions, which are more complex, are not considered in this framework. The macroscopic field created by a uniformly polarized continuous medium, for a spherical cavity, is given by:

$$\vec{E}_e = \frac{\vec{P}}{3\varepsilon_o} \tag{1.24}$$

From this, we can deduce the expression for the local field:

$$\vec{E}_e = \vec{E}_0 + \vec{E}_e = \frac{2+\varepsilon}{3}\vec{E}_0 \tag{1.25}$$

The polarization per unit volume of a medium consisting of k types of particles, each with a polarizability α_k and a number density N_k, is expressed as:

$$\vec{P} = \sum_k N_k \alpha_k \vec{E}_{local} \tag{1.26}$$

By introducing Eq. 1.25 into Eq. 1.26, and using the definition of polarization (Eq. 1.21), we obtain the Clausius Mossotti relation:

$$\frac{\varepsilon - 1}{\varepsilon + 2} = \frac{1}{3\varepsilon_0} \sum_k N_k \alpha_k \tag{1.27}$$

This equation again reveals a relationship between two macro-meso scales. If we repeat the reasoning to move from the mesoscopic to the microscopic scale (see Figure 1.15), assuming that the application assumptions of Eq. 1.27 remain valid, we arrive at:

$$\frac{\varepsilon_k - 1}{\varepsilon_k + 2} = \frac{1}{3\varepsilon_0} N_{\alpha k} \alpha_k \tag{1.28}$$

where N_{ak} is the number of atoms per unit volume of material .

The macro-micro transition relationship is then given by:

$$\frac{\varepsilon-1}{\varepsilon+2}=\frac{1}{3}\sum_{K}N_K\left[\frac{3\varepsilon_0}{N_{\alpha k}}\frac{\varepsilon_k-1}{\varepsilon_K+2}\right] \tag{1.29}$$

because $N_{\alpha k}/ N_k$ is equal to the volume fraction V occupied by material k in the composite. Therefore, we obtain:

$$\frac{\varepsilon-1}{\varepsilon+2}=\frac{1}{3\varepsilon_0}\sum_{k}V\frac{\varepsilon_k-1}{\varepsilon_k+2} \tag{1.30}$$

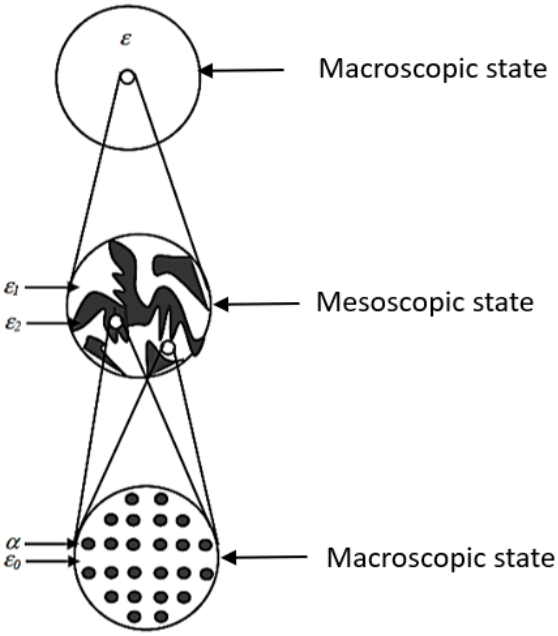

Figure 1.15: Principle of multi-scale analysis of the transition from macroscopic to microscopic [49].

We thus recover the MG equation defined for spherically shaped inclusions. By setting $\varepsilon = 1$ in the left-hand side of Eq. 1.30, we recover the SBG equation [8-9].

1.9.3 Maxwell-Garnett Mixing Law

The Maxwell-Garnett (MG) model [8], derived from the Clausius-Mossotti relation, was developed in 1904 to explain the coloration of glasses containing a small fraction of metallic particles dispersed in a permittivity matrix.

The key principle is to consider each inclusion as an isolated dipole, whose total polarizability is the sum of its individual polarizabilities, neglecting interactions between inclusions (Lorentz field approximation). The effective permittivity of the composite is obtained by applying the Clausius-Mossotti relation at the microscopic and then macroscopic scales:

$$\varepsilon = \varepsilon_m + 3v\varepsilon_m \frac{\varepsilon_i - \varepsilon_m}{\varepsilon_i + 2\varepsilon_m - v(\varepsilon_i - \varepsilon_m)} \tag{1.31}$$

where εi and εm are respectively the permittivities of the inclusions and the matrix, and v is the volume fraction of the inclusions.

The MG model accurately describes composites with a low inclusion fraction, particularly dispersed metallic particles, but becomes inaccurate for concentrations above 50%. Figure 1.16 shows a medium composed of material spheres inserted into a host medium that can be described by this theory.

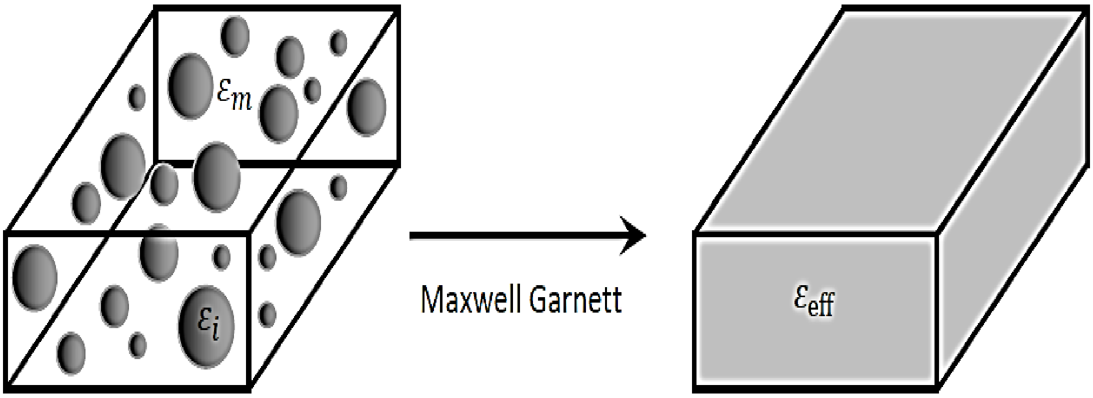

Figure 1.16: The composite medium described by Maxwell-Garnett's theory.

The modified formulation takes into account the depolarization factor A of the inclusions $(0 < A < 1)$.

$$\varepsilon = \varepsilon_m \left(1 + \frac{v\left[\varepsilon_i / \varepsilon_m - 1\right]}{1 + A(1-v)\left[(\varepsilon_i / \varepsilon_m) - 1\right]}\right) \tag{1.32}$$

For inclusions with circular geometry, A=1/2.

1.9.4 Bruggeman mixing law

To deal with high volume fractions, Bruggeman [9] proposed in 1935 an alternative approach known as the Effective Medium Approximation (EMA). Unlike the Maxwell-Garnett model, the existence of an explicit host material is no longer assumed. Each component of the mixture is considered to be immersed in a homogeneous effective medium of unknown permittivity εeff, which is to be determined (Figure 1.17).

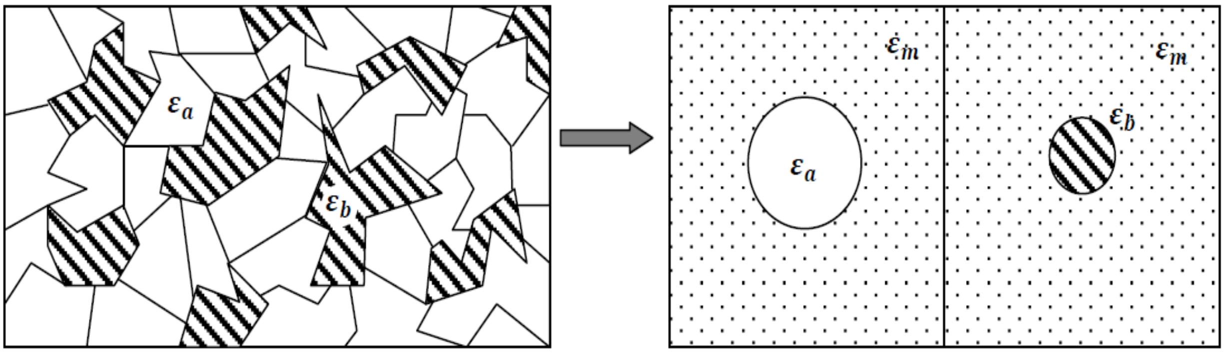

Figure 1.17: Unit cell of the Bruggeman model.

For spherical inclusions with permittivity ε_i and volume fraction v, immersed in an environment with permittivity ε_m, the Bruggeman equation is written:

$$(1-v)\frac{\varepsilon_m-\varepsilon_{eff}}{\varepsilon_m+2\varepsilon_{eff}}+v\frac{\varepsilon_i-\varepsilon_{eff}}{\varepsilon_i+2\varepsilon_{eff}}=0 \quad (1.33)$$

This symmetrical relationship balances the contributions of the two components by weighting them by their respective volume fractions. It contrasts with the Maxwell-Garnett law, which is inherently asymmetric, since each inclusion is immersed in a predefined matrix. In Figure 2.3, the inclusions interact through the same effective medium.

A modified version of Bruggeman's formula can also be used to estimate the effective permittivity of a composite with two distinct components.

$$\varepsilon=\frac{1-A(1+\frac{\varepsilon_i}{\varepsilon_m})+v(\frac{\varepsilon_i}{\varepsilon_m}-1)\pm\sqrt{[1-A(1+\frac{\varepsilon_i}{\varepsilon_m})+(1-v)(\frac{\varepsilon_i}{\varepsilon_m}-1)]^2+4A(1-A)\frac{\varepsilon_i}{\varepsilon_m}}}{2(1-A)} \quad (1.34)$$

1.9.5 Birchak Law

Birchak [51] proposed the so-called CRIM (Complex Refractive Index Method) for calculating the dielectric permittivity of a binary mixture, assuming that the size of the inclusions is small enough compared to the wavelength. This method is given by the formula:

$$\sqrt{\varepsilon_{eff}}=v\sqrt{\varepsilon_i}+(1-v)\sqrt{\varepsilon_m} \quad (1.35)$$

1.9.6 Looyenga Law

In his formulation of the mixture, Looyenga [52] proposes a valid approximation when the two components exhibit low dielectric contrast, that is, when their permittivities are close. He assumes that these can be expressed in the form $\varepsilon_i = \varepsilon_{eff} - \nabla\varepsilon_{eff}$ and, $\varepsilon_m = \varepsilon_{eff} + \Delta\varepsilon_{eff}$ and vice versa. Under this assumption, the effective permittivity εeff can be estimated by:

$$(\varepsilon)^{1/3} = (\varepsilon_i)^{1/3} v + (\varepsilon_m)^{1/3}(1-v) \tag{1.36}$$

1.9.7 Wiener Law

Regardless of the shape, size, physical state, volume concentration, or orientation of the different phases, the effective dielectric response of the mixture always lies between two limits known as the Wiener boundaries.

This theory assumes that an emulsion is formed by parallel and superimposed layers of the continuous and dispersed phases in their pure state. Wiener [53] proposes two equations. The first (lower Wiener law) considers the layers to be parallel to the plates of the measuring capacitor; the system then behaves like two capacitors in series, whose permittivity is given by:

$$\frac{1}{\varepsilon_{w\inf}} = \frac{v}{\varepsilon_i} + \frac{1-v}{\varepsilon_m} \tag{1.37}$$

The second expression (upper Wiener's law) is obtained by considering that the layers are perpendicular to the plates of the measuring capacitor, and then the permittivity of the system is calculated as that of two capacitors in parallel:

$$\varepsilon_{w\sup} = v\varepsilon_i + (1-v)\varepsilon_m \tag{1.38}$$

1.9.8 Lichtenecker-Rother Law

This law is based on a static approach to dielectric mixtures. Experimental work shows that Lichtenecker's formula is widely used, including for anisotropic media, due to its high flexibility. It proves particularly suitable for describing the dielectric behavior, whether static or dynamic, of statistical mixtures across all volume fractions.

Lichtenecker and Rother [54] consider that the effective permittivity of a composite can be expressed as a general function G of the individual permittivities of each of the constituents and their volume fractions. For a mixture containing N phases, this relationship is generally written as:

$$\varepsilon_{eff} = G(\varepsilon_1, \varepsilon_2, ...\varepsilon_N, v_1, v_2, ...v_N) \tag{1.39}$$

The purpose of this law is to determine the form of G; they found two possible forms for this function. For two components, the expression can be written in the form:

$$\varepsilon_{eff} = \varepsilon_1^{v_1}\, \varepsilon_2^{v_2} \tag{1.40}$$

$$\varepsilon_{eff}^{\alpha} = (v_1 \varepsilon_1^{\alpha}\, v_2 \varepsilon_2^{\alpha})^{\frac{1}{\alpha}} \text{ with } (-1 \le \alpha \le 1) \tag{1.41}$$

Generalizing to a mixture of N phases leads to:

$$\varepsilon_{eff}^{\alpha} = \sum_{i \neq 1}^{N} v_i \varepsilon_i^{\alpha} \text{ with } (-1 \le \alpha \le 1) \tag{1.42}$$

$$\varepsilon_{eff}^{\alpha} = \prod_{i=1}^{N} \varepsilon_i^{v_i} \tag{1.43}$$

1.9.9 Bottreau Law

Following numerous measurements carried out on dielectric composites whose behavior did not follow the conventional Lichtenecker law, particularly those exhibiting percolation or a non-spherical granular structure, Bottreau [55] proposed a new method of representation. Instead of plotting the logarithm of the permittivity as a function of the volume fraction of the constituents, he chose to express it as a function of the logarithm of these volume fractions.

Considering that v_i represents the volume fraction corresponding to the inflection point of the experimental curves, Bottreau made an initial change of origin by taking $\ln(v_i)$ as the reference. The resulting curves then exhibit a shape close to a hyperbolic tangent, provided that $ln(v_2/v_i)$ is used in the first case and $-\ln(v_1/(1-v_i))$ in the second case.

He then defined:

$$\ln(v_0) = \ln \sqrt{\frac{v_2 v_1}{v_i(1-v_i)}} \tag{1.44}$$

where v_1 and v_2 denote the volume fractions of the two constituents.

By applying a second change of origin, he obtains the final abscissas, which serve as the basis for the analysis and become functions of $\ln(v_2/v_1)$. This step leads to:

$$\ln(\frac{v_2}{v_1}) - \ln \sqrt{\frac{v_2 v_1}{v_i(1-v_i)}} = \ln \sqrt{\frac{v_2(1-v_i)}{v_1 v_i}} \tag{1.45}$$

By proceeding similarly with the variable ln ((1-v_i) /v_1), we obtain:

$$\ln\left(\frac{(1-v_i)}{v_1}\right)-\ln\sqrt{\frac{v_2v_1}{v_i(1-v_i)}}=\ln\sqrt{\frac{v_2(1-v_i)}{v_1v_i}} \tag{1.46}$$

Since the two forms obtained for the abscissas are identical, it becomes possible to process all the experimental data within the same coordinate system. By setting this common variable equal to ln(v_N), considered as a normalized variable, it then suffices to normalize the variations of ln(ε') between the values +1 and −1.

This normalization leads to a hyperbolic tangent-type function, whose slope at the origin, denoted α, must be determined. Bottreau thus obtains the final relation of his model, which is written in the form:

$$\ln(\varepsilon_N)=\frac{2\ln(\varepsilon)-\ln(\varepsilon_1\varepsilon_2)}{\ln(\frac{\varepsilon_1}{\varepsilon_2})}=\tanh(\frac{\alpha}{2}\ln v_N) \tag{1.47}$$

$$\text{With }\ v_N=\frac{(1-v_i)v_2}{v_1v_i} \tag{1.48}$$

$$\text{This leads to: }\ln(\varepsilon_N)=\frac{v_N^{\alpha}-1}{v_N^{\alpha}+1} \tag{1.49}$$

So we will have:

$$v_N^{\alpha}=\frac{\ln(\varepsilon)-\ln(\varepsilon_1)}{\ln(\varepsilon_2)-\ln(\varepsilon)} \tag{1.50}$$

After expansion, we obtain:

$$n(\varepsilon)=p_1\ln(\varepsilon_1)+p_2\ln(\varepsilon_2) \tag{1.51}$$

$$p_1=\frac{\left(\frac{v_1}{1-v_1}\right)^{\alpha}}{\left[\left(\frac{v_2}{v_i}\right)^{\alpha}+\left(\frac{v_1}{1-v_i}\right)^{\alpha}\right]}=\frac{1}{1+v_N^{\alpha}} \tag{1.52}$$

$$p_2=\frac{\left(\frac{v_2}{v_i}\right)^{\alpha}}{\left[\left(\frac{v_2}{v_i}\right)^{\alpha}+\left(\frac{v_1}{1-v_i}\right)^{\alpha}\right]}=\frac{v_N^{\alpha}}{1+v_N^{\alpha}} \tag{1.53}$$

1.9.10 Bergman Law

In 1978, Bergman [56] established a general formulation by analyzing the distribution of the electric field inside and outside an ellipsoid embedded in a homogeneous medium. His approach involves evaluating how the applied field is modified by the presence of the inclusion, which induces a local perturbation and a redistribution of the electric field in its vicinity. This detailed analysis of the electrostatic behavior of an ellipsoid allowed Bergman to derive a more general expression for the effective dielectric response of composites.

$$\varepsilon = \varepsilon_m + v\varepsilon_i \frac{\varepsilon_m - \varepsilon_i}{\varepsilon_i + A(\varepsilon_m - \varepsilon_i)} \tag{1.54}$$

1.9.11 Yamada Law

Yamada and al. [57] proposed an expression describing the dielectric behavior of a composite consisting of a random distribution of ellipsoidal particles dispersed in a continuous matrix. Their model explicitly takes into account the influence of the geometry of the inclusions by introducing a shape parameter, denoted n, which characterizes the ellipticity or elongation of the particles. This approach thus makes it possible to modulate the effective response of the material according to the actual morphology of the inclusions, beyond the more restrictive assumption of spherical particles.

$$\varepsilon = \varepsilon_m \left[1 + \frac{nv(\varepsilon_i - \varepsilon_m)}{n\varepsilon_m + (1-v)(\varepsilon_i - \varepsilon_m)} \right] \tag{1.55}$$

The theoretical models discussed above can be classified into two main categories, as presented in Table 1.1. The first category comprises the original empirical models, which do not account for factors such as depolarization effects, filler shape, or distribution. The second category consists of modified laws in which these factors are explicitly taken into account.

Table 1.1: Classification of Theoretical Models

Original Mixing Laws	Modified Mixing Laws
• Maxwell Garnett	• Modified Maxwell Garnett
• Bruggeman	• Modified Bruggeman
• Looyenga	• Bottreau
• Weiner	• Bergman
• Lichtenecker-Rother	• Yamada

1.10 Conclusion

This chapter introduces the fundamental concepts of composite dielectric materials to establish the theoretical framework for this study. The different types of polarization, at both microscopic and macroscopic scales, are presented, as is the application of Gauss's law to dielectrics. The concepts of permittivity, losses, and conductivity are examined, along with the influence of key parameters such as frequency, temperature, and grain size on dielectric properties. Furthermore, the concepts of local and effective fields, as well as approaches based on mixing laws, are discussed to better understand the behavior of composites. These theoretical elements form the necessary foundation for the following chapter, which will focus on characterization methods and sample preparation procedures, in order to connect the experimental results to the theoretical concepts presented in this chapter.

CHAPTER

2

Electromagnetic Characterization of Dielectric Materials

2.1 Introduction

Characterizing the dielectric properties of materials is an essential step in analyzing the electromagnetic behavior of composites. Among the various existing approaches, several techniques provide access to complex permittivity, such as waveguide methods, resonant devices, coaxial probes, and reflectometry techniques.

This chapter focuses on three complementary methods used to study dielectric composites. The first relies on time-domain reflectometry (TDR), a broadband technique that involves injecting an electromagnetic pulse into a coaxial line to analyze the reflected signals and deduce the material's frequency response. The second method uses a rectangular X-band waveguide to determine the complex permittivity at a fixed microwave frequency by observing how the sample modifies wave propagation within the waveguide. The third method presented is the finite element method, which allows for the accurate modeling of the electromagnetic behavior of complex dielectric structures and overcomes the limitations of classical analytical approaches.

2.2 Characterization by Time-Domain Reflectometry

The time-domain reflectometry (TDR) technique adopted in this study is a broadband microwave method, recognized for its conceptual simplicity, speed of execution, and reliability in determining the electromagnetic properties of materials, particularly dielectric properties. It is based on studying the reflection generated by the interaction of an electromagnetic pulse with the sample to be characterized, placed in a transmission line.

2.2.1 Measurement Principle

The principle of TDR is based on analyzing the reflection generated when a short electromagnetic pulse, with a rise time typically less than $35ps$, interacts with a sample placed in a coaxial transmission line. The sample used in our study consists of a solid tube with an external diameter of 7 mm and an internal diameter of 3 mm, providing a characteristic impedance of 50 Ω, with a thickness that varies according to experimental requirements.

The pulse stimulus travels along the coaxial line and, when it encounters an impedance discontinuity at the sample-line interface, part of the wave is reflected while another part is transmitted. Successive reflections, including those reflected by the end plate of the measurement cell, are recorded by a sampler connected to a digital oscilloscope, and their time-domain analysis allows for the precise deduction of the sample's dielectric properties, such as the complex permittivity. Examining reflected signals also allows for a detailed characterization of the nature of discontinuities along the line, whether capacitive, inductive, or resistive, as well as the assessment of any potential losses. The complete measurement setup (Figure 2.1) includes a step pulse generator (HP 54121A), a digitizing oscilloscope (HP54120B), the coaxial transmission line, the measurement cell, and a computer system for data processing and storage. This configuration enables the acquisition, analysis, and visualization of time-domain signals, and, due to the broadband nature of the stimulus, TDR provides information on dielectric properties over a wide frequency range. The technique can also be adapted to the frequency domain using a vector network analyzer when sensitivity, accuracy, or spectral resolution are required. Its conceptual simplicity, combined with the wealth of information provided, has enabled TDR to find a wide range of applications in the characterization of dielectric materials, whether solid or liquid, and today constitutes a preferred tool for the study of microwave composites in an advanced scientific research context [58-61].

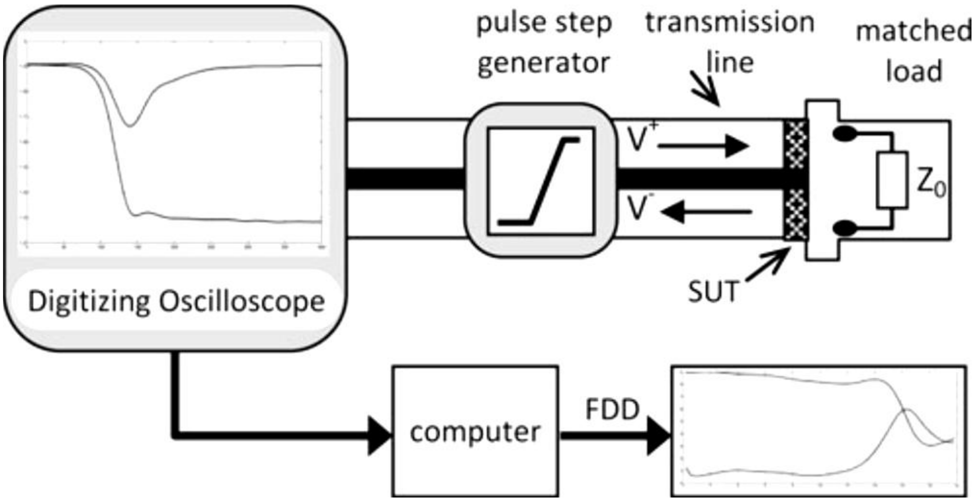

Figure 2.1: TDR experimental setup [61].

2.2.2 Measurement Cell

The coaxial measurement cell used in this study, supplied by Maury Microwave and illustrated in Figure 2.2, plays a crucial role in the microwave characterization of dielectric materials. Made of gold-plated copper, it offers excellent conductivity and very low losses, ensuring stable signal propagation. Its geometric dimensions are calculated to guarantee a characteristic impedance of 50 Ω, a standard value in microwave metrology. The transitions are achieved using APC-7 mm connectors, renowned for their mechanical precision and low impedance mismatch [61].

In the line segments before and after the sample, the impedance depends solely on the internal geometry of the cell. Thus, the only electromagnetic discontinuity originates from the inserted material, allowing the measured reflections to be clearly correlated with the sample's inherent properties. This configuration allows for the determination of the dielectric properties (complex permittivity) of the material over a wide frequency range, using well-established analytical models. This choice of a coaxial cell is particularly well-suited to composite materials, whose civil applications often require operation in lower frequency bands, where the coaxial line provides a simple, precise, and ideally adapted solution.

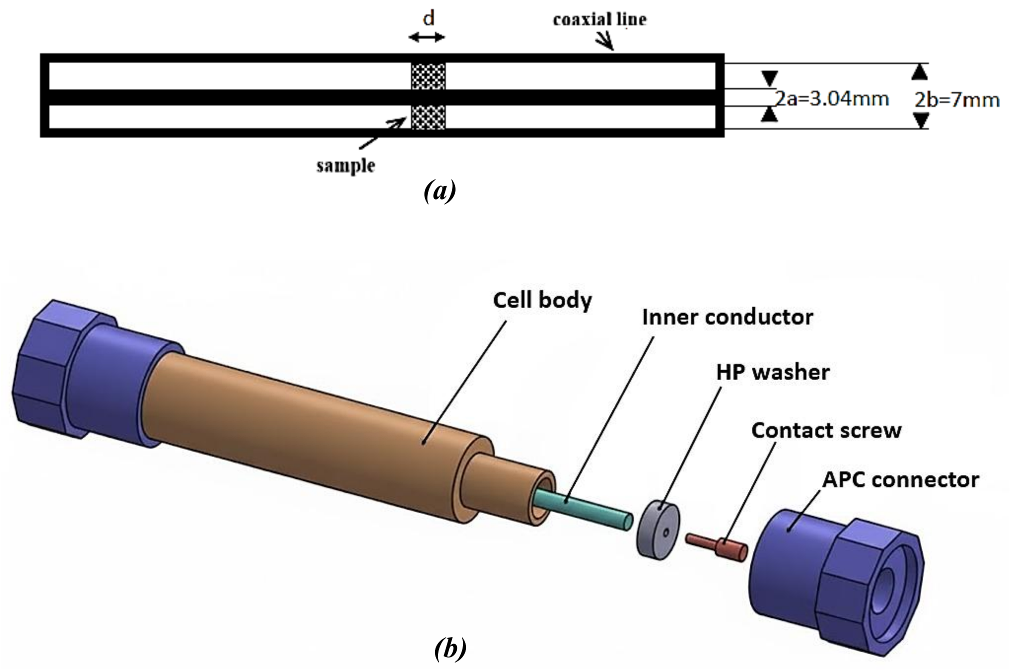

(a)

(b)

Figure 2.2: *(a)* Geometric dimensions of the measurement cell in reflection/transmission, *(b)* Composition of the APC-7 measurement cell.

2.2.3 Experimental Methods Used in TDR

To fully exploit the reflected signals obtained by the TDR technique [62], various measurement methods have been developed, each adapted to the geometry of the line and the characteristics of the sample. These methods are all based on the analysis of the reflection coefficient and allow the measured signals to be linked to the dielectric permittivity of the sample.

The main distinctions are [63]:

a) **The first reflection method.**
b) **Multiple reflection methods:** It comes in three experimental configurations, namely the short-circuited line, the open line and the adapted line.

2.2.3.1 First Reflection Method

The first reflection method relies on the exclusive analysis of the first wave reflected at the interface between the surface and the sample, that is, at the first interface encountered by the voltage step in the coaxial line. In practice, the total reflected signal results from the superposition of this first reflection and additional reflections generated at subsequent interfaces, particularly at the opposite end of the sample. However, this method aims to isolate only the first reflection; therefore, the sample must be long enough so that subsequent reflections do not interfere with the first detected pulse. This condition ensures that the contribution of reflections generated at the second interface is negligible during the analysis.

The analysis of this first reflected wave allows for the direct estimation of the material's complex permittivity, and the desired information is contained within the time signature of this initial reflection. This approach has the advantage of being conceptually simple and leading to relatively straightforward calculations once the reflection coefficient is determined experimentally.

However, the method suffers from a major limitation: it is only applicable to samples long enough to temporally separate the first reflection from the multiple internal reflections. Otherwise, the successive contributions overlap, rendering the analysis invalid. Since the samples studied in our work do not meet this condition, the first reflection method is not suitable for our experimental setup [64].

2.2.3.2 Multiple Reflection Methods

These methods, unlike the first one presented above, take into account the reflections generated between the two interfaces (air-sample and sample-load). The total reflection coefficient in the medium (1) will therefore include the contribution of all these reflections (Figure 2.3).

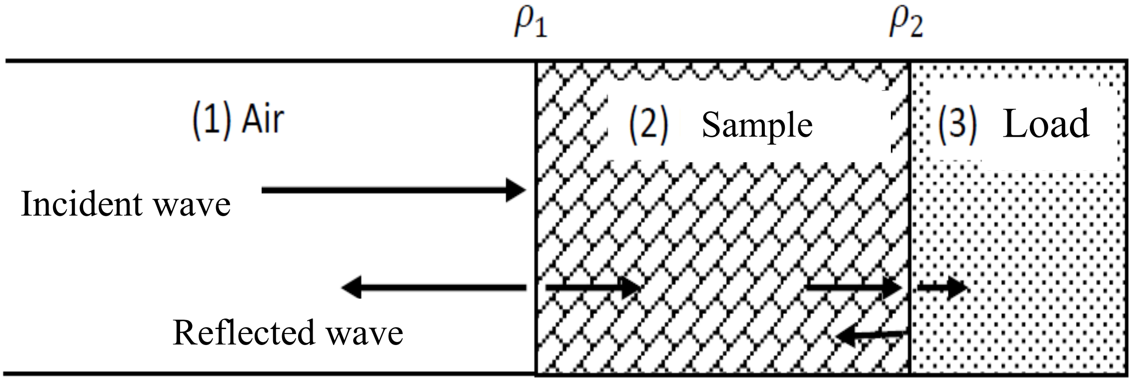

Figure 2.3: Multiple reflections in a sample.

According to Figure 2.3, when a wave at normal incidence reaches the first interface, part of the wave penetrates the sample while the other part is reflected. The transmitted portion propagates with a propagation constant $\gamma_2 = j.\frac{\omega}{c}.\sqrt{\varepsilon_r.\mu_r}$ throughout the sample until it encounters the second interface. At this point, it undergoes the same process as the fundamental incident wave.

The reflected portion will now return to the first interface and will also generate two other waves: reflected and transmitted. The transmitted wave from medium (2) to medium (1) will be added to the fundamental reflected wave. Therefore, in the end, the total reflected wave will be the sum of the fundamental reflected wave plus the secondary reflected waves generated by the multiple reflections, and we write:

$$E_r = E_{r0} + E_{r1} + \cdots = \sum_{i=0}^{\infty} E_{ri} \tag{2.1}$$

The total reflection coefficient will be:

$$R(\omega) = \frac{\rho_1 + \rho_2 e^{-2\gamma_2 d}}{1 + \rho_1 \rho_2 e^{-2\gamma_2 d}} \tag{2.2}$$

where ρ_1 and ρ_2 are respectively the reflection coefficients of the first and second diopters, which are defined by the following relations:

$$\rho_1(\omega) = \frac{Z_{cd} - Z_c}{Z_{cd} + Z_c} \tag{2.3}$$

$$\rho_2(\omega) = \frac{Z_C - Z_{cd}}{Z_C + Z_{cd}} \tag{2.4}$$

In methods based on multiple reflections, the choice of experimental setup depends primarily on the terminal load placed at the end of the coaxial line, immediately after the sample. Three configurations are commonly used: the short-circuited line, the open line, and the matched line, each with specific characteristics depending on the type of material and the frequency range being studied. In the short-circuited line method, the zero-terminal impedance (Z_t=0) simplifies the analysis but eliminates the contribution of permittivity for small sample thicknesses or low frequencies, making it unsuitable for dielectric characterization while remaining relevant for magnetic materials. The open-line method, which consists of terminating the line only ($Z_t = \infty$) with the sample, is suitable for purely dielectric materials in the low-frequency regime but does not allow access to the permeability of magnetic materials. Conversely, the matched line method ($Z_t = Z_0$) is the most robust approach, as it allows for a direct interpretation of the time-domain signals, provides access to the complex permittivity, and also enables the estimation of electrical conductivity from the asymptotic behavior of the reflection coefficient.

In this work, the objective is to present only the method used in our experimental protocol, which is the matched line method detailed in the following section. The principle of two other configurations is explained in detail in [64, 65].

2.2.4 Adapted Line Method: Principle and Experimental Protocol

The experimental method chosen is that of the adapted line, the appropriate setup of which we anticipate in Figure 2.4. The impedances in the matched measurement line are given by Figure 2.5.

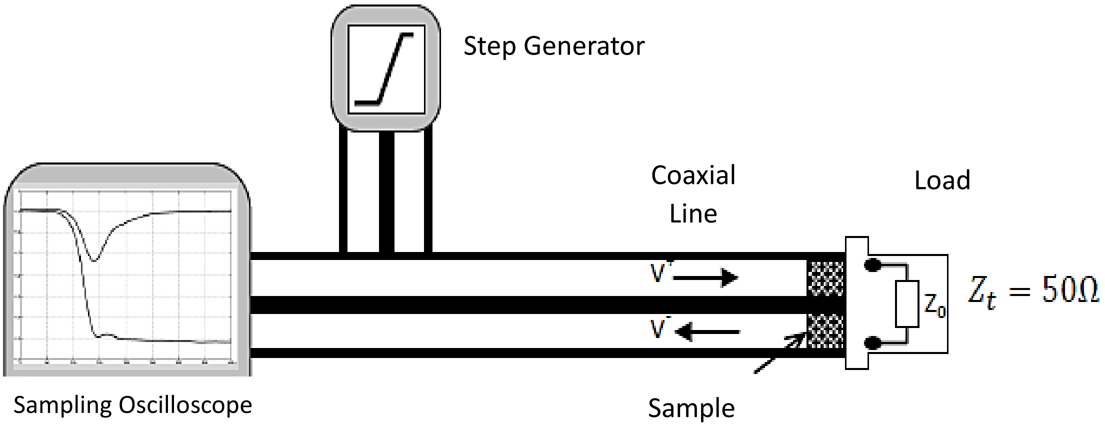

Figure 2.4: Experimental setup of the adapted line.

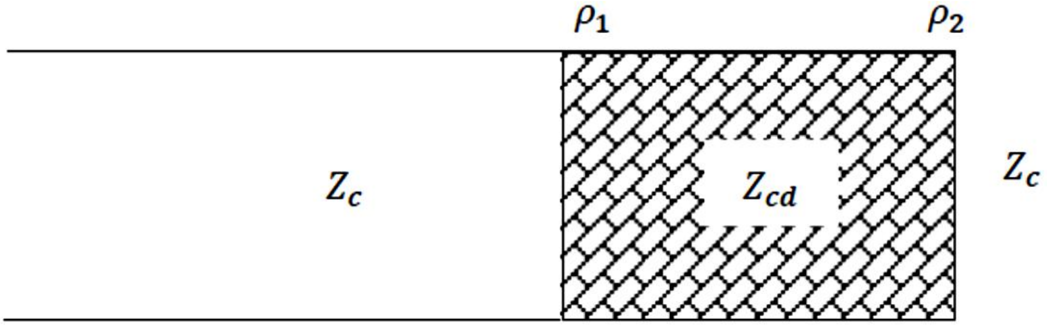

Figure 2.5: The impedances in the adapted measurement line.

In this case, the terminal load is equal to the characteristic impedance of the waveguide: $Z_t = Z_c$ and $\rho_2 = -\rho_1$, where the reflection coefficient can be given by the following expression:

$$R(\omega) = \frac{\rho_1(1-\rho_1 e^{-2\gamma_2 d})}{1-\rho_1^2 e^{-2\gamma_2 d}} \tag{2.5}$$

By introducing the concept of reduced impedance, we obtain:

$$Z(\omega) = \frac{(1+\rho_1)(1-\rho_1 e^{-2\gamma_2 d})}{(1+\rho_1)(1+\rho_1 e^{-2\gamma_2 d})} \tag{2.6}$$

This formula can be expressed as a function of ε_r and μ_r in the following form:

$$Z(\omega) = \sqrt{\mu_r / \varepsilon_r}\,.\frac{1-e^{-2\gamma_2 d}+\sqrt{\varepsilon_r}.(1+e^{-2\gamma_2 d})}{\sqrt{\mu_r}.(1+e^{-2\gamma_2 d})+\sqrt{\varepsilon_r}.(1+e^{-2\gamma_2 d})} \tag{2.7}$$

If we divide the numerator and denominator of the fraction by $(1-e^{-2\gamma_2 d})$ and use the following relation:

$$\tanh(\gamma_2 d) = \frac{1-e^{-2\gamma_2 d}}{1+e^{-2\gamma_2 d}} \tag{2.8}$$

We will obtain the following:

$$Z(\omega) = \sqrt{\mu_r/\varepsilon_r}.\frac{1+\sqrt{\mu_r/\varepsilon_r}.\tanh(\gamma_2.d)}{\sqrt{\mu_r/\varepsilon_r}.\tanh(\gamma_2.d)} \tag{2.9}$$

In the case where $\gamma_2 = j\frac{\omega}{c}\sqrt{\varepsilon_r\mu_r}$ and $\mu_r = 1$, the relation becomes:

$$Z(\omega) = \sqrt{1/\varepsilon_r}.\frac{1+\sqrt{1/\varepsilon_r}.\tanh(j\frac{\omega}{c}.d)}{\sqrt{1/\varepsilon_r}.\tanh(j\frac{\omega}{c}\sqrt{\varepsilon_r}.d)} \tag{2.10}$$

To simplify the calculations, we use admittance instead of impedance, i.e.:

$$Y(\omega) = \frac{1}{Z(\omega)} = \sqrt{\varepsilon_r}.\frac{1+\sqrt{\varepsilon_r}.\tanh(j\frac{\omega}{c}\sqrt{\varepsilon_r}.d)}{\sqrt{\varepsilon_r}.\tanh(j\frac{\omega}{c}\sqrt{\varepsilon_r}.d)} \tag{2.11}$$

To solve this equation, we decompose all complex numbers into real and imaginary parts by setting: $\sqrt{\varepsilon_r} = a + jb$ and $\tanh(j\frac{\omega}{c}\sqrt{\varepsilon_r}.d) = c + jd$. By separating the two parts, real and imaginary, we find:

$$\mathrm{Re}\left[Y(\omega)\right] = \frac{(1+ac-bd)(c+a)-(ad+bc)(d+b)}{(c+a)^2-(d+b)^2} \tag{2.12}$$

$$\mathrm{Im}\left[Y(\omega)\right] = \frac{(1+ac-bd)(d+b)-(ad+bc)(c+a)}{(c+a)^2-(d+b)^2} \tag{2.13}$$

Solving these two equations will give the expressions for $c = f(a,b)$ and $d = g(a,b)$. Substituting them into the equation $\gamma_2 d = c + jd$, will give us the values of *a* and *b*, and therefore the value of $\sqrt{\varepsilon_r}$.

Another approach can be used when ω tends towards 0 (t tends towards infinity) and when $\gamma 2d \ll 1$. In this case, we can approximate the exponential to its first-order Taylor series expansion: $e^{-2\gamma_2 d} \cong 1-2\gamma_2 d$.

This will lead to:

$$R(\omega \to 0) \cong \frac{2\rho_1\gamma_2 d}{1-\rho_1^2+2\rho_1^2.\gamma_2 d} \tag{2.14}$$

By substituting γ_2 and ρ_1 using their respective relation and simplifying the expression, we obtain:

$$R(\omega \to 0) \cong \frac{i.d\frac{\omega}{c}(1-\varepsilon_r)}{2+i.d\frac{\omega}{c}(1-\sqrt{\varepsilon_r})^2} \tag{2.15}$$

For a material with non-zero electrical conductivity, the expression for dielectric permittivity takes the form:

$$\varepsilon_r^*(\omega) = \varepsilon_r^{'}(\omega) - i\,(\varepsilon_r^{''}(\omega) + \frac{\sigma}{\omega\varepsilon_0}) \Rightarrow R(0) = \frac{-\sigma.d/c.\varepsilon_0}{2+\sigma.d/c.\varepsilon_0} \tag{2.16}$$

$$\sigma = \frac{2c.\varepsilon_0}{d}\frac{R(0)}{1+R(0)} \tag{2.17}$$

This approach allows us to easily deduce the electrical conductivity of the material by knowing only the asymptotic value of *R(t)* when t tends towards infinity.

The first advantage of this method is therefore to easily obtain the DC conductivity of the material from the asymptotic value of *R(t)*, and the second advantage is to define a priori and very simply, by simple observation of the time signal, the nature of the type of material to be studied.

This experimental protocol, as can be seen in Figure 2.6, allows the properties of the material (dielectric composite (a) [σ=0, μ=1], or a composite with a non-zero conductivity (b) [$\sigma \neq 0$, μ=1], or a magnetic composite (c) [$\mu \neq 1$, σ=0]) to be visualized directly on the oscilloscope screen.

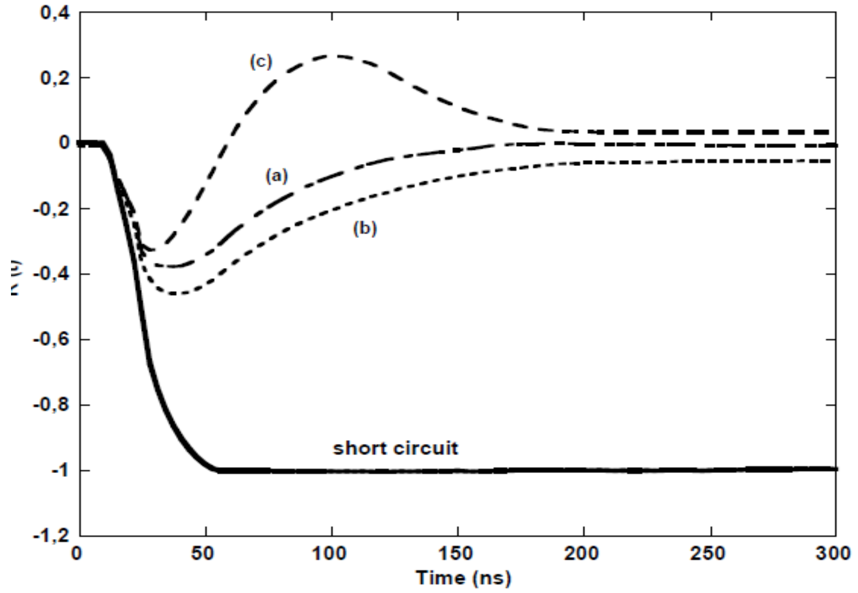

Figure 2.6: Schematic representations of the different time-domain responses adapted to the electromagnetic characteristics of the material.

Before initiating measurements, the entire reflectometry system is run for more than four hours to ensure thermal stability and optimal acquisition accuracy. To improve the signal-to-noise ratio, each reflected response is obtained by averaging several successive recordings for each sample [31].

Time-domain reflectometry (TDR) measurements are performed according to the following procedure for all samples studied. First, a short circuit is placed at the end of the measurement cell, and the corresponding response is recorded. Then, the sample is inserted into the cell, the matched load is positioned at the termination, and the associated TDR response is acquired [64].

The time-domain reflectometry system then implements the operational sequence described in [65].

1) A voltage step with a very short rise time (approximately 28 ps) is injected into a matched coaxial line terminated by the sample. The impedance discontinuity introduced by the sample generates a reflected wave.
2) The sampling head converts the superposition of the incident and reflected waves into a low-frequency signal, which is displayed by a digital sampling oscilloscope.
3) The resulting time-domain signal is recorded and then digitally processed to extract the desired information. Several processing steps are necessary to obtain the final results.

The signal processing methods used in this work, as well as their theoretical justification, are presented in detail in references [64].

2.3 Microwave Propagation in A Rectangular Waveguide [66-68]

The rectangular waveguide used in this study is a hollow metallic conduit designed to confine and direct the propagation of electromagnetic waves. The dimensions of this waveguide are chosen to allow signal propagation in the frequency band between 8.2 and 12.4 GHz, known as the X-band.

Propagation in such a waveguide does not occur as a classical plane wave, but rather according to natural modes, which are solutions to Maxwell's equations associated with the boundary conditions imposed by the conductive walls. Among the various possible modes, the TE_{10} (Transverse Electric) mode is the most commonly used, as it exhibits the lowest attenuation and constitutes the fundamental mode of the rectangular waveguide.

In a perfectly conductive waveguide, the boundary conditions require that the electric field be perpendicular to the metallic walls, while the magnetic field be tangent to them. These conditions prevent the propagation of a TEM mode, and only TE (Transverse Electric) or TM (Transverse Magnetic) waves can exist.

The minimum frequency at which a given mode (m,n) can propagate is called the cutoff frequency. Below this frequency, the wave does not propagate and its amplitude decreases exponentially; it is given by:

$$f_{c(m\,n)} = \frac{1}{2\pi\sqrt{\mu\varepsilon}}\sqrt{(\frac{m\pi}{a})^2 + (\frac{n\pi}{b})^2} \tag{2.18}$$

where:

- a and b are the internal dimensions of the waveguide ($a>b$),
- μ and ε are respectively the permeability and permittivity of the medium in the waveguide.

For the fundamental mode TE_{10} ($m=1$, $n=0$) :

$$f_{c10} = \frac{c}{2a} \tag{2.19}$$

Therefore, the corresponding cutoff wavelength is:

$$\lambda_{c10} = 2a \tag{2.20}$$

The wavelength in the waveguide, denoted λ_g, is related to the wavelength in free space $\lambda_0 = c/f$ by the relation:

$$\lambda_g = \frac{\lambda_0}{\sqrt{1 - \left(\frac{\lambda_0}{\lambda_c}\right)^2}} \tag{2.21}$$

This wavelength is always greater than the wavelength in air. λ0, and becomes infinite at the cutoff frequency ($f = f_c$), which means that the wave no longer propagates.

The propagation constant in the waveguide is written as:

$$\gamma_g = \alpha_g + j\beta_g = j\frac{2\pi}{\lambda_0}\sqrt{1 - \left(\frac{f_c}{f}\right)^2} \tag{2.22}$$

where:

- β_g is the phase constant,
- α_g is the attenuation constant (zero for a perfect empty waveguide).

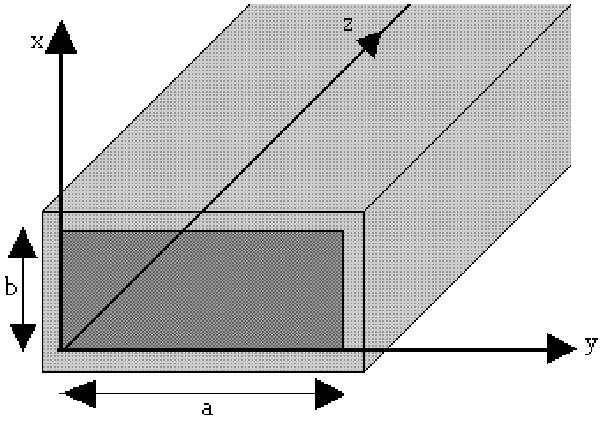

Figure 2.7: Diagram of the rectangular waveguide.

2.3.1 Determination of Complex Permittivity

The electromagnetic characterization of dielectric materials in rectangular waveguides relies on analyzing the behavior of a microwave propagating within the waveguide when it is loaded by a sample. The main objective of this method is to determine the complex permittivity from experimental measurements using the fixed-frequency short-circuited line technique proposed by Von Hippel.

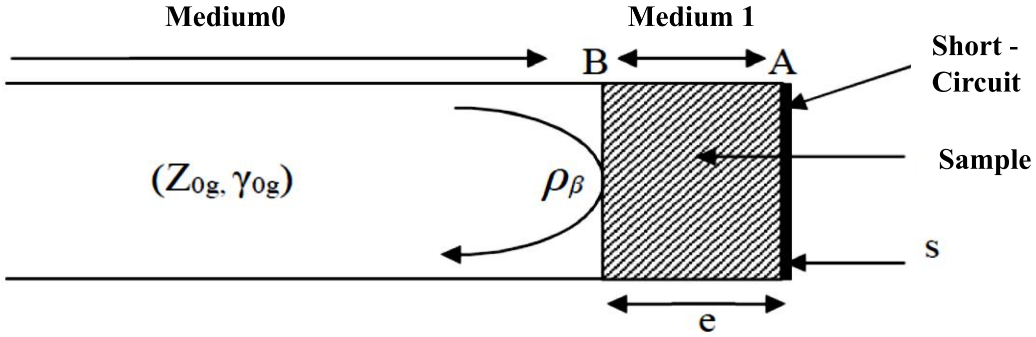

Figure 2.8: Waveguide filled by the dielectric and short circuit.

Figure 2.8 represents the theoretical model of a waveguide filled with a dielectric and terminated by a short circuit. It consists of two distinct media:

- **Medium 0** corresponds to the air-filled (or vacuum) portion of the waveguide. In this region, losses are assumed to be negligible, therefore:

  $$\alpha_{0g} = 0 \tag{2.23}$$

  Propagation is then entirely reactive, described by the propagation constant and the characteristic impedance of the air-filled waveguide. These two quantities are given by the following relationships:

  $$\gamma_{0g} = j\beta_{0g} = j\frac{2\pi}{\lambda_{0g}} \tag{2.24}$$

  $$Z_{0g} = \frac{Z_0}{\sqrt{1-\left(\frac{f_c}{f}\right)^2}} \tag{2.25}$$

- **Medium 1:** the region of the waveguide containing the dielectric sample of thickness e, characterized by γ_{1g} and Z_{1g}; given by:

$$\gamma_{1g} = j\frac{2\pi}{\lambda_0}\sqrt{\varepsilon_r^* - \left(\frac{f_c}{f}\right)^2} \tag{2.26}$$

$$Z_{1g} = \frac{Z_0}{\sqrt{\varepsilon_r^* - \left(\frac{f_c}{f}\right)^2}} \tag{2.27}$$

Where: ε_r^* is the relative complex permittivity of the dielectric material.

For non-magnetic media ($\mu_r = 1$), the $Z_g\gamma_g$ product remains invariant:

$$Z_{1g}\gamma_{1g} = Z_{0g}\gamma_{0g} = j\omega\mu_0 \tag{2.28}$$

So,

$$\frac{Z_{1g}}{Z_{0g}} = \frac{\gamma_{0g}}{\gamma_{1g}} = j\frac{2\pi}{\lambda_{0g}}\frac{1}{\gamma_{1g}} \tag{2.29}$$

At **point A**, corresponding to the plane of the short circuit, the physical impedance is zero ($Z_A = 0$) since the tangential electric field is zero. The reduced impedance is therefore also zero.

The associated reflection coefficient is then:

$$\rho_A = -1 \tag{2.30}$$

This corresponds to total internal reflection with phase inversion. However, the reflection measured at the entrance of the waveguide differs, as it undergoes a transformation during propagation over the distance separating plane A from the observation point.

At **point B**, the system impedance is given by:

$$Z_B = Z_{1g}\tanh(\gamma_{1g}e) \tag{2.31}$$

From this expression, it is possible to define two forms of reduced impedances allowing the impedance to be normalized with respect to the chosen reference medium:

- The reduced impedance at point B with respect to the material:

$$z_{B1} = \frac{Z_B}{Z_{1g}} = \tanh(\gamma_{1g}e) \tag{2.32}$$

- Reduced impedance at point B relative to the empty waveguide:

$$z_{B0} = \frac{Z_B}{Z_{0g}} = \frac{Z_{1g}\tanh(\gamma_{1g} e)}{Z_{0g}} \tag{2.33}$$

By substituting the expressions of equations (2.26) and (2.29) into equation (2.33), we obtain:

$$z_{B0} = j\frac{2\pi}{\lambda_{0g}} \frac{\tanh(2\pi e\sqrt{\frac{1}{\lambda_c^2} - \frac{\varepsilon^*}{\lambda_0^2}})}{2\pi e\sqrt{\frac{1}{\lambda_c^2} - \frac{\varepsilon^*}{\lambda_0^2}}} \tag{2.34}$$

When a material is inserted, the standing waves move. At the minimum electric field strength, the measured impedance is:

$$Z_m = Z_{0g}\frac{1-|\rho_B|}{1+|\rho_B|} = \frac{Z_{0g}}{\theta} \tag{2.35}$$

Since we are working with reduced impedances, we define:

$$z_m = \frac{Z_m}{Z_{0g}} = Z_{0g}\frac{z_{B0} - \tanh(\gamma_{0g} dm)}{1 + z_{B0}\tanh(\gamma_{0g} dm)} = \frac{1}{\theta} \tag{2.36}$$

So,

$$z_{B0} = \frac{1 + j\theta\tan(2\pi d_m / \lambda_{0g})}{\theta - j\tan(2\pi d_m / \lambda_{0g})} \tag{2.37}$$

Where dm is the distance between the minimum of the field and the plane passing though by B, and θ correspond to the standing wave ration (SWR).

From equations (2.34) and (2.37), we deduce the equation (2.28) which relates the complex permittivity of the material to the quantities measured experimentally $(\theta, d_m, \lambda_{0g}, \lambda_c, e)$ within the framework of the short-circuited line method.

$$\frac{\tanh\left(2\pi e\sqrt{\frac{1}{\lambda_c^2} - \frac{\varepsilon^*}{\lambda_0^2}}\right)}{2\pi e\sqrt{\frac{1}{\lambda_c^2} - \frac{\varepsilon^*}{\lambda_0^2}}} = -j\lambda_{0g}\frac{1 + j\theta\tan(2\pi dm / \lambda_{0g})}{\theta - j\tan(2\pi dm / \lambda_{0g})} \tag{2.38}$$

2.3.2 Experimental Measurement by X-band Waveguide Bench

When the waveguide is empty and terminated by a metallic short circuit, the propagation of a microwave wave generates standing waves, characterized by maxima and minima of the electric field along the guide. The insertion of a dielectric sample modifies this distribution due to partial reflections at the air-material interface and propagation within the material. This perturbation of the standing waves forms the basis of the measurement. The observed variations in the position of the minima and maxima allow the measurable quantities to be experimentally related to the complex permittivity of the material.

The experimental setup shown as a bloc diagram in Figure 2.9 includes a microwave generator injecting the signal into the waveguide, a detector for measuring the electric field along the waveguide, and an attenuator to control the amplitude. The end of the waveguide is closed by a metallic short circuit, and the sample is placed directly against this short circuit. The measurement consists of recording the position of the electric field minima with and without the sample.

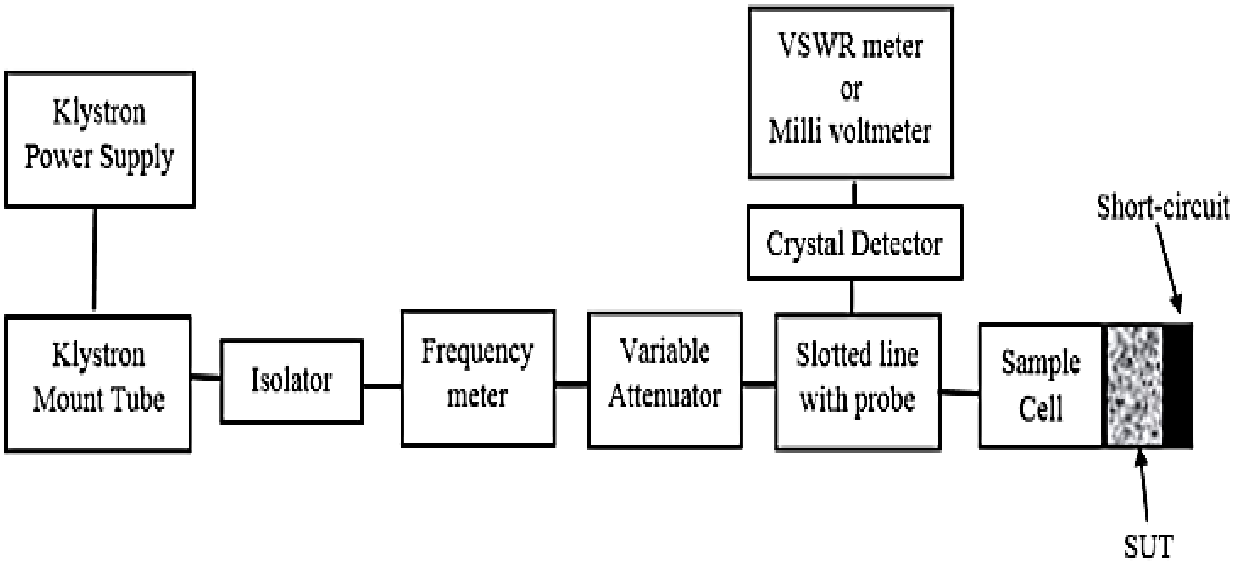

Figure 2.9: Bloc diagram of X-band waveguide bench.

The displacement of the minima, denoted d_m, is given by:

$$d_m = X_m^{'} - X_m + e \tag{2.39}$$

where $X_m^{'}$ and X_m are the positions of the minimum with and without the sample, and e is the thickness of the sample. The measurement principle of dm is shown in Figure 2.10.

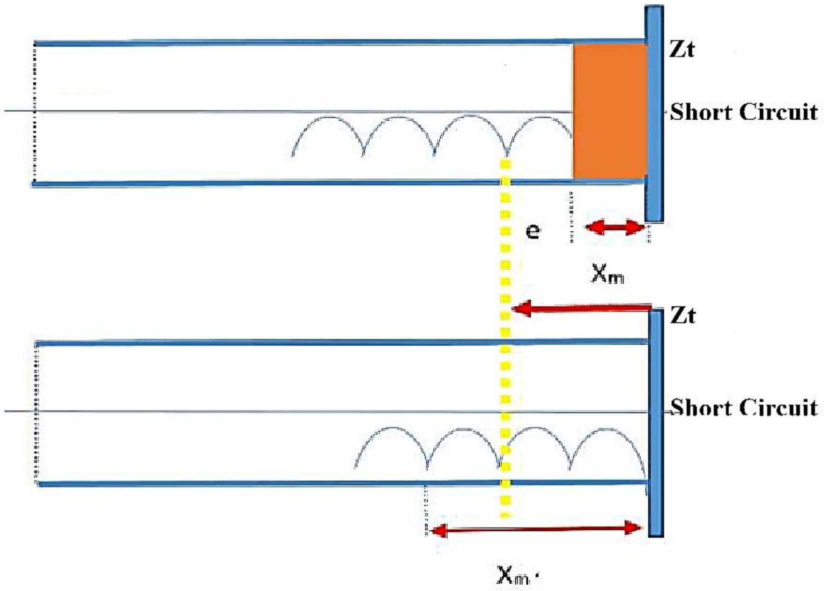

Figure 2.10: Principle of measuring the distance from the minimum d_m with and without the sample.

The determination of λ_{0g} is direct. It suffices to measure the distance between two minima, either in the case of the short circuit (m'_1, m'_2) or with the sample (m_1, m_2):

$$\frac{\lambda_{0g}}{2} = \left(m_2^{'} - m_1^{'}\right) = \left(m_2 - m_1\right) \tag{2.40}$$

The standing wave ratio (SWR), is defined as the ratio between the maximum and minimum amplitudes of the electric field in the waveguide:

$$SWR = \theta = \frac{V_{\max}}{V_{\min}} = \frac{1+|\rho|}{1-|\rho|}, \quad |\rho| = \frac{\theta - 1}{\theta + 1} \tag{2.41}$$

With $1 \leq \theta \leq \infty$

ρ: The charge reflection coefficient.

$V_{\max}$: The maximum voltage value.

$V_{\min}$: The minimum voltage value.

2.4 Numerical Characterization Methods

The introduction of numerical methods into the design process of new composite materials is becoming essential for studying the properties of these heterogeneous structures. Numerical modeling is becoming a necessary step for the "virtual" fabrication of heterogeneous structures before they are tested in the laboratory. It allows us to avoid unsuccessful synthesis methods. This is all the more true given that previously proposed analytical approaches all rely on approximations that limit their application. Their transferability and universality also pose an unresolved problem. The spatial disorder of heterogeneities, their shapes, their orientations relative to the external electric field, their potential interactions, and their concentrations constitute a set of parameters that can each be considered independently by numerical simulation in order to assess their influence. This undoubtedly represents yet another advantage of numerical methods.

In our work, we use the finite element method (FEM) [69-71] in order to be able to use it to evaluate the effective permittivity of random composite materials. The advantage of this method lies in the fact that it allows the simulation of highly heterogeneous structures.

2.4.1 Finite Element Method (FEM)

The finite element method (FEM) [72] is one of the numerical tools that has proven effective in a wide variety of fields (electromagnetism, mechanics, thermodynamics, etc.). This method is one of the most widely used today for solving partial differential equations, particularly Maxwell's equations, which govern electromagnetic phenomena. It is based on the finite element approximation technique [73], which allows us to approximate a polynomial function in a given space using the values at certain nodes of the domain. This requires dividing the domain of study of these functions into elementary subdomains called elements. These local functions have the advantage of being simpler than those that could potentially be used to represent the entire computational domain. Thanks to the diversity of elements that can be used, notably triangles in 2D or tetrahedra in 3D, this method is very common for modeling complex geometries. The repetitive nature of the method, which involves applying the same operator to each element, has made it very efficient. This method requires specific treatment of the equations, which are transformed using an integral formulation and then discretized to arrive at a system of algebraic equations. The method is robust but generally requires significant computational resources.

In this method, the focus is not on solving the equation (for example, Laplace's equation), but rather on a variation problem associated with the principle of minimum energy in a closed region of the electrostatic field. The energy stored in the field always takes the lowest possible value. The region of the electric field under consideration is divided into elements of arbitrary shapes and sizes (Figure 2.11).

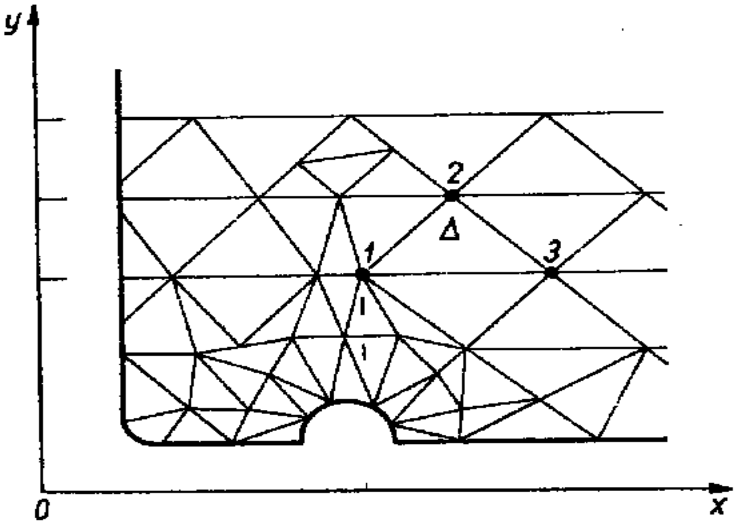

Figure 2.11: Fragment of the field with the mesh intended for calculations using the finite element method.

The FEM method uses a parts-based approximation of the unknown function to solve a differential equation. Physical equivalence can be used to find a solution to the partial differential equation. However, the complexity of the geometries of the systems considered makes it very difficult, if not impossible, to find an approximation of the solution across the entire domain. To overcome this difficulty, the domain is subdivided into subdomains called finite elements, on which interpolation is performed locally to approximate the unknown function. The domain is bounded by a boundary where the potential value is assumed to be known. The finite elements used to discretize the domain are generally grouped into topological families: line segments, triangles, quadrilaterals, tetrahedra, parallelepipeds, and prisms. Each element is represented by points called geometric nodes. Interpolation nodes, where the unknown function will be calculated, are associated with each element. Thus, for each element resulting from the subdivision, the function modeling the phenomenon is defined by a polynomial interpolation [2].

$$V = \sum_{i=1}^{n} \lambda_i V_i \tag{2.42}$$

n is the number of interpolation nodes; λ_i are the interpolation functions and V_i are the nodal values.

The basic principle is to find the distribution of nodal values λ_i that satisfy the partial differential equations and the boundary conditions. This can be done either by a variational method that minimizes a function equivalent to the posed differential problem, or by using a projection method such as the Galerkin projection, which directly addresses the partial differential equation. The order of the polynomial depends on the type of element; for example, for a one-dimensional quadratic element described by the curvilinear abscissa μ located in the interval [-1, 1], the interpolation functions are [74].

$$\begin{aligned} \lambda_1(\mu) &= \frac{1}{2}\mu(\mu-1) \\ \lambda_2(\mu) &= 1-\mu^2 \\ \lambda_3(\mu) &= \frac{1}{2}\mu(\mu+1) \end{aligned} \tag{2.43}$$

Consider, for example, the Poisson equation. We are looking for an approximation V' of V that minimizes the quantity R:

$$R = (\Delta V' + \frac{\rho}{\varepsilon_0 \varepsilon}) \tag{2.44}$$

where ρ is the volume charge density.

Among the methods for setting a given quantity to zero in a domain, the weighted residuals method is often used. A system of independent linear functions W_n, called projection functions, is chosen, and then all integrals (Eq. 2.45) are set to zero at each finite element.

$$I_n = \int_\Omega W_n R d\Omega \tag{2.45}$$

This yields a comprehensive formulation of the finite element method. Sub-methods of the weighted residual method also exist (point-by-point collocation, subdomain collocation, Galerkin, least squares), depending on the choice of weighted functions.

$$\lambda_i(\mu) = W(\mu) \tag{2.46}$$

For each element, we set to zero the n integrals (Eq. 2.45) corresponding to the n projection functions. This system of equations can be written in matrix form:

$$A_e\overrightarrow{V_e} = \vec{b}_e \tag{2.47}$$

with Ae being the matrix associated with the element under consideration, whose coefficients depend on the coordinates of the element's nodes. The components of V_e are the unknowns at the nodes of the same element. The vectors take into account any boundary conditions at certain nodes of the element under consideration. Writing Eq. 2.47 for all elements, we obtain a series of algebraic equations, among which is the potential solution in the domain studied [2].

Numerous commercial software packages (Comsol Multiphysics, HFSS, etc.) are available for modeling complex three-dimensional structures, particularly through adaptive meshing. The functions used are functionals constructed with respect to potentials or electromagnetic fields.

We used the FEM method to evaluate the effective permittivity of composite materials containing inclusions of arbitrary shape. We briefly describe the principle of its application to heterogeneous structures below.

2.4.2 Application to composite materials

The FE method has been widely used for modeling random or periodic, linear or nonlinear, lossless or lossless composite materials, in both 2D and 3D cases. This method has been employed by various authors [75] for calculating the complex effective permittivity of composite materials by solving the Laplace equation and using appropriate boundary conditions.

In the numerical approach we developed, we used the COMSOL Multiphysics finite element code [76], which integrates all the functions of the MATLAB software for developing quasistatic models and solving them.

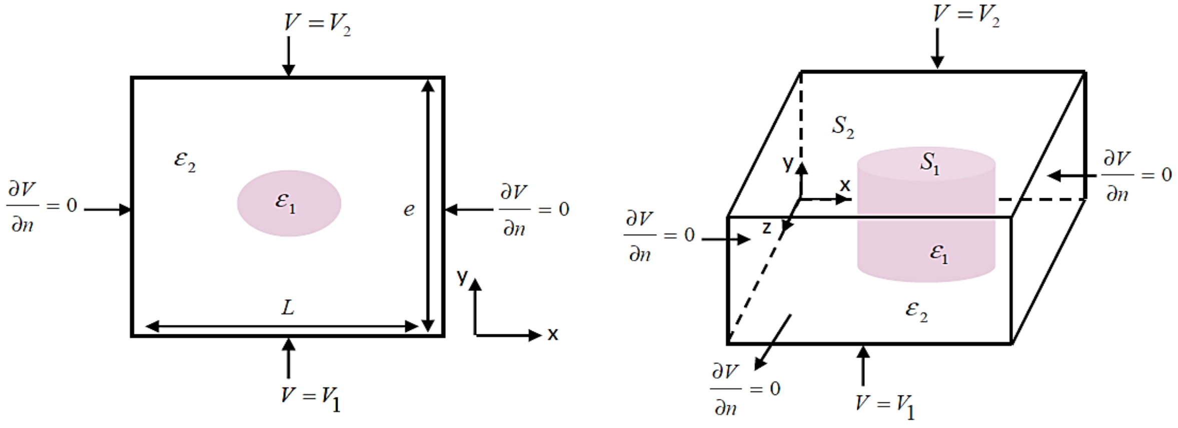

(a) *(b)*

Figure 2.12: Modeling of a composite: *(a)* 2D, *(b)* 3D.

Let us first consider the case of a lossless periodic structure. Consider a two-phase periodic dielectric composite containing an inclusion of arbitrary shape in a matrix. Taking into account the symmetry and periodicity properties, the geometry of the material is reduced to an elementary cell, as shown in Figure 2.12, which is approximated by a parallel-plate capacitor.

The calculation of the effective permittivity of 2D composite structures proceeds in three steps: (1) definition of elementary cells containing a grid of points allowing a good approximation of the spatial domain. The space is filled with the desired arrangement, i.e., the effective permittivities of the cells are equal to ε_1 or ε_2 depending on whether the cell is filled with phase 1 or phase 2; (2) calculation of the local potential distribution within the cell, where there are neither free charges nor currents, obtained by solving Eq. 2.48.

$$\vec{\nabla}.(\varepsilon(r)\vec{\nabla}V(r)) = 0 \tag{2.48}$$

Where $\varepsilon(r)$ and $V(r)$ denote the local permittivity and potential.

The electrostatic energy can be calculated from the values of the derivatives of the potential V at the nodes of the mesh over the entire surface S of the composite using the equation:

$$E_e = \frac{1}{2}\iint_s \varepsilon(x,y)\left[\left(\frac{\partial V}{\partial x}\right)^2 + \left(\frac{\partial V}{\partial y}\right)^2\right]dxdy \tag{2.49}$$

The effective permittivity in the direction of the applied electric field, i.e., $\varepsilon = \varepsilon_y$, is obtained by the continuity condition of the normal component of the electric displacement vector via:

$$\int_s \varepsilon_1\left(\frac{\partial V}{\partial n}\right)_1 = \varepsilon\frac{V_2 - V_1}{L}S \tag{2.50}$$

where $V_2 - V_1$ represents the potential difference imposed in the y direction, L is the thickness of the composite in the same direction, and S denotes the "surface" of the unit cell that is perpendicular to the applied field. The potential on the top of the structure is set to $V_2 = 1V$, while on the other face V_1 is taken to be $0V$; and (3) automatic or semi-automatic mesh generation performed by the Comsol Multiphysics software.

As we recalled in Chapter 1, the interaction of an electromagnetic field with a homogeneous and isotropic dielectric material can be characterized by a (relative) permittivity described by a complex number $\varepsilon = \varepsilon' - j\varepsilon''$. The calculation of ε' and ε'' is easily generalized from the previous evaluation of ε as follows:

For a dielectric medium, the numerical solutions of the electrostatic problem are based, in the general case, on solving Poisson's equation:

$$\vec{\nabla}.(\varepsilon\varepsilon_0\vec{\nabla}V) = -\rho \tag{2.51}$$

If the medium is conductive, with no free charges or sources, the solution to the problem is given by solving:

$$\vec{\nabla}.(\sigma\vec{\nabla}V) = 0 \tag{2.52}$$

with σ defining the conductivity of the medium.

When the medium considered is intermediate between the two limiting cases considered previously (medium with dielectric losses), then the solution to the problem depends on time, and is given by a complex electrical potential that satisfies the continuity equation:

$$\vec{\nabla}.(\sigma\vec{\nabla}V) + \vec{\nabla}.\left(\frac{\partial}{\partial t}(\varepsilon\varepsilon_0\vec{\nabla}V)\right) = 0 \tag{2.53}$$

or equivalently in Fourier space (taking a harmonic potential proportional to exp(jωt)), considering a medium without free charges, by

$$\vec{\nabla}.(j\varepsilon_0\varepsilon(\omega)\omega\vec{\nabla}V) = 0 \tag{2.54}$$

Eq. 2.54, is analogous to Eq. 2.48, by setting $\varepsilon = \varepsilon' - j\varepsilon''$, with $\varepsilon'' = \sigma/\omega\varepsilon 0$

2.4.3 FEM Mesh

Generating a high-quality mesh plays a crucial role in finite element analysis. This is achieved using the COMSOL MultiPhysics software. COMSOL MultiPhysics allows for the controlled generation of finite element meshes using input files containing complete instructions with node-by-node and element-by-element mesh characteristics. This results in a mesh that is both fine enough to guarantee high-quality convergence and sufficiently reduced to obtain results with limited resources and time. COMSOL MultiPhysics also allows the use of both unstructured meshes (triangles in 2D (Figure 2.13), tetrahedra in 3D) and structured meshes. In 2D, structured meshes are composed of quadrangles [75]. Meshing surfaces is one of the essential steps in modeling heterogeneous materials. This step transforms the surfaces from outlines into elementary surfaces. It's worth noting that a manual mesher can be used, where surfaces are meshed either one by one, i.e., surface by surface, or all at once. The COMSOL MultiPhysics software includes an automatic mesher that generates quadrilateral or triangular elements. The mesh is then refined by propagating one or more mesh lines and/or by dividing the mesh elements.

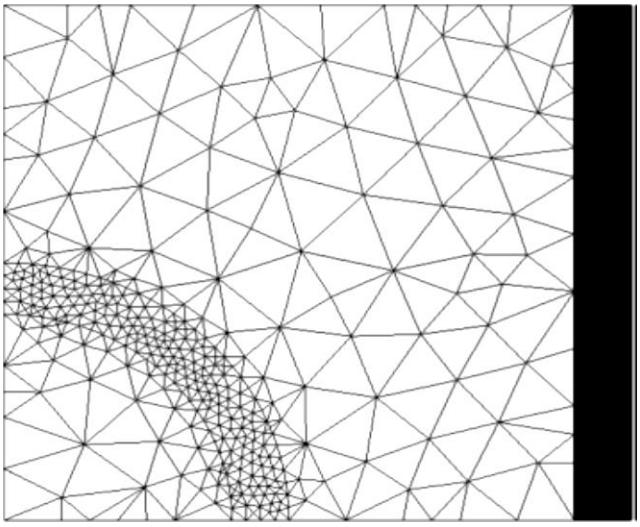

Figure 2.13: 2D unit cell mesh.

2.5 Conclusion

In this chapter, we presented and examined the two experimental techniques used for the electromagnetic characterization of dielectric materials. The first, based on time-domain reflectometry (TDS), relies on the matched line method and proves particularly relevant for studying dielectric composites over a wide frequency range. Thanks to the use of broadband pulsed signals, this approach allows for the rapid and robust extraction of electromagnetic parameters.

The second technique studied is based on the use of a rectangular X-band waveguide. We detailed its principle and the experimental parameters required for estimating the complex permittivity. Commonly used in the microwave regime, this method offers high accuracy in determining dielectric properties, notably through the equivalent impedance model and the exploitation of the reflection coefficient.

Furthermore, a numerical calculation tool based on the finite element method was presented. Its formulation principle and its contribution to the determination of permittivity in heterogeneous materials have been explained.

Thus, this chapter has laid the theoretical and methodological foundations necessary for all the experimental and numerical analyses carried out in this work. The following chapter will focus on the procedure for preparing the samples studied and will present, analyze, and interpret the results obtained using the two experimental characterization techniques introduced here.

CHAPTER

3

Experimental Results and Modeling of Binary and Ternary Composites

3.1 Introduction

In this chapter, we present our contribution to the study and characterization of two types of titanate-based composites. The first is a binary composite consisting of an epoxy resin matrix and barium titanate, while the second is a ternary composite combining the same matrix with calcium titanate and ferrite.

The chapter is organized into three main sections. The first section describes the materials used and the sample preparation protocols for the measurements. The second section presents a comparative analysis of the dielectric properties obtained using two experimental techniques: an X-band bench operating at 9.49 GHz and time-domain spectroscopy covering the range from 0 to 9.49 GHz. Several theoretical mixing models are also applied to determine which best reproduces the experimental results.

Finally, the third section presents the experimental results for the ternary composite, covering the microwave range from DC to 5 GHz as well as low-frequency measurements (500 MHz). This approach makes it possible to link the dielectric characteristics to the charge concentrations and the structure of the composites, thus providing a comprehensive overview of the electrical behavior of these materials.

3.2 Fabrication and Preparation of Composites

This section details the procedures for preparing samples to be characterized using the two measurement benches (TDS, X-band). The objective is to describe the composite materials used, their formulations, and the shaping methods adopted, in order to obtain composites that are compatible with the measurement devices used.

3.2.1 Materials Used

The composites studied in this work are binary and ternary composites consisting of a thermosetting polymer matrix and a ceramic filler. The matrix used for both composites is an epoxy resin (Figure 3.1(a)), composed of a resin-hardener mixture [77] that ensures the mechanical cohesion of the composite and the uniform coating of the filler grains. The ceramic filler consists of Barium Titanate ($BaTiO_3$) (Figure 3.1(b)) for the binary composite, and Calcium Titanate ($CaTiO_3$) (Figure 3.1(c)) with Manganese-Zinc Ferrite (MnZn Fe_2O_4) (Figure 3.1(d)) for the ternary composite.

(a)

(b)

(d) (c)

Figure 3.1: Materials used in the composition of binary composites: (a) Epoxy resin, (b) Barium titanate, (c) calcium titanate, (d) Manganese-Zinc Ferrite.

The composites were manufactured at the LIS laboratory, Ferhat Abbas University, Setif 1. The minimum resin volume fraction was set at 70% to ensure good shaping, sufficient mechanical stability, and limited filler agglomeration. The formulations studied differ in the volume fraction of BaTiO3, which was increased in regular 5% increments to progressively examine the effect of ceramic concentration on dielectric properties. Table 3.1 lists all the prepared compositions with their corresponding volume percentages and the main properties of the constituents.

Table 3.1 Main materials used in the experiment.

MATERIALS		**EPOXY RESIN**	**BARIUM TITANATE**	**CALCUIM TITANATE**	**MANGANESE-ZINC FERRITE**
Chemical Formula		-	BaTiO3	CaTiO3	MnZn Fe_2O_4
Physical proprieties		Transparent, viscous liquid, excellent adhesive properties, high strength after curing.	White powder, high permittivity, ferroelectric properties, electrical resistivity, Perovskite	White powder, Moderate permittivity, electrical resistivity, Perovskite	Black powder, soft magnetic, high permeability, low coercivity, spinel
Density [g/cm3]		1.07	6.02		
Particle size		-	< 3 µm	< 100 nm	< 5 µm
Materials concentration		RE (%)	BT (%)	CT(%)	FE(%)
Binary Sample code	RB0	100	0	---	----
	RB1	95	5		
	RB2	90	10		
	RB3	85	15		
	RB3	80	20		
	RB5	75	25		
	RB6	70	30		
Ternary Sample code	RCF01	70	----	0	30
	RCF02	70		2.5	27.5
	RCF03	70		5	25
	RCF04	70		7	22.5
	RCF05	70		10	20
	RCF06	70		12.5	17.5
	RCF07	70		15	15
	RCF08	70		17.5	12.5
	RCF09	70		20	10
	RCF10	70		22.5	7.5
	RCF11	70		25	5
	RCF12	70		27.5	2.5
	RCF13	70		30	0

3.2.2 Determination of Volume Fraction

Determining the volume fractions is a crucial step, as the mixing laws used in this study depend directly on the volumes of the constituents. For powdered materials, such as barium titanate, direct volume measurement is impossible; therefore, it is obtained from the mass using the material's density. The procedure begins by establishing the total volume (V_{tot}) of the sample, defined according to the mold dimensions. Once this volume is established, the matrix volume fraction (F_{matrix}) is selected, which allows the required resin volume to be deduced based on:

$$V_{matrix} = V_{tot} . F_{matrix} \tag{3.1}$$

The same approach is applied to the ceramic filler. Starting with the fixed volume fraction F_{filler} of the filler, the corresponding volume is calculated by:

$$V_{filler} = V_{tot} . F_{filler} \tag{3.2}$$

Since the filler is in powder form, its volume is then converted into mass using its density, according to the following relationship:

$$M_{filler} = \rho_{filler} . V_{filler} \tag{3.3}$$

The use of these equations ensures correct formulation of volume fractions, and the different masses of powders are weighed using a precision electronic balance (1mg), thus ensuring the accuracy of the quantities introduced and the reproducibility of the samples obtained.

3.2.3 Samples Preparation

The manufacturing technique used, as described in Figure 3.2, is the hand-pouring method, the most traditional and simplest method for molding composites. It always involves the following three steps: mixing, polymerization, and shaping.

The different stages of preparing epoxy-based composite samples are as follows:

- The resin, consisting of one volume of pure epoxy resin and the same volume of hardener, is poured into a container.
- The two products are thoroughly mixed until they form a single viscous liquid. Air bubbles will appear and be expelled by the resin.
- Next, the desired BaTiO3 ceramic fillers are added, and the mixture is thoroughly mixed until no isolated grains remain.
- The mixture is then stirred for an extended period to achieve maximum homogeneity, ensuring a uniform distribution of the BaTiO3 grains. The resin must completely coat the

powder. It should be noted that the mixing phase determines the homogeneity of the final product. After that, a vacuum degassing chamber will be used to remove any air bubbles trapped during mixing.

- Then, the mixture is gently poured into the appropriate molds, after their interior walls have been coated with a layer of wax to facilitate later demolding. The first mold is a rectangular parallelepiped used for the waveguide, and the second is a hollow cylindrical shape (Figure 3.3) for the TDS device.

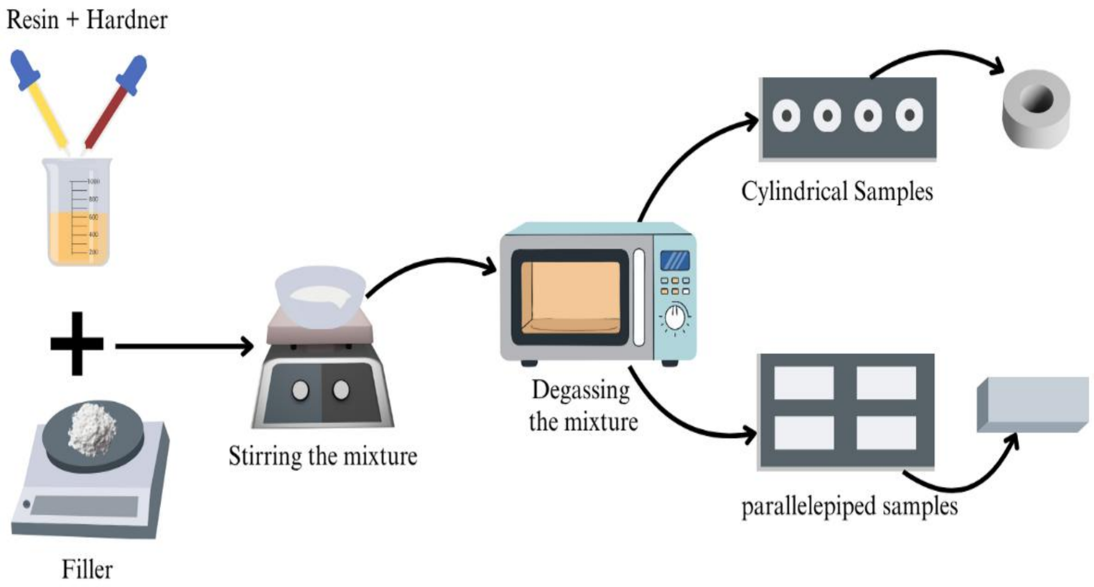

Figure 3.2: Main steps in a sample manufacturing process by molding.

The filler powder grains are bonded after the epoxy resin polymerizes, which must coat all of these grains. The use of the resin, which replaces the air space between the grains, allows for precise control of the volume of this phase of the composite (Figure 3.4).

Due to the high viscosity of the mixture, especially with high filler volume fractions, it is poured into the mold, aiming for a uniform spatial distribution. Once poured, the mixture is left for over sixteen hours until the resin has fully polymerized. During this time, the degassing of air bubbles can be observed. Using a vibrator would have helped to eliminate these bubbles from the mixture. Once the resin has fully polymerized and the mixture has hardened, it is carefully demolded. This results in a relatively hard composite material, ranging in color from cream to yellowish-white, depending on the filler concentration. As the filler volume fraction increases, it becomes more difficult for the resin to retain the grains, eventually saturating the resin. The viscosity of the mixture increases, creating further difficulties in its flow through the mold. This constraint essentially determines the maximum filler fraction that cannot be exceeded.

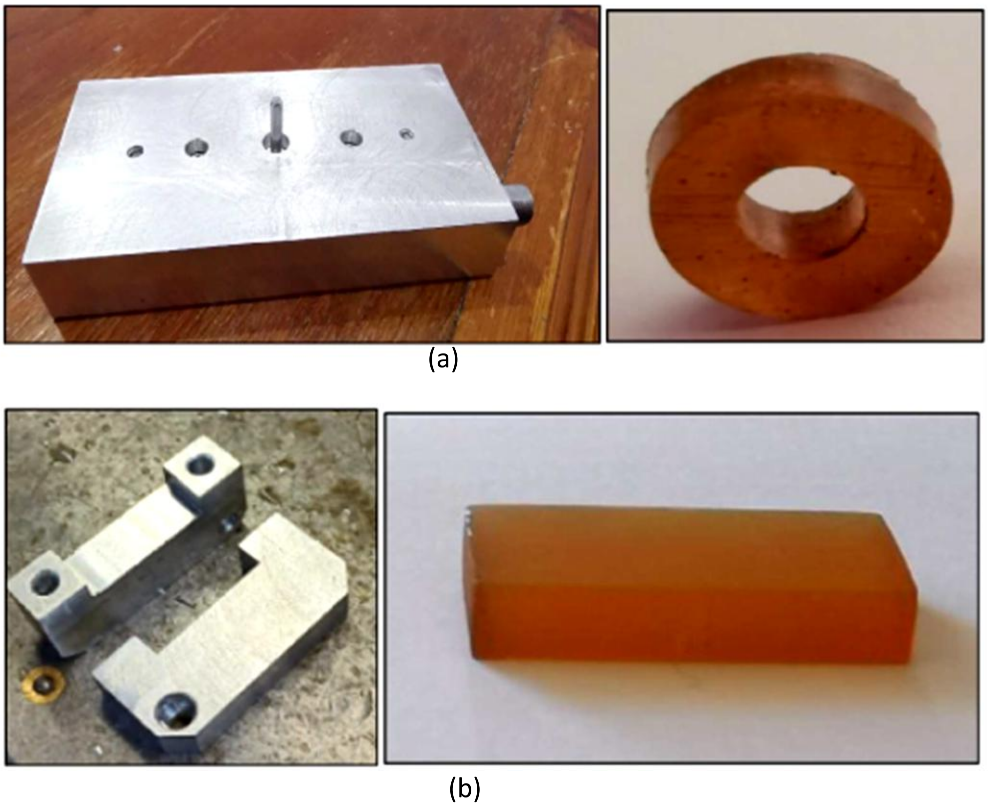
(a)

(b)

Figure 3.3: (a) Mold and Sample of pure resin (7x3 mm) for TDS bench, (b) Mold and Sample of pure resin (22,86x10,16mm) for X-band rectangular bench.

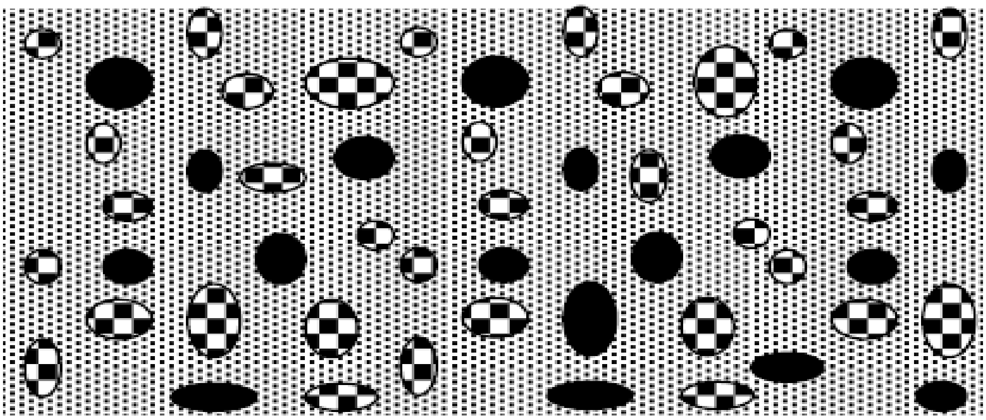

Figure 3.4: Representation of Inclusions (Loads) in the Host Matrix (Resin).

3.3 RE-BT Binary Composite

This section presents a collaborative research project that resulted in the publication of a scientific article and several presentations at national and international conferences. Our contribution focuses on the characterization and modeling of a set of binary composite samples made of epoxy resin and barium titanate RE-BT. The main objective of this work is to compare the dielectric properties obtained at a fixed frequency of 9.49 GHz from measurements performed on an X-band microwave test bench (MTB) with those obtained from time-domain spectroscopy (TDS). TDS covers a frequency range from direct current up to 9.49 GHz and is distinguished by a nearly invariant response to field length, characteristic of a practically flat spectrum. Furthermore, a modeling study based on the application of empirical mixing laws was conducted to identify the most suitable law for accurately representing the experimental results.

3.3.1 Raw Results Obtained by TDS

Techniques that combine time-domain signal analysis with appropriate frequency-domain processing (Fourier analysis) are frequently used due to their ease of implementation and the advantages they offer the user by adding the benefits of time-domain reflectometry to those provided by frequency-domain processing. They are grouped under the name "Time Domain Spectroscopy" or TDS [78-80]. The process involves two steps:

- Measurement (time domain): the first step is performed using time-domain reflectometry (TDR) .
- Second step (frequency analysis): the data from the previous step; which are time-domain in nature; are processed using appropriate mathematical tools to transform them into the frequency domain and then extract the desired parameters [81].

Characterization using the RDT measurement bench yields two time-domain curves: one for a short circuit and one for the sample being characterized. Figures 3.4 and 3.5 show some raw results from measurements performed using this technique.

By observing Figures 3.5 and 3.6, we can directly deduce the nature of the samples, which are dielectrics, since the recorded RDT response is characteristic of a dielectric material. We note that the minimum value of the sample's TDR curve changes depending on the concentrations of the different phases in the mixture [65]. The dashed curve, corresponding to the TDR response to a short circuit, exhibits some slight undulations, which are generally due either to static charges on the short circuit placed at the end of the measurement cell or to poor contact between the different recordings.

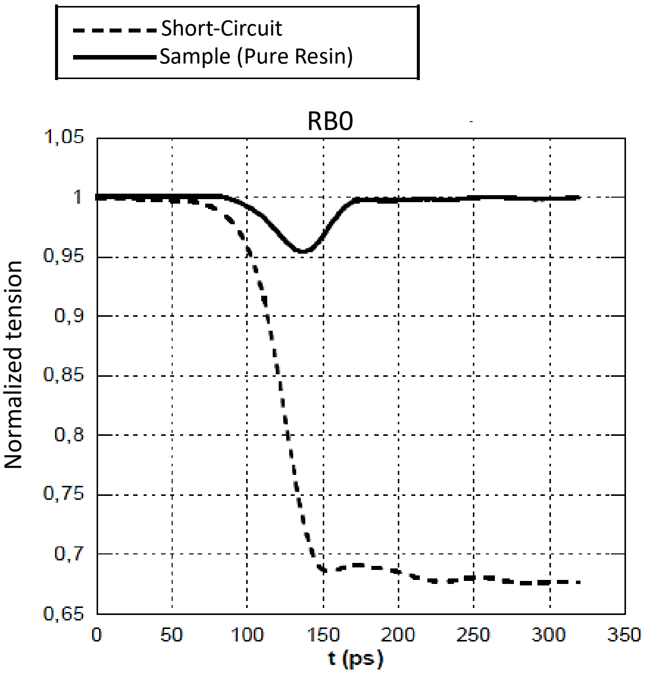

Figure 3.5: TDR response of pure epoxy resin (100%), with an observation window T=320ps

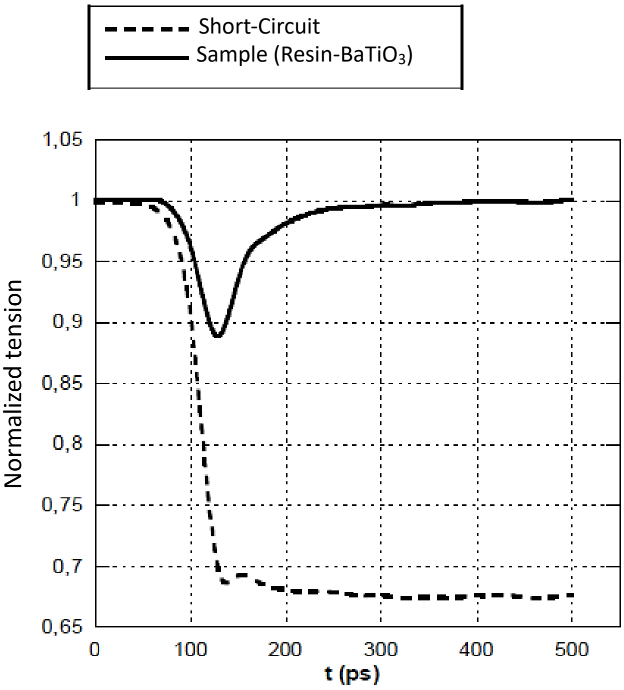

Figure 3.6: Response by TDR of the binary composite (RE-TBa) at (70%, 30%), with an observation window T=500ps.

3.3.2 Comparison of dielectric properties determined by the two measurement benches

3.3.2.1 Dielectric Constant

The analysis of the complex dielectric permittivity of RE–$BaTiO_3$ composites, presented in Figures 3.7and 3.8, highlights the influence of the barium titanate volume fraction on the electromagnetic behavior of the system, for both experimental methodologies used (TDS and MTB).

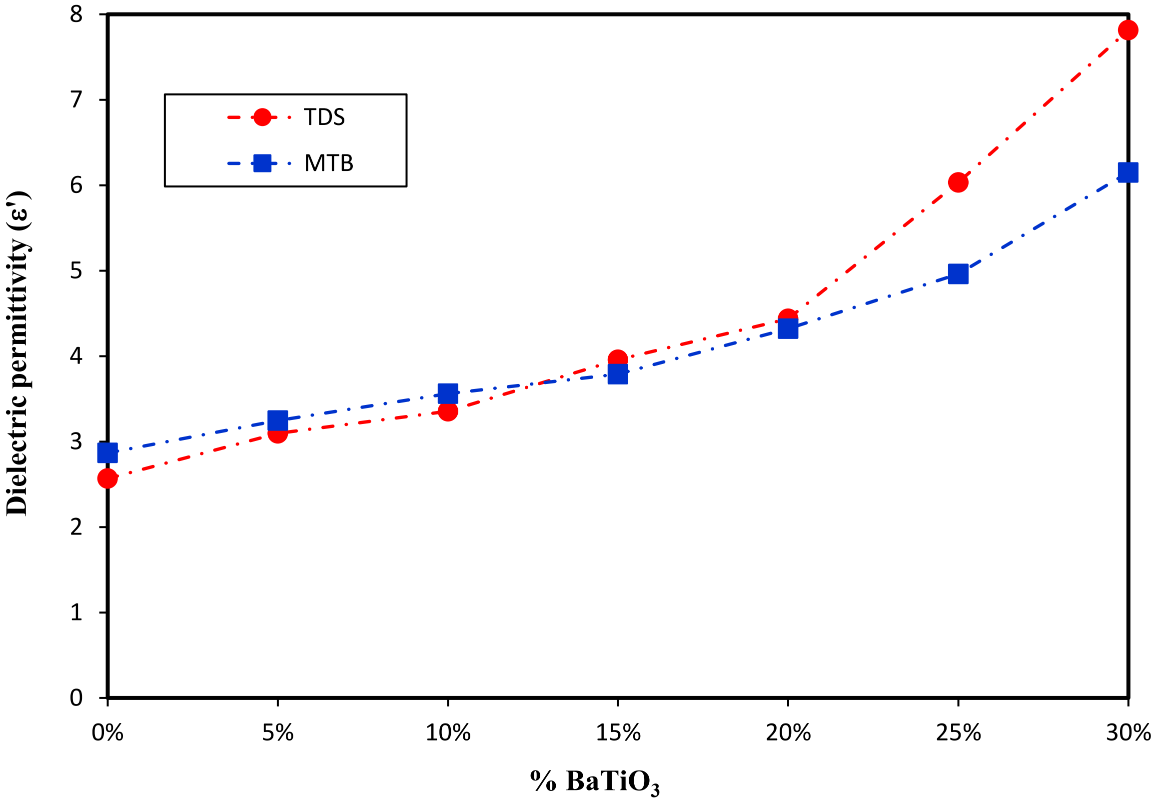

Figure 3.7: Variation of dielectric permittivity for RE-TBA composite as function of TBA concentration for the two measurements benches (TDS and MTB).

Figure 3.7 shows that the real permittivity increases monotonically with the $BaTiO_3$ conentration [82-86]. This trend reflects the effect of the high polarizability of barium titanate, a well-established phenomenon in perovskite-structured polymer-ceramic composites based on titanates. For all the compositions studied, both measurement techniques reproduce the same general trend, confirming the robustness of the observation.

However, a systematic divergence appears between the absolute values obtained by TDS and those from the microwave bench. The MTB measurements generally show slightly higher permittivities for the same volume fraction. This difference can be explained by several factors:

- the difference in the frequency regimes explored.

- the distinct wave-material coupling methods.
- and, the significant difference in the dimensions of the samples used.

In particular, the large sample used on the MTB bench promotes a more homogeneous distribution of the ceramic charge, whereas the TDS sample, three times smaller, induces local densification of the filler, which can alter the polarization trajectories. The extreme values observed range from a minimum permittivity of approximately 2.6 for the pure matrix to a maximum close to 7.8 for a 30% $BaTiO_3$ volume fraction, obtained with the TDS technique.

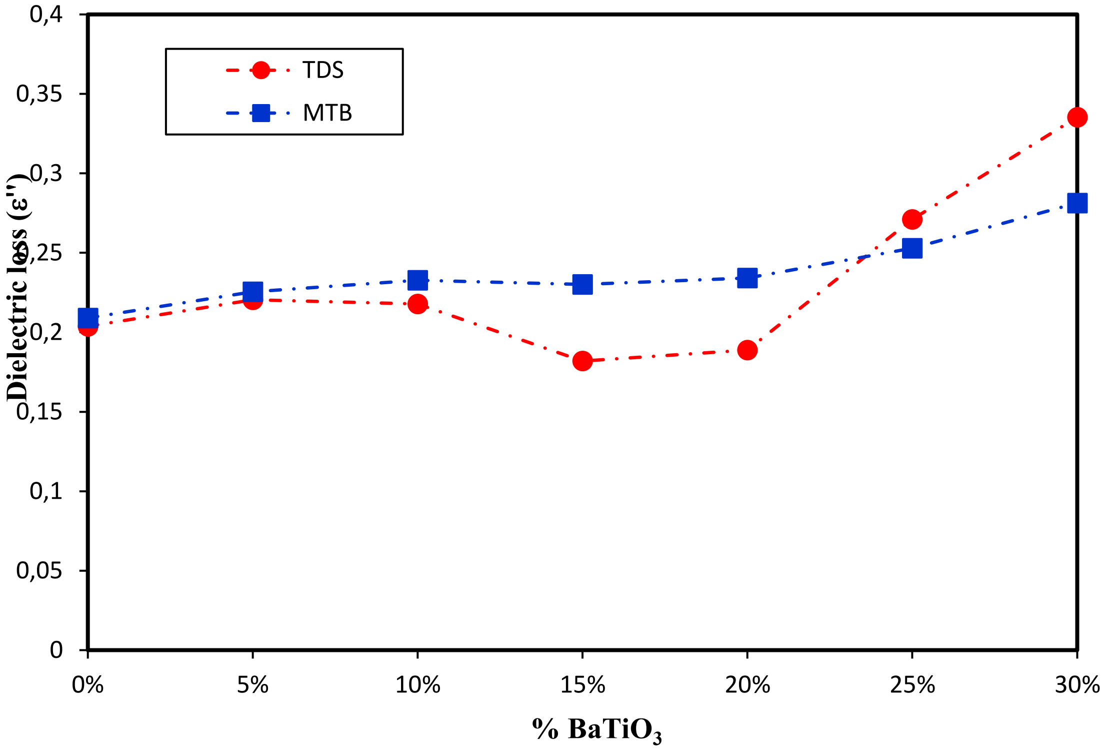

Figure 3.8: Variation of dielectric losses for RE-TBA composite as function of TBA concentration for the two measurements benches (TDS and MTB).

The dielectric losses, illustrated in Figure 3.8, also show an increasing dependence on the $BaTiO_3$ content. Both measurement benches reveal a moderate but steady increase in losses as the volume fraction of the ceramic charge increases. Nevertheless, the dispersion of values differs between the two techniques.

The microwave results show a smooth and relatively stable evolution within the considered loss range (approximately 0.21 to 0.28). In contrast, the TDS measurements show more pronounced fluctuations, reflecting a more complex material behavior when probed over a broad spectral band. These variations may be associated with the emergence of dipolar relaxation phenomena or dispersive effects specific to composites, which the microwave technique, limited to a fixed frequency, cannot necessarily reveal.

3.3.2.2 Electrical Modulus

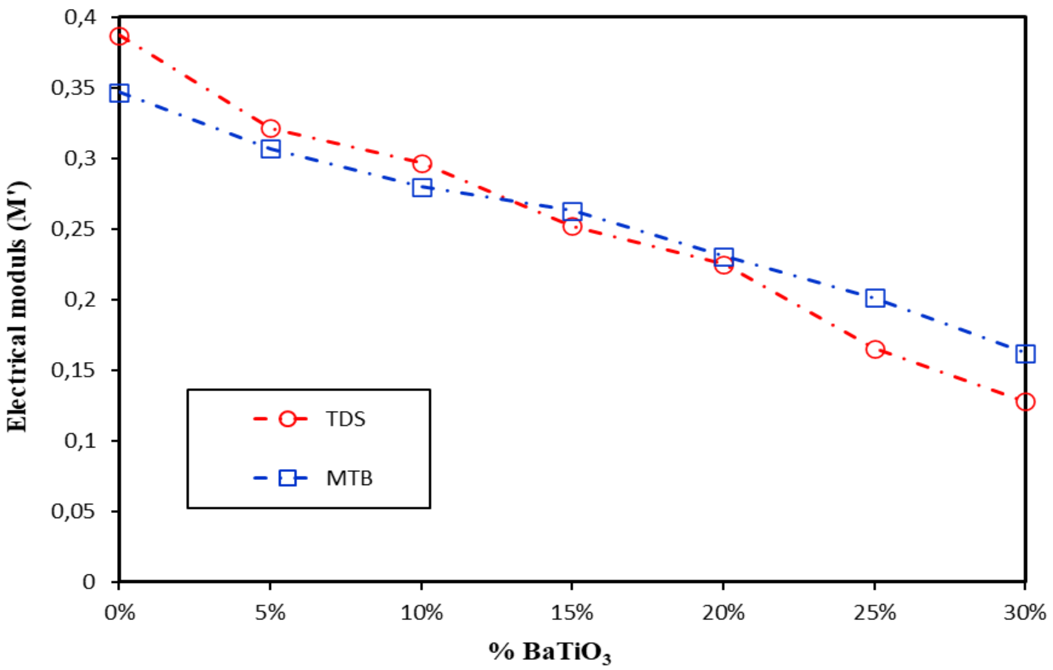

(a)

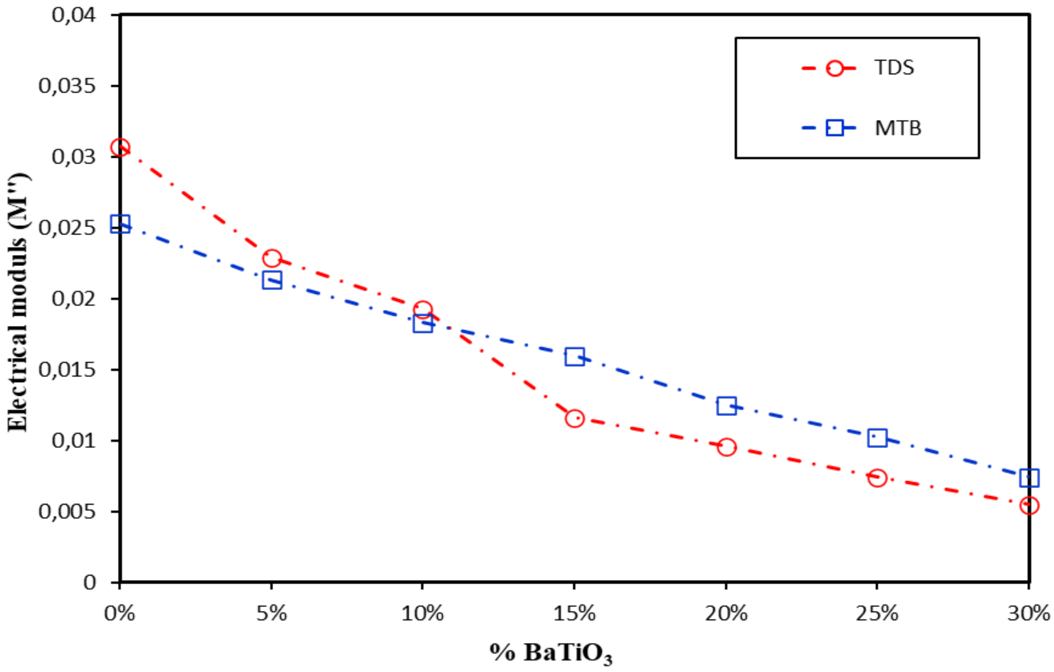

(b)

Figure 3.9: Variation of electrical modulus for RE-TBA as function of TBA concentration for the two measurements benches (TDS and MTB).

Figure 3.9 shows the evolution of the electrical modulus, including its real and imaginary components, as a function of the $BaTiO_3$ concentration in the RE-$BaTiO_3$ composite, as measured by two characterization techniques: TDS and MTB. The results show that the real and imaginary components of the electrical modulus decrease progressively as the volume fraction of $BaTiO_3$ increases. For the pure matrix composite (0% $BaTiO_3$), the maximum values obtained are approximately 0.34 and 0.025 for the real and imaginary parts, respectively, according to the MTB method, and between 0.38 and 0.03 according to the TDS analysis. These observations confirm that the addition of $BaTiO_3$ significantly influences the electrical behavior of the composite, leading to a reduction in the components of the electrical modulus with increasing concentration.

3.3.2.3 Electrical Conductivity

Figure 3.10 shows the evolution of the electrical conductivity of the RE-$BaTiO_3$ composite as a function of the $BaTiO_3$ volume fraction, measured by TDS and MTB. The TDS results indicate a significant decrease in conductivity at high concentrations, while MTB reveals a slight, relatively constant increase, ranging from 5.81×10^{-3} to 7.82×10^{-3} $(\Omega \cdot m)^{-1}$. This difference is related to the wider frequency range used by TDS, allowing for better characterization. Between 0 and 20% $BaTiO_3$, the conductivity stabilizes, suggesting the onset of quasi-percolation, where the particles begin to form conductive pathways. This behavior depends on the size, shape, and distribution of the particles within the composite.

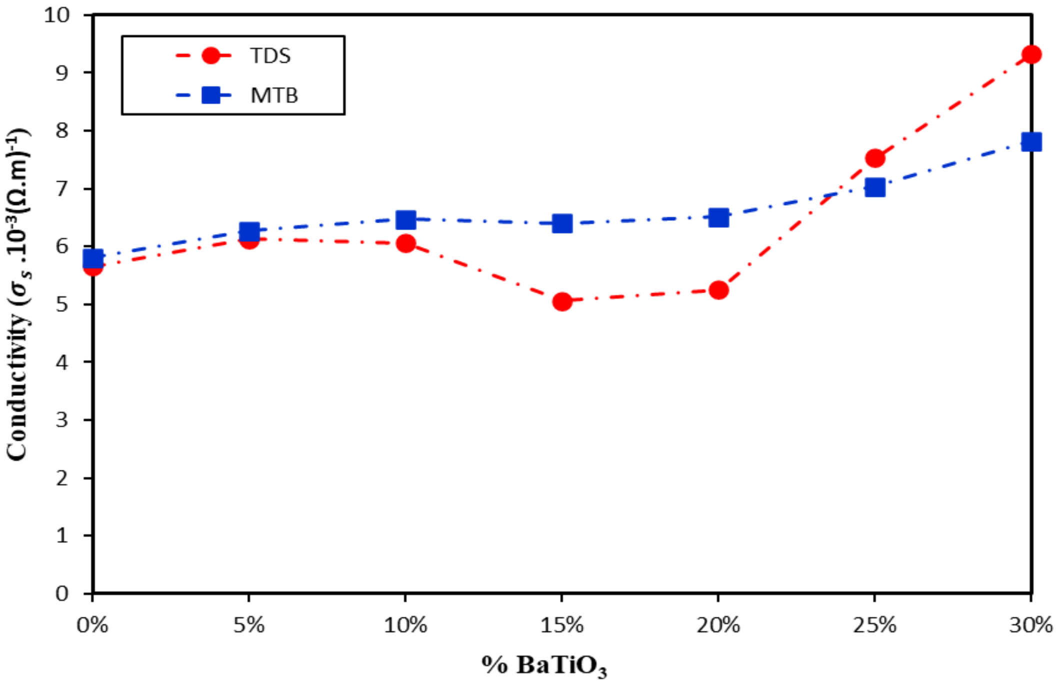

Figure 3.10: Variation of electrical conductivity for RE-TBA as function of TBA for two benches.

3.3.2.4 Dissipation & Quality Factors

Figures 3.11 and 3.12 show the effect of the $BaTiO_3$ volume fraction on the dissipation factor (tanδ) and the quality factor (Q) of RE-$BaTiO_3$ composites, measured by TDS and MTB.

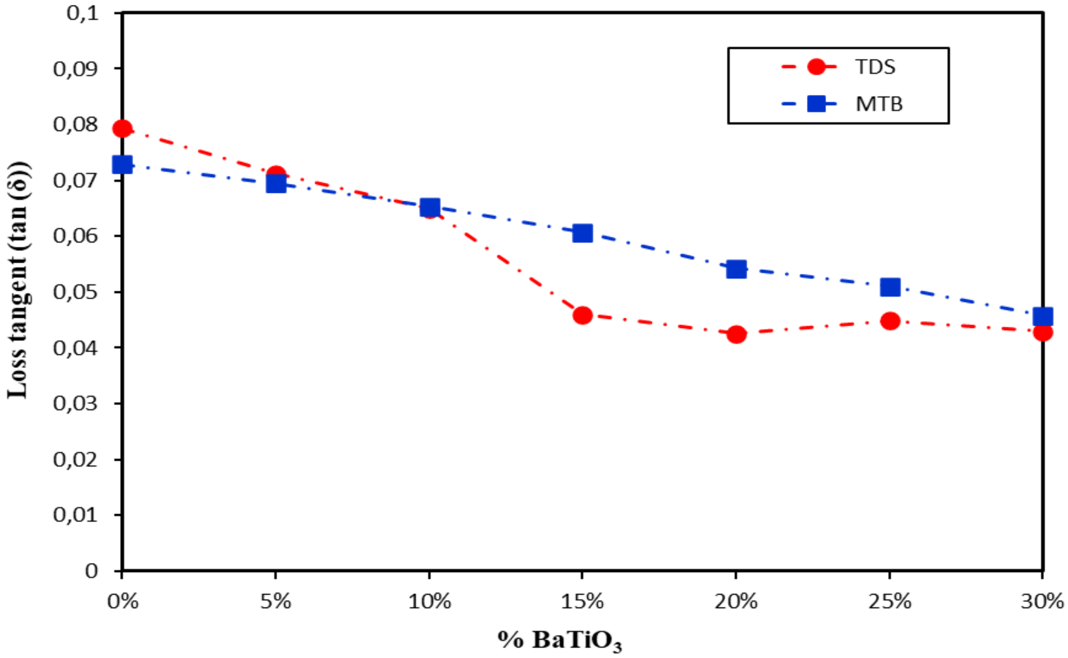

Figure 3.11: Variation of dissipation factor for RE-TBA as function of TBA for the two benches.

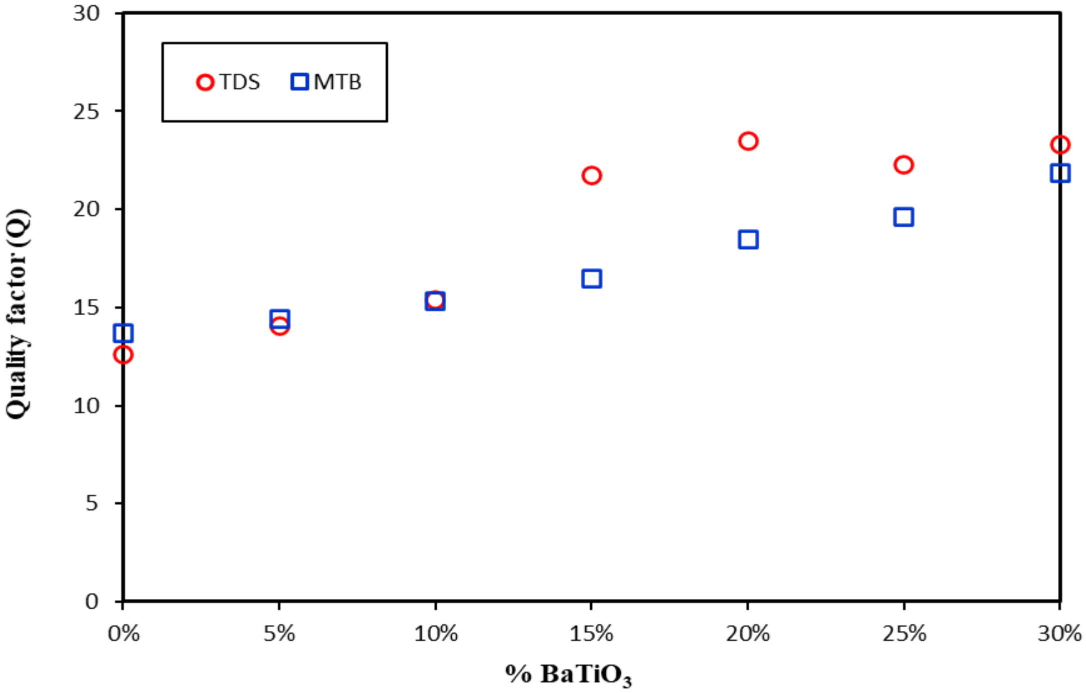

Figure 3.12: Variation of quality factor for RE-TBA as function of TBA for the two benches.

The dissipation factor decreases overall with increasing $BaTiO_3$, from 0.072 to 0.045 for MTB and from 0.079 to 0.042 for TDS, reflecting a reduction in energy losses. This decrease is more pronounced for intermediate $BaTiO_3$ fractions (10–20%), while it remains almost constant for higher (20–30%) or low (0–10%) concentrations. Concurrently, the quality factor increases, from 13.72 to 21.85 for MTB and from 12.60 to 23.48 for TDS, indicating maximum energy storage and minimum dissipation.

The higher values obtained by TDS, covering a wide frequency range (DC–9.490 GHz), compared to those of the microwave bench (9.490 GHz), highlight the influence of the frequency range on tanδ. These results confirm that the addition of $BaTiO_3$ significantly improves the dielectric properties of the composite, reducing losses while increasing the quality factor, which is essential for electronic applications.

3.3.3 Modeling Using Mixture Laws

Figure 3.13 shows the evolution of the effective dielectric permittivity of RE-$BaTiO_3$ composites as a function of the $BaTiO_3$ volume fraction, compared with several predictive models. Experimental measurements show a progressive increase in permittivity with the addition of barium titanate, a trend generally consistent with the theoretical models considered. Beyond 20% filler, the effective permittivity increases further, particularly for the values obtained by the TDS method, which remain consistently higher than those obtained by the MTB method.

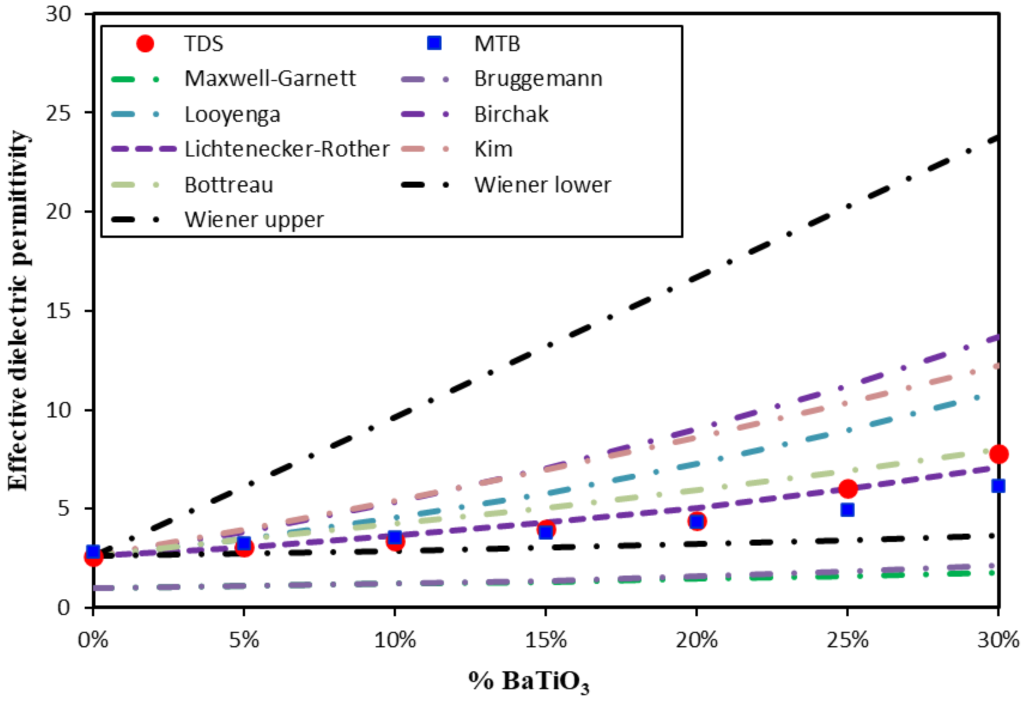

Figure 3.13: Experimental results Vs mixing laws.

The comparative analysis highlights that the Maxwell-Garnett and Bruggeman models deviate significantly from the experimental results as the filler concentration increases, with these predictions falling outside the Wiener domain. In contrast, the Looyenga, Kim, and Birchak models offer a better approximation, although their ability to reproduce the composite's behavior remains limited by interface effects present in the material studied. The Bottreau and Lichtenecker-Rother models, characterized by a quasi-linear evolution of permittivity as a function of concentration, partially overlap and show the best overall agreement with experimental measurements.

The following equation was used to determine the mean squared error Δε, used as an indicator of the difference between experimental values and those predicted by empirical models. In this expression, Δε denotes the mean squared error, while εexp and εmodel correspond respectively to the experimentally measured and theoretically calculated permittivities.

$$\Delta\varepsilon = \frac{1}{N}\sqrt{\sum_{i=0}^{N}\left[\frac{\left|\varepsilon^{i}_{\exp}(i) - \varepsilon^{i}_{\mathrm{mod}\,el}(i)\right|}{\max\left|\varepsilon^{i}_{\mathrm{mod}\,el}(i)\right|}\right]^{2}} \tag{3.4}$$

Table 3.2 presents the square root of the mean squared error Δε obtained for the two characterization methods, TDS and MTB, applied to the RE-BaTiO$_3$ binary composite. The results indicate that the Lichtenecker-Rother model offers the best agreement with experimental measurements, as evidenced by the low values of Δε, equal to 0.058 for TDS and 0.11 for MTB.

Table 3.2: Values of $\Delta\varepsilon$ obtained for the different mixing laws.

	$\Delta\varepsilon$	
Mixing laws models	MTB	TDS
Wiener lower	0.3206	0.4123
Wiener upper	0.5938	0.5672
Maxwell-Garnett	2.0214	2.1933
Bruggeman	1.8224	1.9577
Looyenga	0.2888	0.2432
Birchak	0.3828	0.3447
Lichtenecker-Rother	0.1065	0.0584
Bottreau	0.1959	0.1368
Kim	0.3708	0.3292

3.4 RE-CT-FE Ternary Composite

This section focuses on the study and modeling of the dielectric behavior of a ternary composite made of epoxy resin, calcium titanates, and manganese-zinc ferrite. The TDS characterization of this composite was performed during my internship at the Física Aplicada Laboratory of the University of Zaragoza, Spain. This work is currently being written; therefore, only the raw results are presented.

3.4.1 Study of Dielectric Constant From DC to 5 GHz

Figure 3.14 shows the variation of the real permittivity ε' of the RE–TC–FE ternary composite as a function of frequency, from the DC regime up to 5 GHz. It can be observed that increasing the TC volume fraction leads to a progressive increase in permittivity. This is close to ≈ 4.5 for a volume fraction of 0%, and reaches approximately ≈ 11.5 when the concentration reaches 30%.

Furthermore, for each concentration studied, the permittivity remains almost stable across the entire frequency range [87]. The nearly horizontal curves indicate that, at a constant volume fraction, the permittivity does not depend significantly on the frequency. The slight variations observed can be attributed to experimental uncertainties. This behavior, characterized by a nearly constant permittivity, is consistent with what has been reported in previous studies on ternary composites.

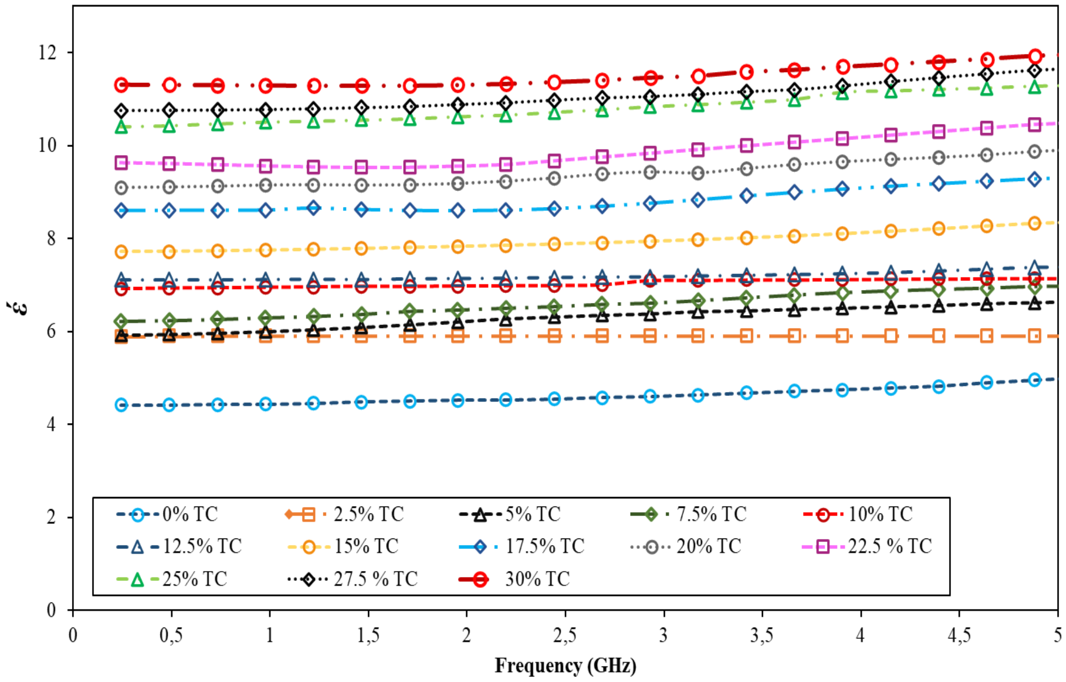

Figure 3.14: Variation of real permittivity of RE-TC-FE as function of frequency.

Figure 3.15 illustrates the evolution of the imaginary permittivity ε'' of the ternary composite of RE-TC-FE as a function of frequency, from the DC regime up to 5 GHz. The imaginary permittivity remains very low, with values close to zero across the entire frequency range. However, a slight increase is observed as the frequency increases. This behavior has already been reported in previous work on ternary composites exhibiting low dielectric losses.

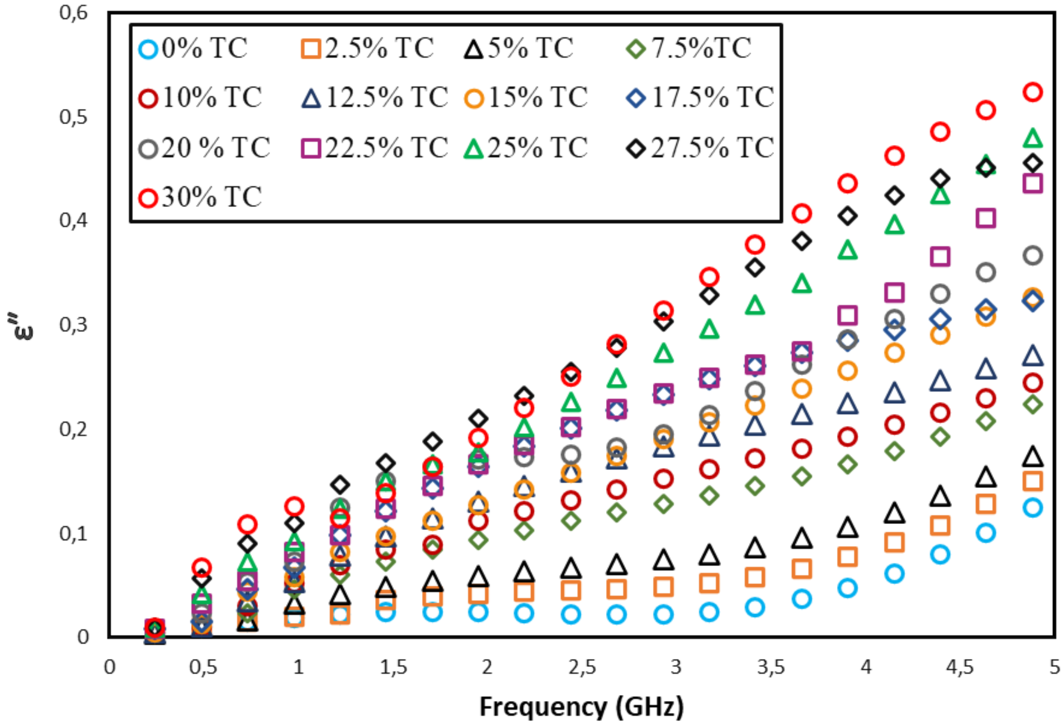

Figure 3.15: evolution of the imaginary permittivity ε'' of the ternary composite (RE-TC-FE) as a function of frequency.

3.4.2 Study of Static Permittivity at low Frequency of 500MHz

Figure3.16 shows the evolution of the static permittivity, measured at 500 MHz, of the ternary composite of RE-TC-FE, as a function of the $CaTiO_3$ volume fraction. A nearly linear increase in permittivity is observed as the $CaTiO_3$ concentration increases. For reference, the permittivity is approximately 4.2 at zero concentration and reaches nearly 11 when the volume fraction reaches 30%.

Furthermore, a decrease in permittivity is observed as the ferrite fraction increases. This can be attributed to the intrinsically lower permittivity of ferrite and the reduction in the polarizable contribution of calcium titanate in the composite. Similar behavior has been reported in several previous studies on ternary composites based on epoxy resin and dielectric oxides.

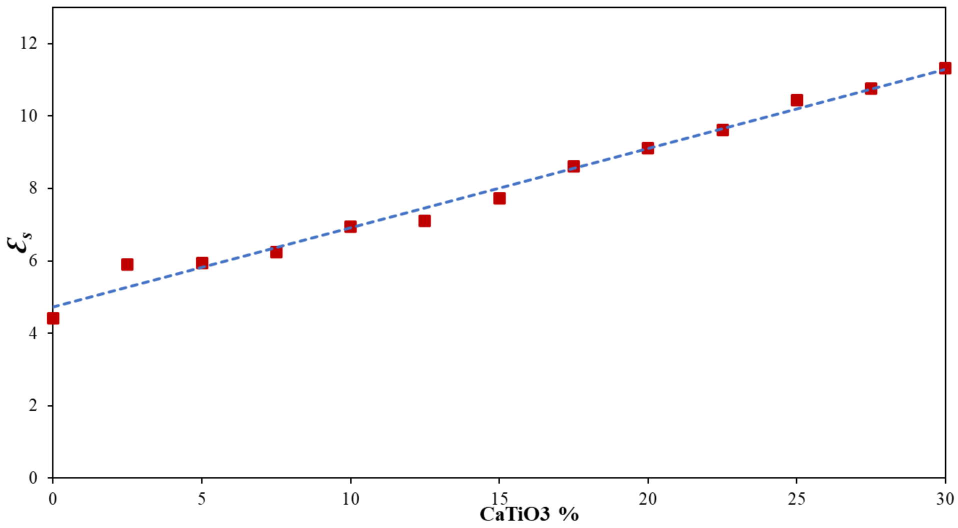

Figure 3.16: Evaluation of static permittivity as the function of CaTiO3 volume fraction.

3.5 Conclusion

This chapter presented a comparative study of two families of composites, analyzing their dielectric behavior from sample preparation to characterization.

The first material examined is a binary RE–$BaTiO_3$ composite. Its dielectric properties were measured at room temperature using two complementary techniques: an X-band microwave bench (9.490 GHz) and time-domain spectroscopy covering the 0–9.490 GHz range. The various dielectric properties were determined as a function of the $BaTiO_3$ volume fraction. The results show that increasing the ceramic charge systematically improves the permittivity, with maximum values of approximately 7.25 (TDS) and 6.15 (MTB), while losses remain moderate and quality factors reach high values, indicating low dissipation. The comparative study of empirical models reveals that those of Lichtenecker and Bottreau most accurately reproduce the effective permittivity.

The second material studied is a ternary RE–CaTiO3– MnZn Fe_2O_4 composite characterized using a TDS bench. The real and imaginary permittivity were measured over a wide frequency range, from DC to 5 GHz. The results show quasi-static behavior, with an imaginary permittivity close to zero. Furthermore, the analysis of the static permittivity at 500 MHz highlights an increase in permittivity as the calcium titanate concentration increases.

Overall, this work provides significant insights into the understanding and modeling of polymer-ceramic composites and constitutes a solid foundation for the development of advanced materials for microwave applications, sensors, resonators, absorbers, and energy harvesting or storage systems.

CHAPTER

4

Characterization and Modeling of Dielectric Composites by Finite Element Method

4.1 Introduction

This chapter presents the numerical modeling of dielectric composite materials using the Finite Element Method (FEM). This chapter focuses on the implementation of FEM to determine the effective permittivity of binary composites composed of an epoxy matrix filled with ceramic particles. The numerical approach is employed to investigate how particle morphology, size distribution, concentration, and intrinsic permittivity influence the macroscopic dielectric response of the composite.

To reproduce realistic heterogeneous microstructures while maintaining computational efficiency, the analysis is carried out in two dimensions. Several statistical distribution models are used to generate random sets of ellipsoidal inclusions, allowing the study of different configurations and their impact on the computed effective permittivity. This procedure enables the systematic evaluation of microstructural effects that are difficult to capture through analytical formulations alone.

A central component of this chapter is the comparison between FEM results and classical analytical mixing laws. These theoretical models, commonly used to estimate the effective dielectric properties of composite media, provide reference values that help assess the validity and limitations of the numerical predictions. By examining the correspondence between the two approaches, the chapter highlights conditions under which analytical laws remain reliable and identifies cases where FEM provides a more accurate description of heterogeneous systems.

The chapter is structured as follows: the modeling framework and boundary conditions are first described; the generation of composite geometries and statistical distributions is then presented; finally, the numerical results are discussed and compared with selected mixing laws. This structure provides a coherent basis for understanding the modeling strategy and for evaluating the performance of FEM in the dielectric characterization of composite materials.

4.2 Simulation methodology

4.2.1 Model structure and computational details

Our work focuses specifically on the study of the effective permittivity of random and lossless dielectric composite materials in the quasi-static state. The quasi-static regime is determined when the temporal variations of the electromagnetic field are negligible compared to the spatial variations. This condition is valid when the wavelength of the incident wave is much larger than the typical size of the inhomogeneities presented in the material.

This study consisted in simulating several samples with different permittivities, sizes, concentration, and distribution of ellipsoidal particles. This was achieved by doing a numerical modeling using COMSOL Multiphysics® [76] software version 5.6 which integrates all the functions of MATLAB software containing the parameters of each particle distributed in the epoxy resin polymer matrix. This software uses the finite element method to develop and solve the quasistatic models. A thorough description of this method is available in the literature [69, 88,89].

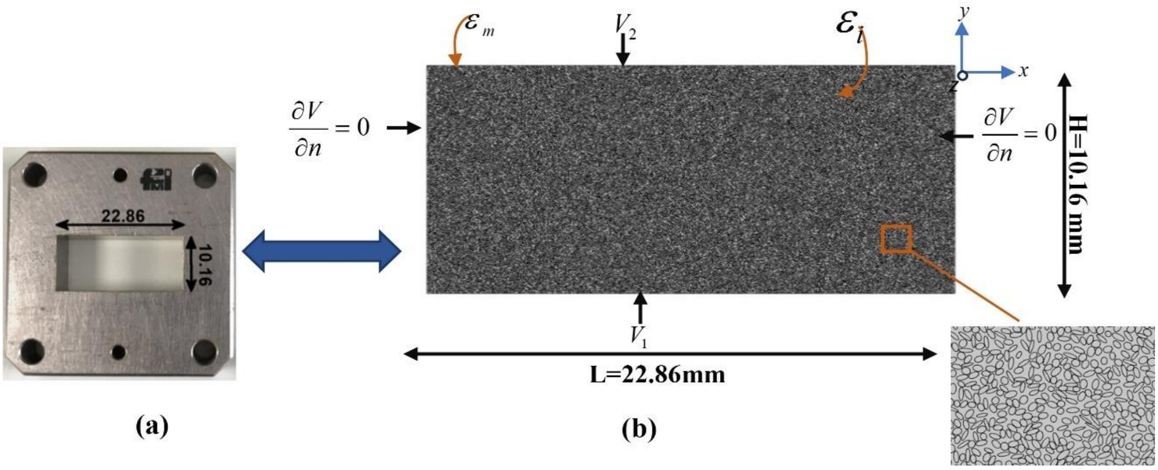

(a) (b)

Figure 4.1: (a) Rectangular waveguide WR-90, (b) Unit cell of the composite material studied and boundary conditions**.**

Figure 4.1 shows the geometry of the unit cell of the composite under study. This cell has dimensions equivalent to those of the rectangular WR-90 waveguide (0.9 in [22.86 mm] x 0.4 in [10.16 mm]). Our two-dimensional structure of the binary composite consists of an epoxy resin host matrix of permittivity $\varepsilon_m = 2$, and ellipsoidal ceramic particles randomly distributed without overlap in the matrix. In order to determine the evolution of the effective permittivity as a function of the surface fraction, the permittivity ε_i , and the particle sizes, the finite element method was used.

Consider the unit cell in Figure 4.1 as a capacitor model. It is composed of two opposite faces with a area A and a height H between them. These faces are subject to a potential difference (V_1-V_2). The periodic boundary conditions $\partial V / \partial n = 0$ are applied to the planes parallel to the direction (Oy). To calculate the effective permittivity, the FEM uses a finely discretized mesh of the spatial domain, where it divides the rectangular geometry into smaller triangular elements (Figure 4. 2).

This meshing strategy facilitates the precise calculation of the spatial distribution of the potential (Figure 4.3) inside this geometry, which is devoid of free charges or currents, via the resolution of Laplace's equation:

$$\vec{\nabla}\cdot(\varepsilon_0\varepsilon(r)\vec{\nabla}V)=0 \tag{4.1}$$

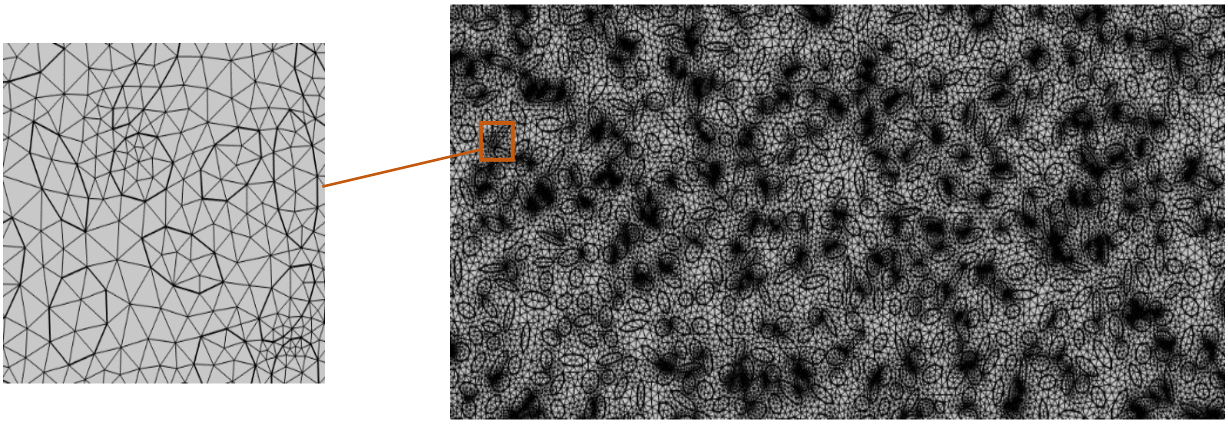

Figure 4.2. Mesh Representation of the unit cell

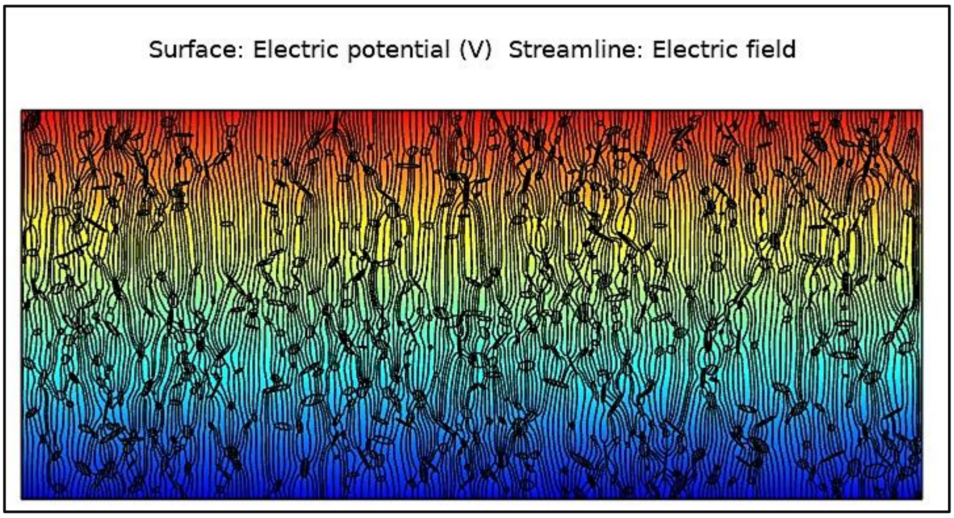

Figure 4.3: Spatial distribution of electric potential and electric field.

With $\varepsilon(r)$ and V representing respectively the local relative permittivity and the spatial distribution of the potential in the cell, where the free charge density is zero, and $\varepsilon_0 = 8.85\times10^{-12}\left[F/m\right]$ as the permittivity of vacuum, the electrostatic energy W can be expressed in terms of the partial derivatives of V over the entire surface of the unit cell.

$$W = \frac{1}{2}\varepsilon_0 \int\int_s \varepsilon(x,y)\left[(\frac{\partial V}{\partial x})^2 + (\frac{\partial V}{\partial y})^2\right]dxdy \tag{4.2}$$

By imposing periodic boundary conditions $\partial V/\partial n = 0$ on the planes parallel to the direction (Oy). the effective permittivity is obtained by evaluating the energy stored in the capacitor:

$$W = \frac{1}{2}\varepsilon_0\varepsilon_{eff}\frac{A}{H}(V_1 - V_2)^2 \tag{4.3}$$

4.2.2 Calculation algorithm

To determine the parameters of the ellipses, we created a MATLAB code that integrates a computational algorithm. The main objective of the algorithm is to generate a non-overlap random distribution of ceramic particles in the epoxy resin matrix. To achieve this, the algorithm follows two main procedures: particle surface area distribution and particle location determination. Here we present the outline of the developed generation algorithm.

a. The algorithm takes several input parameters, including the total particle surface fraction, mean value of particles surface area (μ), standard deviation of particles (σ), minimum particle ratio (r_{min}), maximum particle ratio (r_{max}), minimum (x_{min}) and maximum (x_{max}) grand axis of particles.

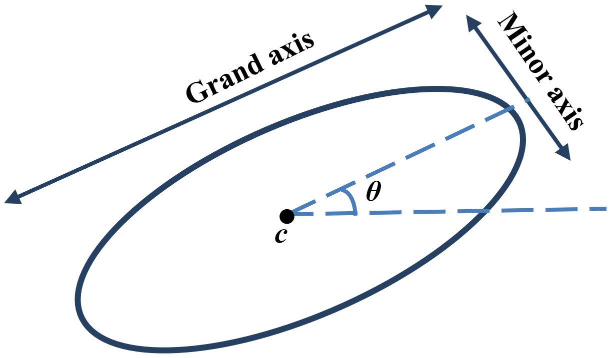

Figure 4.4: Illustration of the shape characteristics of an ellipse. The aspect ratio was calculated by dividing the grand axis by the minor axis.

b. **Particle surface area distribution procedure**:

The particle size distribution procedure begins by generating particles one by one. Each particle is assigned a random ratio (r) within the specified range (r_{min} to r_{max}). This randomness influences the distribution of particle sizes within the polymer matrix.

c. **Particle location determination procedure:**

The procedure focuses on assigning positions to the generated particles within the polymer matrix. It calculates the x parameter, which characterizes particle location (c), based on the particle ratio and random values. The calculated (x) value must fall within the range defined by (x_{min}) and (x_{max}).

d. **Intersection avoidance**:

To ensure that the particles do not overlap, the algorithm checks whether the sum of the radii of the two ellipses is less than the distance between their centers (Figure 4.5). Mathematically this can be expressed by the equation 4. This check consists of solving a system of mathematical equations presented in [90]. If an intersection is detected, indicating particle overlap, the algorithm iteratively repositions the particles until no intersection occurs. The maximum number of iterations ($iter_{max}$) prevents the algorithm from getting stuck in infinite loops.

$$\sqrt{(x_2 - x_1)^2 + (y_2 - y_1)^2} \geq a_1 + a_2 \tag{4}$$

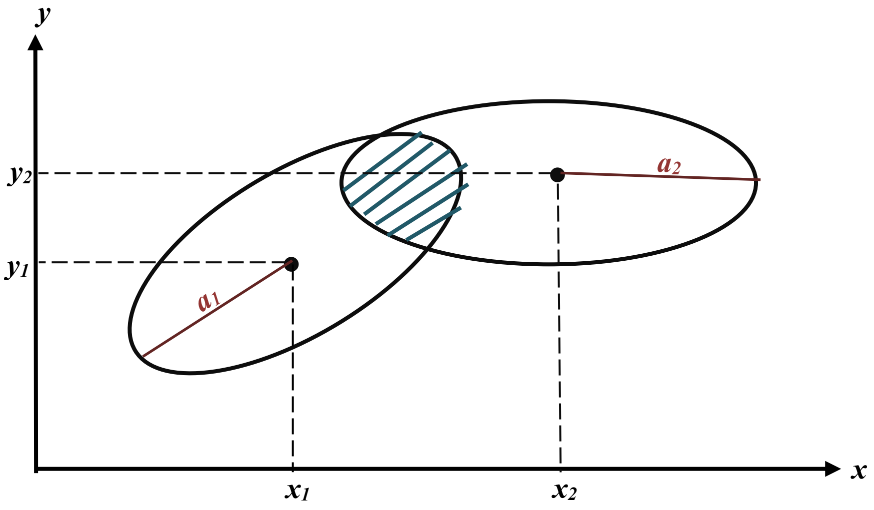

Figure 4.5: Illustration of two ellipses overlap.

e. **Surface fraction calculation:**
   The algorithm calculates the surface fraction of the particles within the polymer matrix. This calculation is based on the areas of the ellipses and their corresponding particle ratios.
f. The particle generation and location determination steps continue until a specific condition is met, such as generating a desired number of particles or reaching a maximum iteration limit.
g. The resulting particle locations (*c*), grand axes (*gx*), small axes (*sx*), and surface fraction (*S*) are obtained as output.

To integrate the parameters of the ellipses obtained in the unit cell, we establish a connection between the MATLAB software and COMSOL using LiveLink [91]. This integration allows us to use the Finite element method available in COMSOL to extract the effective permittivity of the composite samples. It is noteworthy that this simulation may be time-consuming, particularly for distributions with a high concentration of particles.

4.3 Results and discussion

Dielectric composites, which generally combine ceramic particles with a polymer matrix, offer a remarkable synergy between the properties of the two materials: the flexibility and lightness of the polymer, combined with the high permittivity and low dielectric losses of ceramics. However, the performance of these composites is not limited to the dielectric constant of the ceramic particles. Aspects such as the shape, size and distribution of particles in the polymer matrix, as well as their volume fraction, also play a significant role in the overall performance of the material. In this section, we explore the impact of these parameters on the overall permittivity through detailed simulations, allowing an in-depth analysis of the influence of microstructure on dielectric properties. Furthermore, we examine how mixing laws can be used to model the dielectric constant, highlighting the relevance and accuracy of these approaches in predicting the electromagnetic behavior of composites. By integrating these two aspects, our study provides essential insights for the design and optimization of advanced dielectric composites, paving the way for further advancements in various fields of electronics and telecommunications.

4.3.1 Dielectric constant sweep

In our study, we employed epoxy resin with a constant permittivity of (ε_m= 2) as a matrix to bind the charged ceramic particles. We analyzed the dielectric permittivity of three epoxy resin/ceramic

(RC) composites with ceramic permittivities (ε_i) of 80, 400, and 3600, respectively. For each composite, we performed simulations on several samples, varying the surface fraction (S) of ellipsoidal particles included in the matrix from 0.05 (5%) to about 0.4 (40%). Each composite was modeled according to three random distributions of ceramic particles: normal (N), log-normal (LN), and Rayleigh (R). For each distribution, we examined three cases of different particle sizes. This approach allowed us to study the impact of the permittivity of the ceramic particles, their concentration, their size and their distribution on the overall permittivity of the composite.

4.3.1.1 Normal distribution (N)

The normal distribution (N), also called the Gaussian distribution, is widely used to model various physical systems due to its ease of use and flexibility. In our case study, we apply this distribution to the surface area of ellipsoid-shaped particles present in an epoxy polymer matrix. This approach allows us to statistically characterize the distribution of areas within the matrix, which results in a distinctive bell-shaped curve in our curves (Figures. 4.6.a, 4.7.a and 4.8.a).

Table 4.1 lists the designation and composition of 3 sets of simulated RC samples. each series represents a distinct case of particle sizes that follow the normal distribution N-(RC), which is defined by the mean area μ and the standard deviation σ values.

Table 4.1. Characteristics of Three Series of RC Composites Simulated Using the Normal Distribution (N).

	N-(RC)$_1$		N-(RC)$_2$		N-(RC)$_3$	
	μ=0.1 mm^2 , σ=0.005 mm^2		μ=0.02 mm^2, σ=0.001 mm^2		μ=0.005 mm^2, σ= 0.001 mm^2	
N° Samples	***N^0 particles***	***S***	***N^0 particles***	***S***	***N^0 particles***	***S***
1	250	0.059	600	0.052	2600	0.052
2	300	0.109	1000	0.087	4400	0.087
3	350	0.131	1400	0.112	6200	0.122
4	400	0.163	1800	0.147	7995	0.157
5	450	0.194	2200	0.172	9795	0.192
6	500	0.226	2600	0.207	11589	0.227
7	550	0.259	3000	0.232	13361	0.262
8	600	0.281	3400	0.267	15154	0.297
9	650	0.311	3800	0.292	16841	0.332
10	700	0.344	4200	0.327	18528	0.367
11	750	0.375	4600	0.357	20215	0.392
12	800	0.399	5000	0.395		

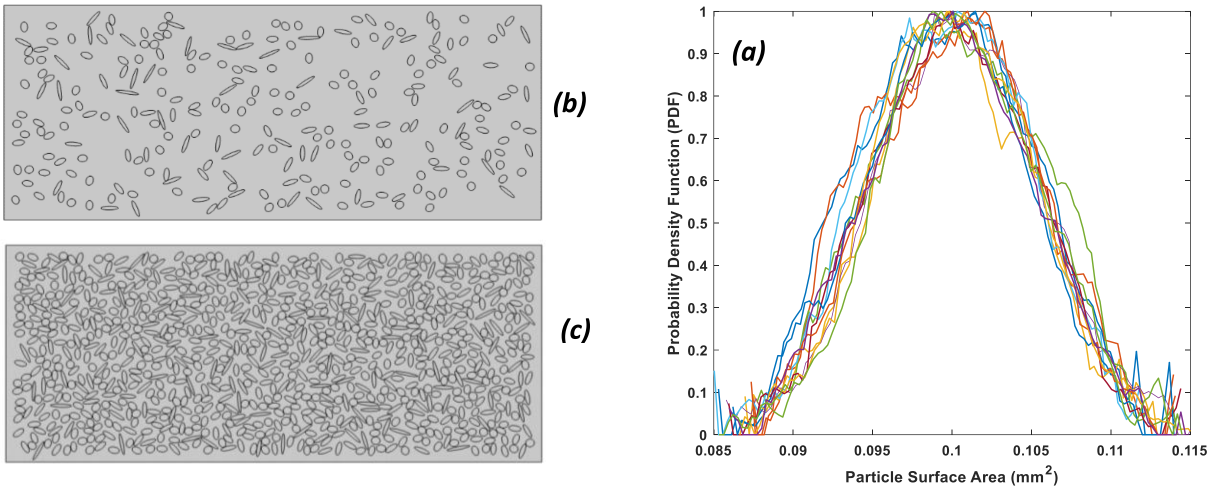

Figure 4.6: N-(RC)$_1$**:** **(a)** Normal distribution of all samples, **(b)** Sample Nº 1 (S=0.059), **(c)** Sample Nº 12 (S=0.399).

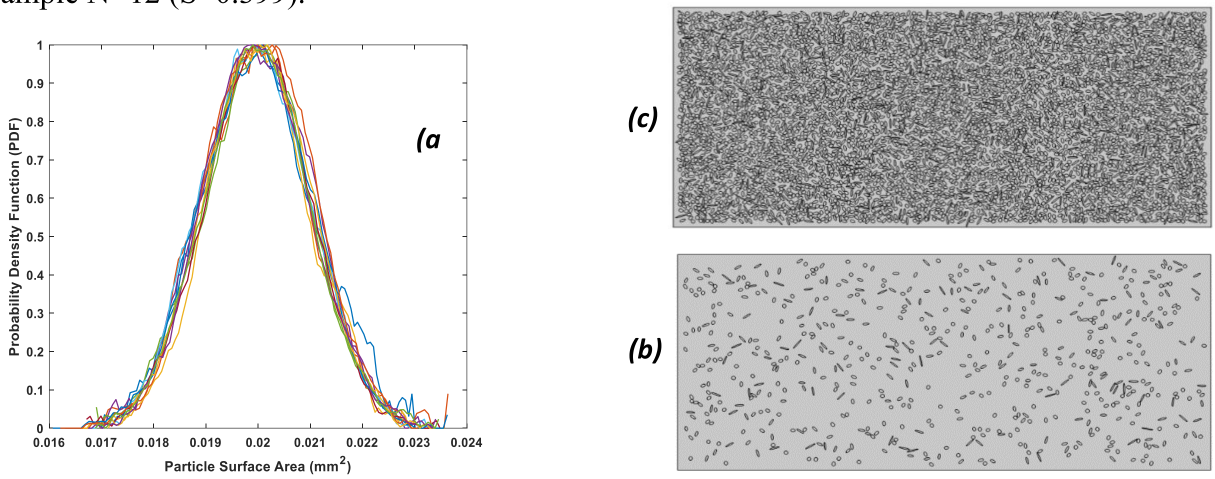

Figure 4.7: N-(RC)$_2$: **(a)** Normal distribution of the samples, **(b)** Sample Nº 1 (S=0.052), **(c)** Sample Nº 12 (S=0.395).

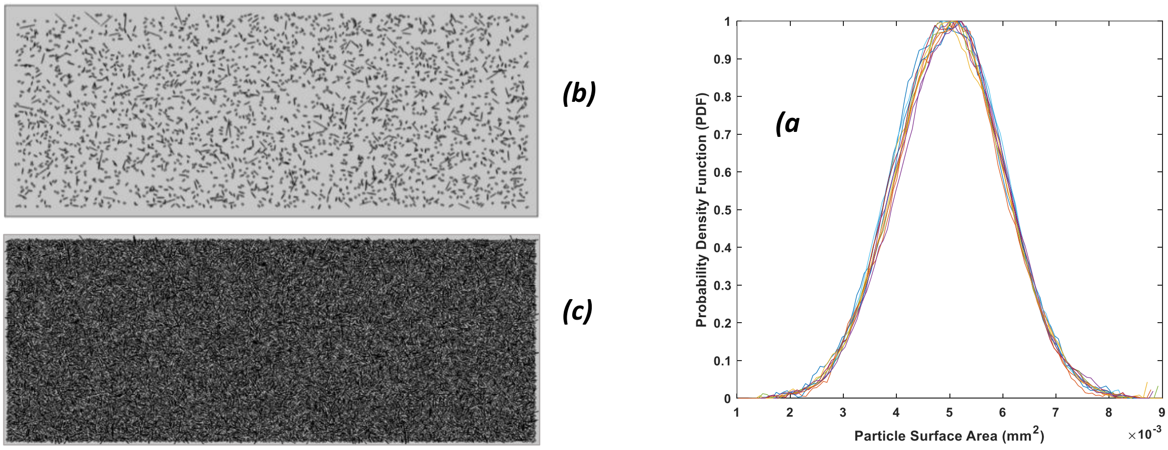

Figure 4.8: N-(RC)$_3$: **(a)** Normal distribution of the samples, **(b)** Sample Nº 1(S=0.052), **(c)** Sample Nº 11 (S=0.392).

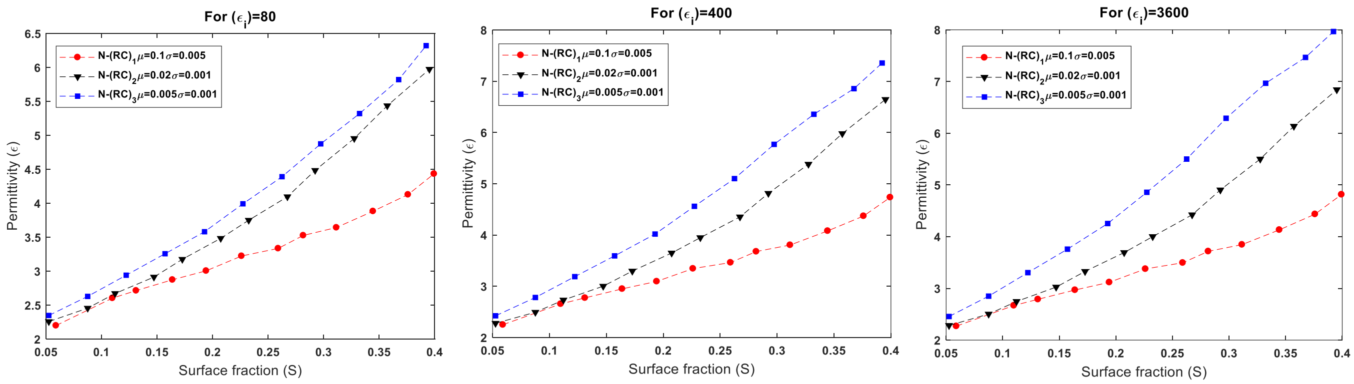

Figure 4.9: Evolution of the effective permittivity as a function of surface fraction for N-(RC) composites.

Figure 4.6.a shows the normal distribution of the simulated samples for case N-(RC)$_1$, giving us an idea of how the particle sizes are spread out. The average particle size is 0.1 mm², with a small standard deviation of 0.005 mm², meaning most of the particles are quite similar in size.

Figures 4.6.b and 6.c present 2D COMSOL simulations of two different samples, helping to visualize how the particles are distributed in the material. Figure 4.6.b represents the first sample, where the particle surface fraction (S) is 0.05, so the particles are more spaced out. On the other hand, Figure 4.6.c corresponds to the last sample, with S = 0.39, where the particles are much denser. Even though this sample has a higher fraction of particles, their relatively large size means there aren’t that many overall, with only 800 particles.

Figure 4.7 illustrates the distribution of N-(RC)$_2$ and presents 2D models of the first and last samples. A key difference compared to N-(RC)$_1$ is the smaller particle size of 0.02 mm², which significantly impacts the overall microstructure. Since the particles are much smaller, there is a higher number of ellipsoidal inclusions in the composite, as clearly depicted in Figures 4.7.b and 4.7.c.

For instance, when considering the last sample from Table 1 with S = 0.39, we observe a remarkable increase in particle density, with approximately 5,000 particles embedded within the epoxy matrix. This sharp contrast with N-(RC)$_1$ (which had only 800 particles for the same S value) highlights the influence of particle size on dispersion and composite microstructure. The higher number of inclusions suggests a greater interfacial area between the particles and the surrounding matrix, which may lead to enhanced dielectric and mechanical properties, depending on particle-matrix interactions.

For the N-$(RC)_3$ case, interesting illustrations have been shown in Figure 4.8. It is notable that the distribution of particles in this case has a lower mean (μ=0.005 mm^2) with a large standard deviation (σ=0.001mm^2), which results in a large number particles of various sizes. For the same case where S=0.39, there are 20215 inclusions.

Figure 4.9 represents the evolution of the effective permittivity depending on the surface fraction of the three series of simulated composite samples (N-$(RC)_1$, N-$(RC)_2$, and N-$(RC)_3$) for three cases of permittivity of ellipsoid particles ε_i= 80, 400 and 3600.

It is observed that the distribution of N-$(RC)_3$ particles gives a better permittivity compared to N-$(RC)_2$ and N-$(RC)_1$ in all cases of particle permittivity. It is likely that this is due to the diversity of particle sizes in this case, where the standard deviation is larger compared to the mean. This size diversity could lead to greater variability in the dielectric properties of the particles, which could help improve the overall permittivity of the composite. In addition, the number of inclusions is also large, which could enhance the interactions between the matrix and the filler. These matrix-filler interactions, resulting from a wider distribution of particles in the matrix, could play a crucial role in improving the dielectric properties of the composite material.

We also notice, for the three cases of permittivity of ceramic particles, When the surface fraction is low ($S < 0.1$), indicating a low concentration of inclusions, minimal fluctuations in the permittivity values are observed, this is due to the minimum interaction between particles within the composite. These charge-matrix interactions become more important as S increases, producing a higher effective permittivity. This increase in dielectric permittivity indicates the same effect of titanates compared to that obtained in previous works [84-87,92, 93].

On the other hand, it is evident that the ceramic charge permittivity has a direct impact on the electromagnetic interactions between the charge and the matrix in the composite material. When the permittivity of the ceramic is very high than the permittivity of the matrix (case of 400 and 3600), this means that the particles interact more strongly with the matrix, which can lead to a greater increase in the effective permittivity of the composite material. Let us take the example of sample N° 12 in Tab .1 for case N-$(RC)_3$: at a surface fraction (S) of 0.39, the effective permittivity of the material varies. For a permittivity (ε_i) of 80, the effective permittivity value is measured at 6.3. This value increases to 7.4 when the permittivity is 400, then reaches 8 for a permittivity of 3600.

4.3.1.2 Log-normal distribution (LN)

A Log-normal distribution is a statistical distribution of logarithmic values derived from an associated normal distribution. The use of this distribution is appropriate for modeling a wide variety of particle sizes due to its skewed nature, characterized by a long tail to the right (see Figures. 4.10.a, 4.11.a, and 4.12.a).

Table 4.2 shows the simulation results obtained by applying log-normal modeling to three distinct series (LN-(RC)$_1$, LN-(RC)$_2$, and LN-(RC)$_3$).

Table 4.2: Characteristics of Three Series of RC Composites Simulated Using the Log-normal Distribution (LN).

	LN-(RC)$_1$		**LN-(RC)$_2$**		**LN-(RC)$_3$**	
	$\mu=0.1$ mm^2 $\sigma=0.15$ mm^2		$\mu=0.03$ mm^2 $\sigma=0.02$ mm^2		$\mu=0.01$ mm^2 $\sigma=0.01$ mm^2	
N° **Samples**	***N^0 particles***	***S***	***N^0 particles***	***S***	***N^0 particles***	***S***
1	144	0.054	348	0.056	996	0.050
2	224	0.091	628	0.093	1688	0.090
3	310	0.132	900	0.133	2363	0.119
4	385	0.163	1450	0.171	3018	0.156
5	445	0.218	1700	0.212	3668	0.194
6	528	0.231	1955	0.239	4306	0.229
7	603	0.255	2440	0.259	4914	0.259
8	644	0.286	2635	0.288	5485	0.297
9	725	0.305	2824	0.306	6036	0.315
10	775	0.322	3150	0.326	6610	0.331
11	812	0.342	3307	0.345	7022	0.348
12	850	0.367	3403	0.365	7447	0.379
13	930	0.386	3518	0.373	7507	0.382
14	997	0.399	3661	0.398	7914	0.394

According to the three series illustrated in Figures 4.10, 4.11 and 4.12. we observe that there is a great variety in the sizes of the particles. This observation can be explained by the nature of this distribution on the one hand with the high value of σ on the other hand.

The particle distribution for the LN-(RC)$_1$ sample series is shown in Figures 4.10.a. A visualization of the particle distribution for sample N° 1 and 14, performed under COMSOL, is shown in Figures 4.10.b and 4.10.c respectively. Significant variability in particle sizes was observed given that standard deviation is large (σ= 0.15 mm^2) with a high mean surface area (μ = 0.1 mm^2). This translates into a relatively low number of inclusions. For example, in the last sample visualized in Figure 4.10.c, for a concentration of S=0.39, only 997 particles are present.

In LN-$(RC)_2$ and LN-$(RC)_3$, on the other hand, the number of particles increases as μ decreases. However, in this distribution, we encountered difficulties in the simulation of inclusions for lower standard deviation (σ) values, in contrast to the case of the normal distribution. The characteristics of this distribution can make the simulation more complex, as the algorithm must guarantee an appropriate distribution of particles in the matrix without overlap, while taking into account the skewed nature and narrow range of the log-normal distribution.

The permittivity values found for the different series of simulated samples as a function of the surface fraction S when ε_i = 80, 400, and 3600, respectively, are shown in Figure 4.13.

The graphs show that permittivity increases with increasing particle surface fraction (S). However, the permittivity (ε) found for the three distribution cases LN-$(RC)_1$, LN-$(RC)_2$, and LN-$(RC)_3$ is relatively close when the permittivity of the ceramic particles is relatively low (ε_i= 80). This behavior can be explained by two points: on the one hand, a ceramic particle permittivity of 80, which is not significantly higher than that of the epoxy matrix (ε_m=2), leads to a weaker polarization effect. On the other hand, particle size has a minimal impact on the overall permittivity of the composite, as they all interact in the same way with the weak polarization effect. In contrast, when the ceramic permittivity is significantly higher (400 and 3600), the inclusions exert a stronger influence on the effective permittivity of the composite. The large contrast between the matrix and particles permittivities leads to a stronger polarization effect, and the size of the particles becomes a more critical factor.

It is remarkable that LN- RC_3 gives a better permittivity than LN-RC_1 and LN-RC_2 for ε_i = 400 and ε_i = 3600, This is attributed to two parameters: a low mean (μ=0.01 mm2) associated with a large standard deviation (σ=0.01), indicating a large number of inclusions with a high variability in particle sizes. This situation can have a significant impact on interfacial polarization, and consequently on the permittivity of the composite. For instance, for ε_i = 3600 and S = 0.39, we find that ε = 6.8 for the LN-RC_2, 7.2 for LN-RC_1, and 8.9 for LN-RC_3

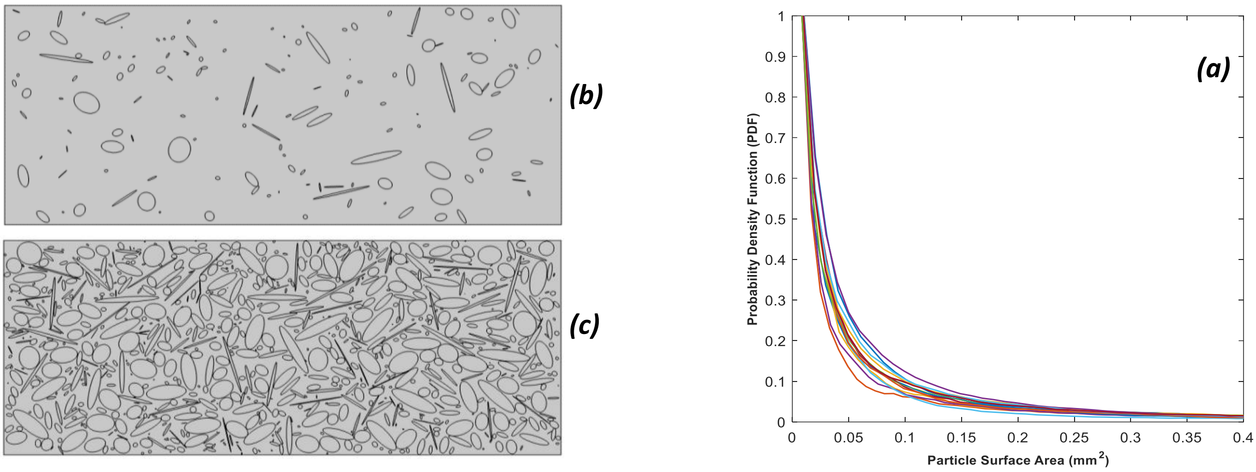

Figure 4.10: LN-(RC)$_1$: **(a)** Log-normal distribution of the samples, **(b)** Sample Nº 1 (S=0.054), **(c)** Sample Nº 14 (S=0.399).

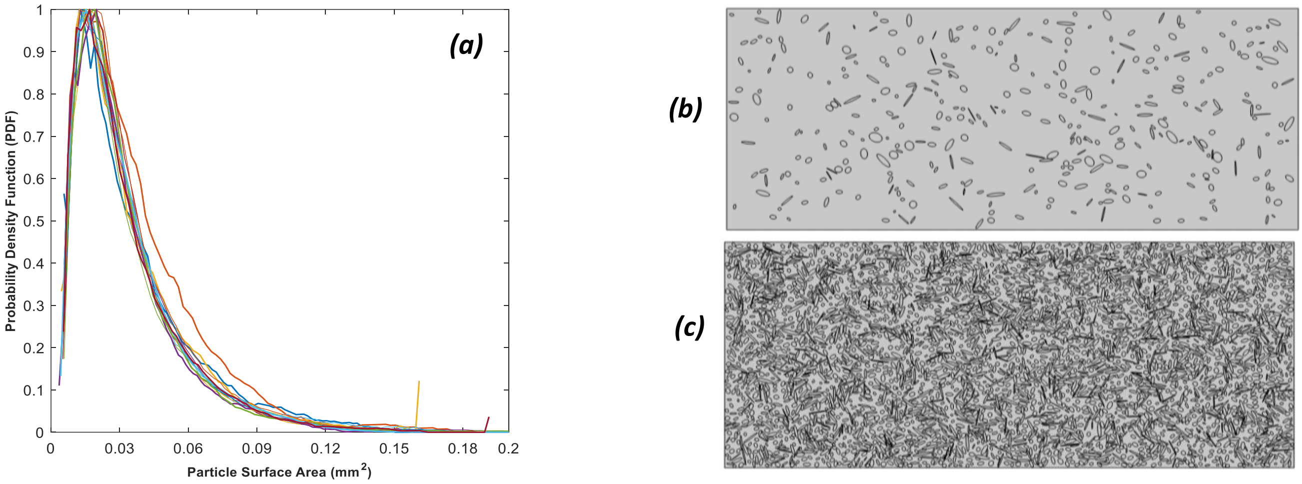

Figure 4.11: LN-(RC)$_2$: **(a)** Log-normal distribution of the samples, **(b)** Sample Nº 1 (S=0.056), **(c)** Sample Nº 14 (S=0.398).

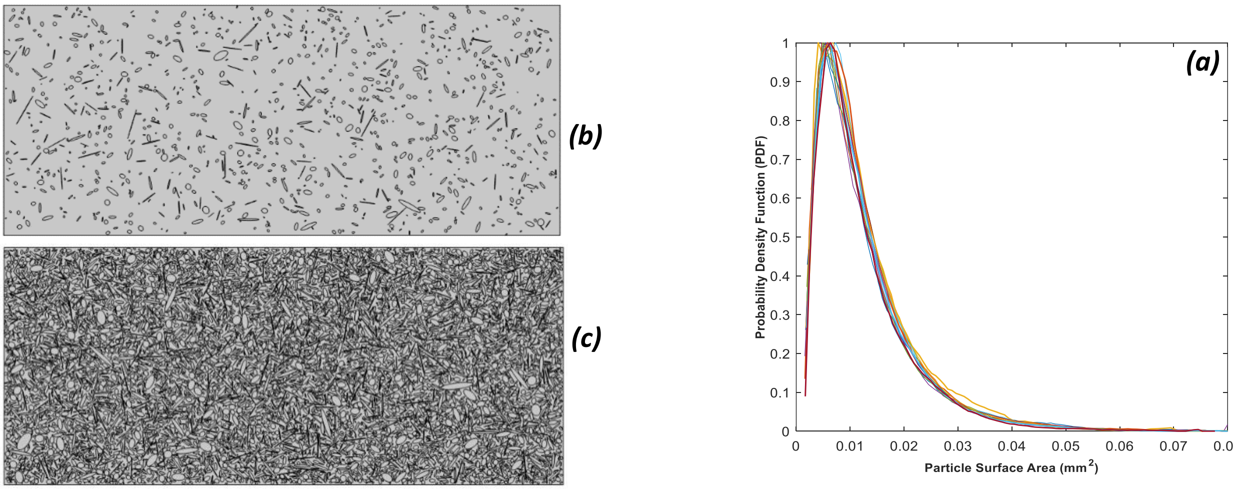

Figure 4.12: LN-(RC)$_3$: (a) Log-normal distribution of the samples, (b) Sample Nº 1 (S=0.50), (c) Sample Nº 14 (S=0.394

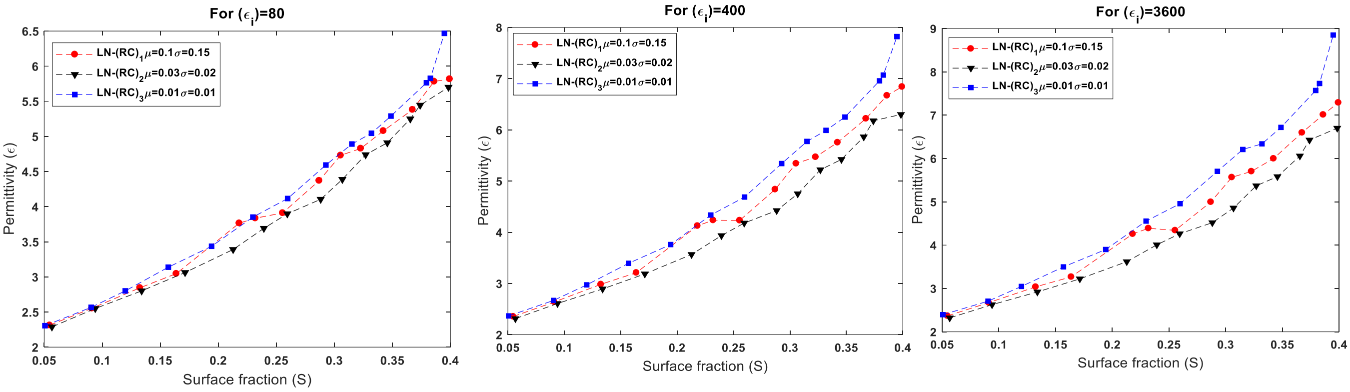

Figure 4.13: Evolution of the effective permittivity as a function of surface fraction for LN-(RC) composites.

4.3.1.3 Rayleigh Distribution (R)

The Rayleigh distribution is a common distribution used to model particle size. This distribution is characterized by a slow exponential decay of the Probability Density Function (PDF) as particle size increases (Figures 4.14.a, 4.15.a, and 4.16.a). Because of this slower decay, the Rayleigh distribution is able to generate a wider range of particle sizes than the Log-normal distribution.

The simulation results obtained with the Rayleigh distribution model of three series of samples (R-(RC)$_1$, R-(RC)$_2$, and R-(RC)$_3$) are summarized in Table 4.3.

. Table 4.3. Characteristics of Three Series of RC Composites Simulated Using the Rayleigh Distribution (R).

	R-(RC)$_1$		**R-(RC)$_2$**		**R-(RC)$_3$**	
	μ=0.01 mm^2 σ=0.006 mm^2		μ=0.003 mm^2 σ=0.001 mm^2		μ=0.001 mm^2 σ = 0.0006 mm^2	
N° **Samples**	***N^0 particles***	***S***	***N^0 particles***	***S***	***N^0 particles***	***S***
1	1198	0.050	4092	0.055	11908	0.050
2	1748	0.094	5881	0.080	15864	0.094
3	2290	0.127	8459	0.116	23776	0.127
4	2830	0.152	11244	0.153	31632	0.152
5	3384	0.181	13012	0.177	37485	0.181
6	3916	0.214	15791	0.213	43327	0.214
7	4447	0.241	18305	0.249	54816	0.241
8	4980	0.270	21673	0.296	54816	0.270
9	5497	0.298	23355	0.315	59619	0.298
10	5977	0.325	24937	0.335	64422	0.325
11	6296	0.355	26501	0.354	69225	0.355
12	7351	0.385	29334	0.376	73066	0.385
13	7670	0.396	33372	0.399	76907	0.396

It is remarkable that, in the context of the Rayleigh distribution, as the value of μ decreases, the number of inclusions increases. This trend is consistent with what we have observed in previous distributions. However, one significant achievement stands out here, demonstrating the effectiveness of the Rayleigh distribution in generating large numbers of particles. Taking the example of sample N^o 13 in Table. 3 with a surface fraction of 0.39, we observed 7670 particles for R-$(RC)_1$ where μ =0.01mm^2 (represented in Figure 4.14.c), 33372 particles for R-$(RC)_2$ with μ =0.03 mm^2 (Figure 4.15.c), and 76907 particles for R-RC_3 with μ=0.001mm^2 (Figure 4.16.c)

In Figure 4.17, we plot the variation of the effective dielectric constant (*ε)* as a function of the size and surface fraction of the ellipsoidal particles for the three permittivities of particles ε_i=80 ,400, and 3600. several salient features can be observed. on the one hand, the results demonstrate that the permittivity (ε) of the composite is influenced both by the surface fraction (*S*) and by the permittivity and the size of the ellipsoidal inclusions. The graphs show that at low inclusion rates ranging from 0.05 to 0.12, the effective permittivity *ε* shows minimal differences whatever the size and permittivity of the inclusions. However, beyond this range, as the surface fraction increases, a notable increase in effective permittivity is observed with divergence between the different simulated composites R-$(RC)_1$, R-$(RC)_2$, and R-$(RC)_3$. This divergence is more pronounced for inclusions with high permittivity (400 and 3600) due to its accentuated contrast with the matrix. The Rayleigh distribution model sensitivity to substantial changes in permittivity, together with intensified polarization effects, amplifies variations between simulated composites with different mean μ and standard deviation σ values. In particular, the R-$(RC)_2$ composite stands out with a higher permittivity than R-$(RC)_1$ and R-$(RC)_3$ because its inclusion size distribution provides superior balance. While R-$(RC)_1$ contains larger inclusions that may not interact effectively with the electric field due to their size, Conversely, in R-$(RC)_3$, the abundance of very small inclusions of very similar size, where the standard deviation is too small (σ =0.0006 mm^2) offers limited interaction with the electric field, leading to minimal impact on permittivity.

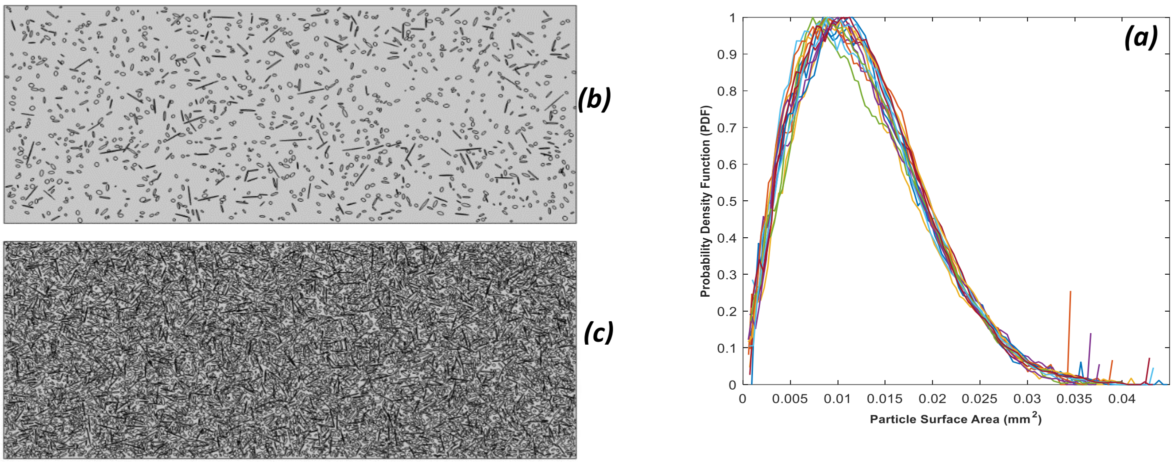

Figure 4.14: R-(RC)$_1$: **(a)** Rayleigh distribution of the samples, **(b)** Sample No 1 (S=0.50), **(c)** Sample Nº 13 (S=0.396).

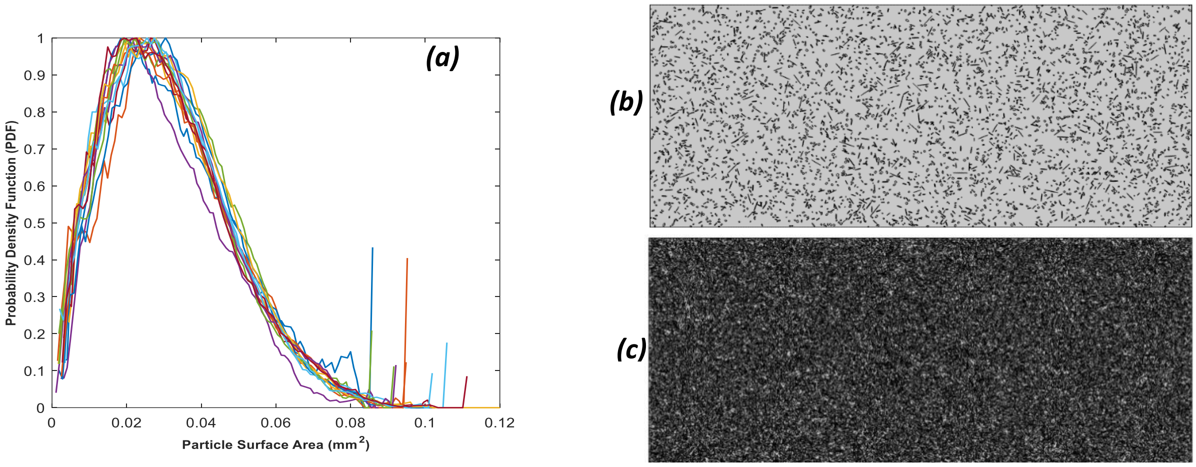

Figure 4.15: R-(RC)$_2$: **(a)** Rayleigh distribution of the samples, **(b)** Sample No 1 (S=0.55), **(c)** Sample Nº 13 (S=0.399).

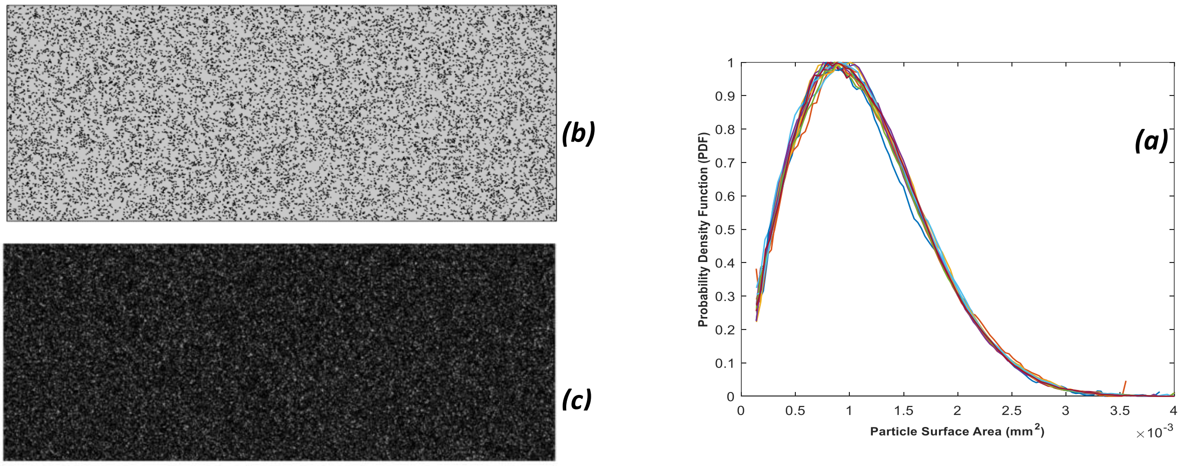

Figure 4.16: R-(RC)$_3$: **(a)** Rayleigh distribution of the samples, **(b)** Sample No 1 (S=0.50), **(c)** Sample Nº 13 (S=0.396).

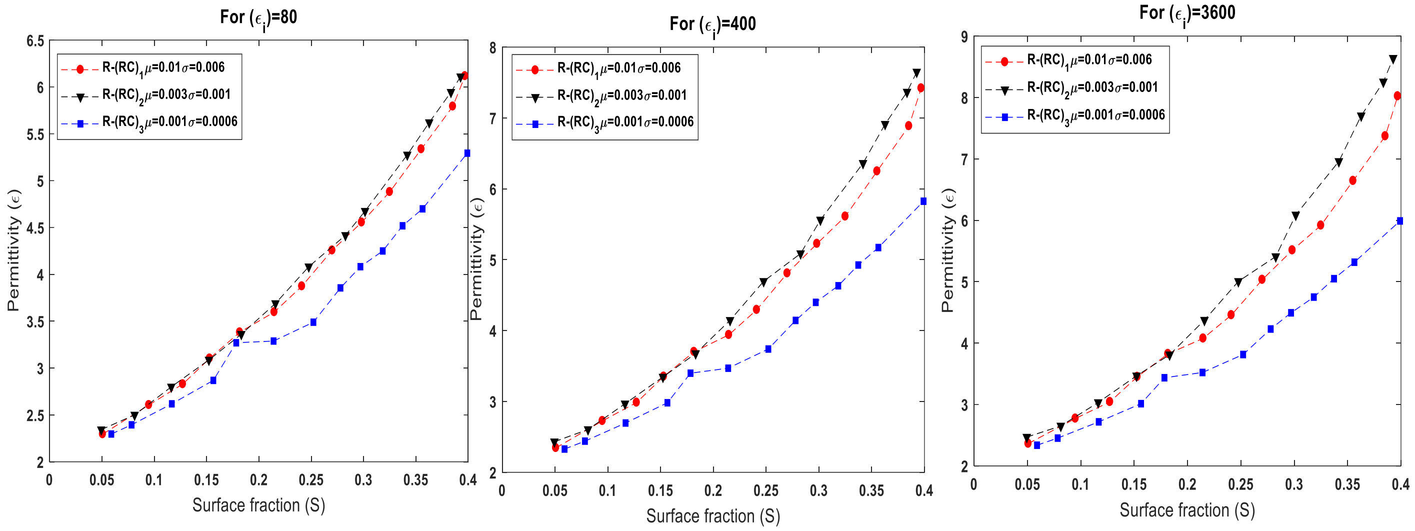

Figure 4.17: Evolution of the effective permittivity as a function of surface fraction for R-(RC) composites.

4.3.2 Simulated results *Vs* theorical models

Figures 4.18 and 4.19 show the correlation between the simulation results and the analytical models. The dielectric constant of the RC composites is plotted for each model as a function of the surface fraction of the ceramic filler particles. For the different distributions and particle sizes, the simulation results are presented alongside the theoretical predictions in each figure to examine the degree of agreement between them.

In order to quantify the average deviation between different values predict by models and the values found by simulation, a Root Mean Square Error (RMSE) was calculated by the following equation (Eq.13):

$$\mathrm{RMSE} = \sqrt{\frac{1}{N}\sum_{i=1}^{N}\left(\varepsilon_{exp} - \varepsilon_{model}\right)^{2}} \qquad (13)$$

Where N represents the number of samples, while ε_{exp} and ε_{model} represent the simulated and theorical permittivity, respectively.

4.3.2.1 Original empirical models

Figure 4.18 presents a comparison between the theoretical predictions of the original models and the corresponding simulation results. After careful examination of the graphs, it becomes apparent that models by Lichtenecker, Bruggeman, and Looyenga fail to accurately align with our simulated results. However, what is truly remarkable is the net advantage observed in the case of the

Maxwell-Garnett (MG) model. This model displays a higher level of accuracy in its predictions, especially when dealing with RC composites with moderate inclusion permittivity (ε_i = 80). Nevertheless, as the permittivity of inclusions increases to levels of 400 and 3600, the disparities between our empirical results and theoretical projections derived from the Maxwell-Garnett model become more evident.

It is imperative to emphasize that the limitations inherent in the Maxwell-Garnett model appear in situations where interactions between particles become more complex due to high permittivity values with more pronounced particle concentration. it is remarkable in most graphs, when the surface fraction remains less than 0.15, the performance of the MG presents a certain degree of adequacy. Conversely, for surface fractions greater than 0.15, the MG equation does not correctly describe the simulated results, independently of the particle size and the type of distribution.

Table 4 lists the RMSE calculation between the dielectric constant predicted by the original mixing laws and the simulation results, for all cases of RC composites.

On the one hand, when ε_i = 80, we note that the error is smaller than 14 for every law in Table 4.4. this error becomes more important when the permittivity of the particles increases. Taking the case of N-$(RC)_1$ as an example, applying Lich's law, we find an RMSE= of 2.29 for ε_i =80, it becomes 5.98 for ε_i =400, then 16.43 for ε_i =3600. On the other hand, all results show that the Maxwell-Garnett model has the lowest error for all distributions. This could be due to the sensitivity of this model in predicting the effective properties of composites when the shape of the inclusions is close to spherical. It is noteworthy that this group of original laws does not effectively predict the dielectric constant because they do not have information about the size and distribution of the particles in the matrix.

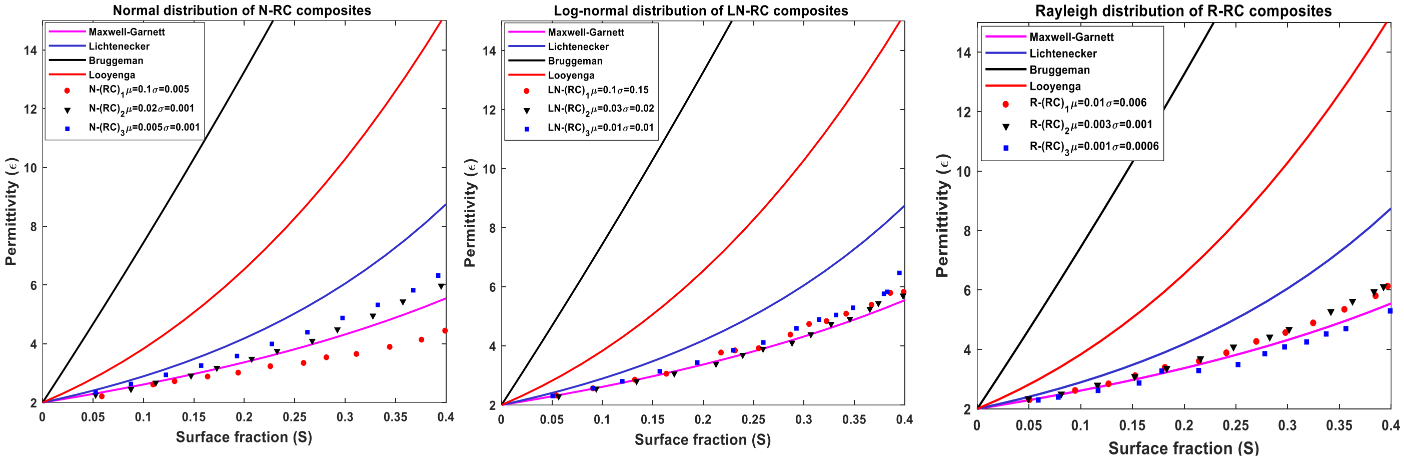

(a) For ε_i=80

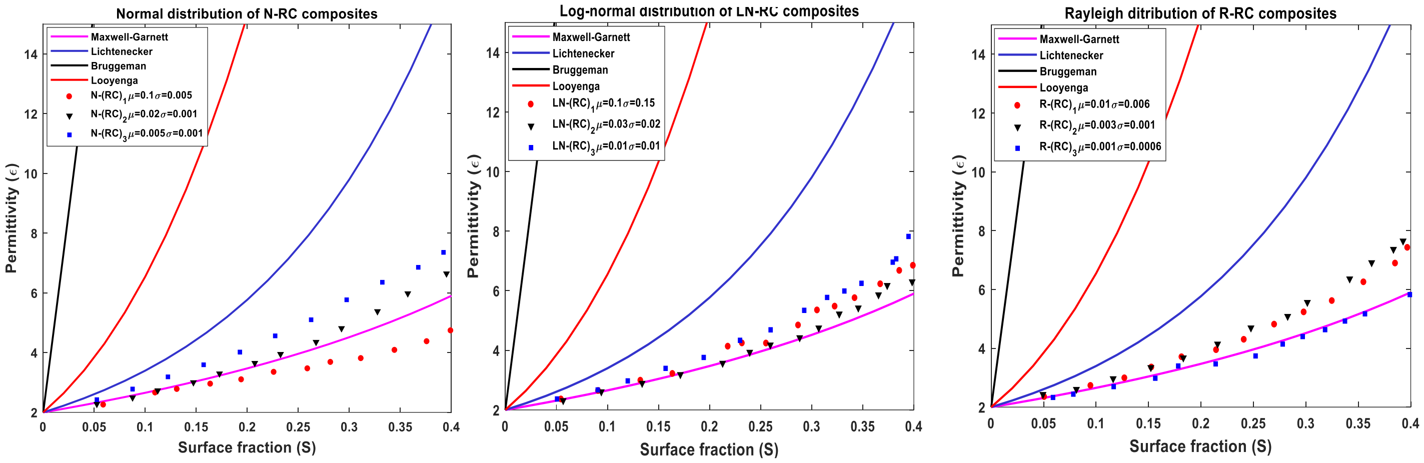

(b) For ε_i=400

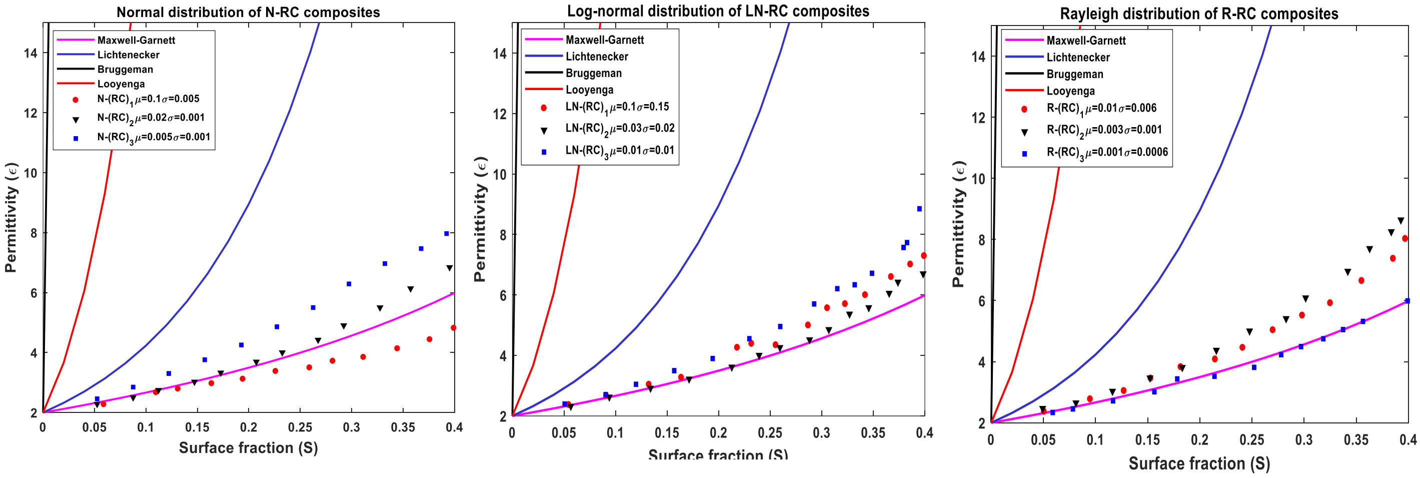

(c) For ε_i=3600

Figure 4.18: The effective permittivity modeling by original mixing laws for the different simulated RC composites.

Table 4.4. Root Mean Square Error values of original mixture laws for the different simulated RC composites.

	Models	**Maxwell-Garnett**	**Lichtenecker**	***Bruggeman***	***Looyenga***
RMSE for $\varepsilon_i = 80$	**N-RC$_1$**	0.6399	2.2967	13.8217	6.053
	N-RC$_2$	0.2355	1.293	12.1959	4.7817
	N-RC$_3$	0.4839	1.11	12.2737	4.7262
	LN-RC$_1$	0.2312	1.5782	13.7945	5.6132
	LN-RC$_2$	0.1105	1.7117	13.9626	5.7462
	LN-RC$_3$	0.3997	1.442	13.7049	5.5221
	R-RC$_1$	0.2786	1.408	13.0052	5.2042
	R-RC$_2$	0.3671	1.3511	13.0724	5.214
	R-RC$_3$	0.2003	1.7829	13.1908	5.4648
RMSE for ε_i =400	**N-RC$_1$**	0.6751	5,9812	75,7035	24,2876
	N-RC$_2$	0,3778	4,445	70,0941	21,2408
	N-RC$_3$	0,9915	4.1102	71,5216	21.6725
	LN-RC$_1$	0,5855	5,18	79,1841	24,9691
	LN-RC$_2$	0,2891	5,4281	79,5433	25,132
	LN-RC$_3$	0,9748	4,8931	79,2298	24,9848
	R-RC$_1$	0,7382	4,6625	74,7894	23,2108
	R-RC$_2$	1,0167	4,4931	75,4467	23,4257
	R-RC$_3$	0,1115	5,1562	73,995	5.4648
RMSE for ε_i =3600	**N-RC$_1$**	0,6808	16,4342	695,9904	159,6589
	N-RC$_2$	0,4255	13,7069	652,0291	143,6422
	N-RC$_3$	1,3448	13,679	670,4512	150,6533
	LN-RC$_1$	0,7587	16,3582	738,379	171,8925
	LN-RC$_2$	0,3903	16,4427	739,0499	170,6463
	LN-RC$_3$	1,3611	16,1096	741,84	174,659
	R-RC$_1$	0,9765	15,0867	698,7134	160,6552
	R-RC$_2$	1,4737	14,9055	706,9592	163,7853
	R-RC$_3$	0,0878	14,9197	684,7853	152,5478

4.3.2.2 modified empirical models

The comparison between the modified theoretical models and the simulated results for the different dielectric composites is shown in Figure 4.19. Obviously, these models show improved performance compared to the original laws. This improvement can be attributed to the incorporation of information on the shape and polarization of inclusions into these models, highlighting their importance in predicting composite dielectric permittivity.

More precisely, when examining the graphs for ε_i =80, we observe that the models of Maxwell-Garnett, Yamada project with greater precision than those of Bruggeman and Bergman, in particular for surface fractions of charge greater than 0.2.

To go further, the models of Maxwell Garnett, Yamada were selectively applied to scenarios of high inclusion permittivities (ε_i = 400 and ε_i = 3600). This research aimed to understand the variable influence of factors related to shape and depolarization.

Looking at the Maxwell-Garnett and Yamada models, the Maxwell-Garnett depolarization factor (A) and Yamada shape parameter (n) show limited variation with increased inclusion permittivity. More specifically, Maxwell Garnett's depolarization factor (A) is a parameter that measures the capacity of a material to polarize in response to an applied electric field. Lower A values indicate a high polarizability of the inclusions, this can lead to an improved effective permittivity of the composite material. Considering the case of the normal distribution of RC composites for ε_i =400 in Figure 4.19.b. it is clear that N-$(RC)_3$, which gives the best permittivity, has a lower A factor of 0.23 compared to N-$(RC)_1$ and N-$(RC)_2$, which have factors of 0.47 and 0.28, respectively.

Furthermore, in the context of the Yamada model, taking the same example, we observe a transition from n = 2.1 for N-$(RC)_1$ to n = 4.4 for N-$(RC)_3$. An n value of 2.1 implies relatively rounded but not spherical ellipsoidal inclusions, while n = 4.4 suggests elongated inclusions. This increased elongation corresponds to a stronger alignment of the inclusions with the electric field, potentially contributing to distinct electrical responses within the composite.

Table 4.5 summarizes the RMSE found, determined by Eq. (13), between theoretical and simulated results for the modified mixing laws. we can see that the modified Yamada and Maxwell Garnett models give the best fit to the simulated results compared to Bruggeman and Bergman with an error value less than 0.2.

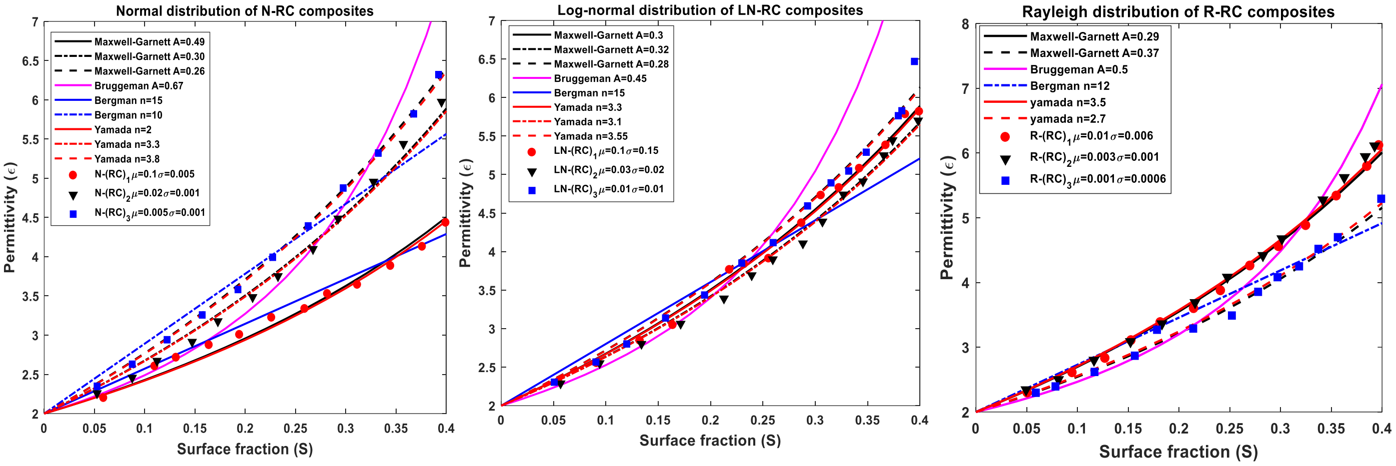

(a) For ε_i=80

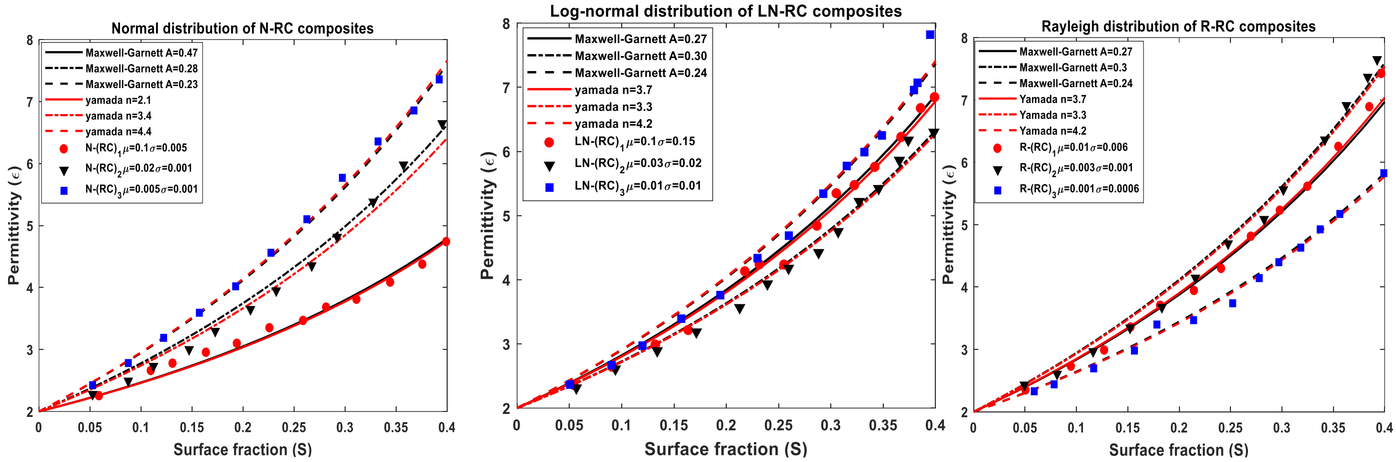

(b) For

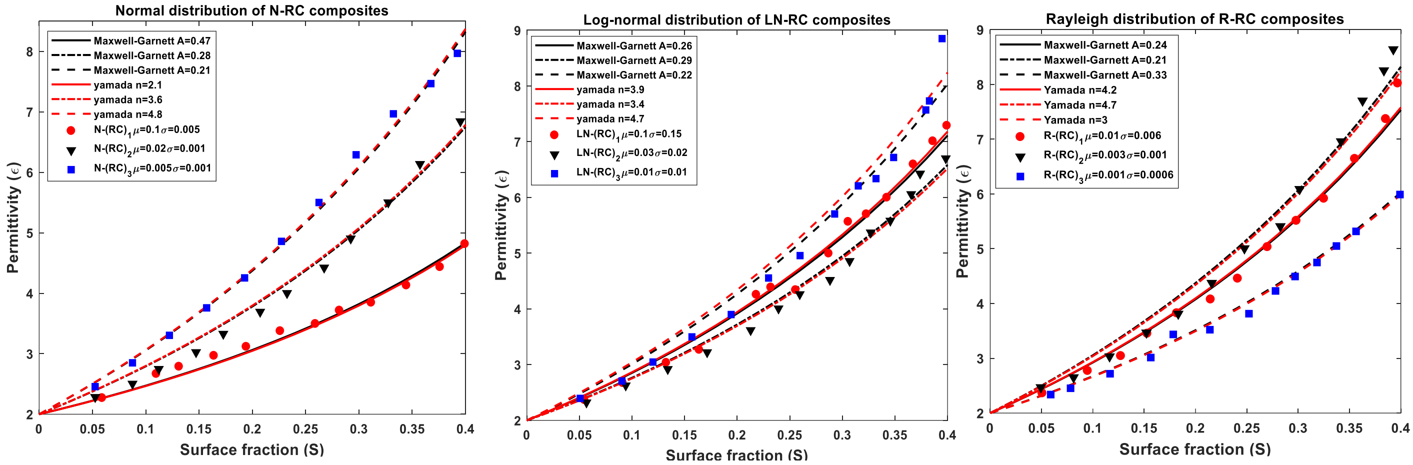

(c) For ε_i=3600

Figure 4.19: The effective permittivity modeling by modified mixing laws for the different simulated RC composites.

Table 4.5. Root Mean Square Error values of modified mixture laws for the different simulated RC composites.

	Models	**Modified MG**	**Modified *Bruggeman***	***Bergman***	***Yamada***
RMSE for $\varepsilon_i = 80$	**N-RC$_1$**	0.0956	1.7969	0.0999	0.0943
	N-RC$_2$	0.1061	0.8175	0.3095	0.1113
	N-RC$_3$	0.0343	1.8564	0.2560	0.0376
	LN-RC$_1$	0.0802	1.1034	0.8827	0.0827
	LN-RC$_2$	0.0935	1.1590	0.7364	0.0914
	LN-RC$_3$	0.1298	0.9555	1.0674	0.1309
	R-RC$_1$	0.0678	1.0027	0.2771	0.0771
	R-RC$_2$	0.1032	0.9008	0.3028	0.0805
	R-RC$_3$	0.0821	1.5050	0.2102	0.0820
RMSE for $\varepsilon_i = 400$	**N-RC$_1$**	0.1014	-	-	0.0994
	N-RC$_2$	0.1478	-	-	0.1616
	N-RC$_3$	0.0904	-	-	0.0811
	LN-RC$_1$	0.1225	-	-	0.1230
	LN-RC$_2$	0.1431	-	-	0.1436
	LN-RC$_3$	0.1820	-	-	0.1786
	R-RC$_1$	0,1693	-	-	0,1495
	R-RC$_2$	0.1552	-	-	0.1582
	R-RC$_3$	0,0879	-	-	0,081
RMSE for $\varepsilon_i = 3600$	**N-RC$_1$**	0.1008	-	-	0.1023
	N-RC$_2$	0.1559	-	-	0.1586
	N-RC$_3$	0.1312	-	-	0.1259
	LN-RC$_1$	0.1548	-	-	0.1468
	LN-RC$_2$	0.1746	-	-	0.1746
	LN-RC$_3$	0.2957	-	-	0.3024
	R-RC$_1$	0,19	-	-	0,184
	R-RC$_2$	0,2627	-	-	0,279
	R-RC$_3$	0,0983	-	-	0,0878

4.4 Conclusion

In this article, we studied binary epoxy resin/ceramics (RC) composite materials through a series of 2D simulations using the finite element method (FEM) under quasistatic conditions. A new algorithm was developed and implemented in MATLAB to generate random distributions of ellipsoidal ceramic particles within the epoxy resin polymer matrix which has dimensions of a WR90 rectangular waveguide.

This work aimed to conduct a thorough examination of the impact of permittivity, concentration, distribution and particle size on the dielectric behavior of the RC composite on the one hand, and to meeting the challenge to simulate a significant number of ceramic particles distributed in the matrix on the other hand.

Divided into two distinct parts, in the first one, the research effort focused on the study of three distribution models (Normal, Log-normal, and Rayleigh) to describe the distribution of surface particles at the matrix level. For each distribution model, three cases of particle sizes were examined and applied on three RC composites with an inclusion permittivity of 80, 400, and 3600 leaving the permittivity of the matrix fixed. Notably, in all models, the results showed that the effective permittivity of all RC composites increases when the permittivity and the surface fraction of the particles also increase. Furthermore, the results show the major impact of particle size and distribution on the interfacial interactions in the material, where it was observed that composites that contain a diversity of particle sizes introduce an obvious effect on the overall permittivity of composite. In addition, the Rayleigh distribution demonstrated exceptional efficiency in allowing the successful simulation of more than 70,000 non overlap ellipsoidal particles distributed in the rectangular matrix, which is not the case for the Normal and Log-normal distributions.

In the second part, theoretical “mixing laws” models were applied to predict the dielectric permittivity of our RC materials, stratified into two categories. The first category includes classical models with spherical inclusions dispersed in a continuous matrix. In contrast, the second category contains modified laws that introduce information about the shape and depolarization factors of particles. Through a systematic analysis of these models with our different simulated results, it becomes evident that the modified models more accurately predict the dielectric behavior of composites. it was found that the modified models of Maxwell-Garnett and Yamada turned out to be exceptionally accurate. where it was observed that these models agree with the simulated results with an error lower than 0.2.

The implications of this research are of considerable importance, as they contribute to the development of new optimized materials (such as phase shifters, filters, and various microwave devices) through a comprehensive analysis of their electromagnetic properties before their production using detailed simulations.

General Conclusion

The work presented in this thesis focused on the experimental and numerical characterization of binary and ternary dielectric composites, supported by theoretical modeling based on various mixing laws. These three complementary approaches; experiment, simulation, and theory, enabled a precise and consistent analysis of the dielectric behavior of the materials studied.

Experimentally, two systems were examined. The first is a binary composite consisting of an Epoxy resin matrix loaded with Barium Titanate powder. The second is a ternary composite, prepared from the same matrix, in which two powders; Manganese-Zinc Ferrite and Calcium Titanate; were homogeneously mixed to form the dispersed phases. Two measurement techniques were used to characterize these materials: a fixed-frequency rectangular waveguide X-band and time-domain spectroscopy (TDS) covering a broad frequency band.

Numerical characterization was performed using the finite element method FEM applied to several binary composites under quasi-static conditions. This approach has the advantage of being able to handle dense materials containing geometrically complex inclusions at high concentrations, situations in which analytical models reach their limits. The simulations also take into account the interactions between inclusions randomly dispersed within the matrix, unlike classical mixing laws. They thus offer an efficient way to predict the dielectric behavior of materials before their fabrication, resulting in significant savings in time and resources.

The study was organized into three parts. The first part focused on the binary composite based on epoxy resin and barium titanate. A comparative study was conducted between the dielectric properties obtained using a rectangular waveguide measurement system at a fixed frequency of 9.49 GHz and those extracted by TDS spectroscopy covering the DC–9.49 GHz range. In this frequency range, the permittivity measured by TDS was found to be almost constant, allowing for a consistent and reliable comparison between the two techniques. The analysis focused on relative permittivity, conductivity, and loss and quality factors. The experimental results were then compared with theoretical models derived from mixing laws to identify the most appropriate approaches for predicting the dielectric behavior of this composite.

The second part presented the raw real and imaginary permittivity results for the ternary composite, obtained by TDS between DC and 5 GHz, supplemented by quasi-static measurements at 500 MHz for different barium titanate concentrations.

The third part focused on the finite element numerical modeling of two-phase composites consisting of an epoxy matrix and ellipsoidal ceramic inclusions. The simulations allowed us to study the influence of several parameters, including charge concentration, the random distribution of particles according to three statistical models (normal, log-normal, and Rayleigh), particle size, and the intrinsic permittivity of the ceramic phase. Detailed analysis of the results and their comparison with different mixing laws made it possible to identify the limits of validity of these models. A specific program was also developed to simulate a large number of inclusions, thus bringing the modeling closer to real-world configurations and representing a methodological challenge that was successfully met.

Several research avenues can be explored following this work, which was based on two-dimensional simulations of binary composites and experimental characterization using TDS and rectangular waveguides:

1**) Extension of the numerical modeling to three-dimensional simulations:** Moving from a 2D to a 3D modeling approach would allow for a more realistic representation of the spatial distribution of inclusions, their interactions, and percolation phenomena. Such a development would improve the accuracy of determining the effective permittivity, particularly for highly filled materials or those with non-ellipsoidal inclusions.

2) Simulation of ternary and quaternary composites with greater geometric diversity of inclusions: Future studies could incorporate complex multiphase systems as well as particles of various shapes (fibers, platelets, irregular inclusions). This would pave the way for a more detailed exploration of the role of microstructure on electromagnetic properties.

3) Microwave characterization in transmission and reflection on three-dimensional devices: The use of suitable beamlines or waveguides (circular waveguide, resonant cavity, coplanar beamline, etc.) would offer a more comprehensive analysis of dielectric and magnetic materials and would allow for the validation of models in configurations close to application conditions.

4) Experimental and numerical study in coaxial waveguides: The development of methodology combining coaxial measurements and FEM simulations in coaxial geometry would allow for the evaluation of consistency between modeling and experiment. This configuration is particularly well-suited for materials with a wide range of permittivities.

5) Integration of artificial intelligence techniques for the optimization of material properties: Machine learning could be used to predict the effective permittivity from microstructural parameters or to identify optimal compositions that meet specific electromagnetic criteria.

6) Characterization of nanocomposites: Investigating nanoscale systems would offer new perspectives, particularly due to the surface effects and interfacial polarization phenomena that are accentuated at these dimensions. This would extend current results to high-performance materials.

7) Evaluation of materials for antenna or microwave applications: The studied or simulated composites could be integrated as substrates, superlayers, or filler materials in antenna structures. Analyzing their impact on efficiency, bandwidth, or reflection coefficient would constitute an important application extension.

References

[1] D. Hull and T. W. Clyne, *An Introduction to Composite Materials*. Cambridge: Cambridge University Press, 1996.

[2] S. Orlowska, Conception et prédiction des caractéristiques des matériaux composites à deux et trois phases par la modélisation et la validation expérimentale, Ph.D. dissertation, École Centrale de Lyon, France, Jan. 2003..

[3] T. D. Ngo, *Composites and Their Applications*. Alberta Innovates, Canada: IntechOpen, 2020.

[4] R. Sharma, N. Hooda, A. Hooda, S. Khasa, D. Verma, and H. Dhull, "Dielectric and magnetic study of NiCuZn spinel ferrites," *ECS J. Solid State Sci. Technol.*, vol. 10, no. 9, Art. no. 091013, 2021.

[5] A. Ashery, S. A. Gad, A. H. Gaballah, and G. M. Turky, "Fabrication, electrical and dielectric characterization of Au/CNT/TiO_2/SiO_2/p-Si/Al with high dielectric constant, low loss dielectric tangent," *ECS J. Solid State Sci. Technol.*, vol. 10, no. 5, Art. no. 051003, 2021.

[6] S. Berthier, *Optique des Milieux Composites*. Paris: Polytechnica, 1993.

[7] S. Ramo, J. R. Whinnery, and T. Van Duzer, *Fields and Waves in Communication Electronics*, 3rd ed. New York: John Wiley & Sons, 1994.

[8] J. C. Maxwell Garnett, "Colours in metal glasses and in metallic films," *Philos. Trans. R. Soc. Lond. A*, vol. 203, pp. 385–420, 1904.

[9] D. A. G. Bruggeman, "Berechnung verschiedener physikalischer Konstanten von heterogenen Substanzen," *Ann. Phys. (Leipzig)*, vol. 24, pp. 636–679, 1935.

[10] C. J. F. Böttcher, *Theory of Electric Polarization*. Amsterdam: Elsevier, 1952.

[11] H. Looyenga, "Dielectric constants of heterogeneous mixtures," *Physica*, vol. 31, pp. 401–406, 1965.

[12] K. Lichtenecker, "Dielectric constant of heterogeneous mixtures," *Phys. Z.*, vol. 30, pp. 805–820, 1929.

[13] S. Torquato, *Random Heterogeneous Materials: Microstructure and Macroscopic Properties*. New York: Springer, 2002.

[14] A. Spanoudaki and R. Pelster, "Effective dielectric properties of composite materials: The dependence on the particle size distribution," *Phys. Rev. B*, vol. 64, Art. no. 064205, Jul. 2001.

[15] A. Plyushch, *Dielectric Properties of Composites with Carbon Nanoparticles*. Doctoral dissertation, Vilnius University, Center for Physical Sciences and Technology, Vilnius, Lithuania, 2018.

[16] T. Arab, H. Khouni, N. Bouzit, and J. P. Martínez Jiménez, "Study of dielectric behavior of ternary composites of epoxy-barium titanate with iron oxide and ferrite in the band (DC- 12.5 GHz)." Inorg. Nan. Met. Chem., (2021).

[16] A. Kelly, *Concise Encyclopedia of Composite Materials*, Elsevier, 2012.

[17] H. F. Mark, N. M. Bikales, C. G. Overberger, and G. Menges, *Encyclopedia of Polymer Science and Engineering*, vol. 4, Wiley-Interscience, New York, 1986.

[18] S. R. P., *Composite Polymeric Materials*, Applied Science, London, 1982.

[20] C. Elissalde, U.-C. Chung, G. Philippot, J. Lesseur, R. Berthelot, D. Sallagoity, et al., "Innovative architectures in ferroelectric multi-materials: Chemistry, interfaces and strain," *J. Adv. Dielectrics*, vol. 5, p. 1530001, 2015, doi: 10.1142/S2010135X15300017.

[21] G. Philippot, C. Elissalde, M. Maglione, and C. Aymonier, "Supercritical fluid technology: A reliable process for high quality BaTiO3 based nanomaterials," *Adv. Powder Technol.*, vol. 25, pp. 1415–1429, 2014, doi: 10.1016/j.apt.2014.02.016.

[22] M.J. Abdullah, D.K. Das-Gupta, Electrical properties of ceramic/polymer composites, IEEE Trans. Electr. Insul. 25 (3), pp. 605-610, 1990.

[23] R. A. Flinn and P. K. Trojan, *Engineering Materials and Their Applications*, 4th ed., John Wiley & Sons, 1990.

[24] Abdallah BENHAMOUDA, "Caractérisation électromagnétique de polymère chargé par des mélanges de titanates et d'oxyde en utilisant la spectroscopie en domaine temporel," Doctorat thesis, Ferhat Abbas University, Setif, 2010.

[25] A. Brahimi, *Élaboration et validation expérimentale de modèles prédictifs du comportement diélectrique des composites à base de titanate multi-phases en hyperfréquence*, Ph.D. dissertation, Ferhat Abbas University, Sétif, 2022.

[26] L. Houf, *Développement de nanocomposites à propriétés piézoélectriques et optiques non-linéaires*, Ph.D. dissertation, Université de Grenoble, 2011.

[27] J.-F. Capsal, *Élaboration et analyse des propriétés physiques de nanocomposites hybrides ferroélectriques*, Ph.D. dissertation, Université de Toulouse, Université Toulouse III – Paul Sabatier, 2008.

[28] H. S. Nalwa, *Handbook of Low and High Dielectric Constant Materials and Their Applications*, 2 vol., Academic Press, 1999.

[29] Z. Ahmad, “Polymer dielectric materials,” in *Dielectric Materials*, M. A. Silaghi, Ed., InTech, 2012.

[30] J. H. Luft, “Improvements in epoxy resin embedding methods.” The Journal of biophysical and biochemical cytology., **9**, 409 (1961).

[31] B. Ertuğ, “The overview of the electrical properties of barium titanate,” *American Journal of Engineering Research*, vol. 2, pp. 1–7, 2013.

[32] S. Bouchareb, *Étude de matériaux irradiés sous faisceau d'électrons*, Ph.D. dissertation, Université de Toulouse, 2014.

[33] J. Martinez-Vega, *Dielectric Materials for Electrical Engineering*, Wiley-ISTE, Hoboken, NJ, USA, and London, UK, 2010.

[34] K. W. Wagner, “Explanation of the dielectric fatigue phenomenon on the basis of Maxwell’s concept.” Arkiv für Electrotechnik., **2**, 371-387 (1914).

[35] R. W. Sillars, “The properties of a dielectric containing semiconducting particles of various shapes.” Journal of the Institution of Electrical Engineers., **80**, 378-394 (1937).

[36] D. H. Nguyen, *Étude des propriétés électriques des élastomères silicones utilisés pour l’isolation électrique*, Ph.D. dissertation, Université Joseph-Fourier, Grenoble I, 2005.

[37] J. C. Maxwell, *A Treatise on Electricity and Magnetism*, 2nd ed., Oxford: Clarendon Press, 1881.

[38] F. Gardiol, *Electromagnétisme*, Vol. 3, Lausanne: Presses Polytechniques Romandes, 1989.

[39] R. Coelho and A. Bernard, *Les diélectriques: propriétés diélectriques des matériaux isolants*, Paris: Hermes, 1993.

[40] J. C. Mage, "Origine des pertes dans les matériaux," *Rev. Générale Électricité*, pp. 24–31, 1991.

[41] A. Y. Abdelhedi, *Élaboration et caractérisations diélectriques de céramiques ferroélectriques et/ou relaxeur de formule MSnO3-NaNbO3 (M = Ba, Ca)*, Ph.D. dissertation, Université de Sfax, 2005.

[42] C. Huber, *Synthesis and characterisation of new tunable ferroelectric materials for hyperfrequency applications*, Ph.D. dissertation, Université Sciences et Technologies, Bordeaux I, 2003.

[43] A. Boudefel, *Propriétés diélectriques de polymères composites et leurs applications en microélectronique*, Ph.D. dissertation, Université Badji Mokhtar Annaba, Faculté des Sciences de l'Ingénieur, 2009.

[44] Z.-G. Ye, *Handbook of Advanced Dielectric, Piezoelectric and Ferroelectric Materials: Synthesis, Properties and Applications*, Elsevier, 2008.

[45] M. H. Frey, Z. Xu, P. Han, and D. A. Payne, "The role of interfaces on an apparent grain size effect on the dielectric properties for ferroelectric barium titanate ceramics," *Ferroelectrics*, vol. 206, pp. 337–353, 1998, doi: 10.1080/00150199808009168.

[46] K. Kinoshita, "Grain-size effects on dielectric properties in barium titanate ceramics," *J. Appl. Phys.*, vol. 47, p. 371, 1976, doi: 10.1063/1.322330.

[47] G. Arlt, D. Hennings, and G. de With, "Dielectric properties of fine-grained barium titanate ceramics," *J. Appl. Phys.*, vol. 58, p. 1619, 1985, doi: 10.1063/1.336051.

[48] C. Brosseau, "Modelling and simulation of dielectric heterostructures: A physical survey from an historical perspective," *J. Phys. D: Appl. Phys.*, vol. 39, p. 1277, 2006.

[49] S. Berthier, *Optique des milieux composites*, Polytechnica, Paris, Jun. 1999.

[50] T. Guillot, *Contribution à la modélisation des propriétés électromagnétiques des mélanges aléatoires du type diélectrique/conducteur*, Ph.D. dissertation, Université de Paris VI, 1992.

[51] J. R. Birchak, C. Z. G. Gardner, J. E. Hipp, and J. M. Victor, "High dielectric constant microwave probes for sensing soil moisture," *Proc. IEEE*, vol. 62, p. 93, 1974.

[52] H. Looyenga, "Dielectric constants of heterogeneous mixtures," *Physica*, vol. 31, p. 401, 1965.

[53] O. Wiener, "Mathematisch-Physikalische Klasse," *Leipziger Berichte*, vol. 62, p. 256, 1910.

[54] K. Lichtenecker and K. Rother, "Deduction of the logarithmic mixture law from general principles," *Phys. Z.*, vol. 32, p. 255, 1931.

[55] A. M. Bottreau, *Caractérisation électromagnétique de quelques composites polymère carbone 2ème partie :Modélisation*, Annales, Université Blaise Pascal, 1997.

[56] D. J. Bergman, "The dielectric constant of a composite material — a problem in classical physics," *Phys. Rep.*, vol. 43, no. 9, pp. 377–407, Jul. 1978.

[57] T. Yamada, T. Ueda, and T. Kitayama, "Piezoelectricity of a high-content lead zirconate titanate/polymer composite," *J. Appl. Phys.*, vol. 53, p. 4328, 1982.

[58] J. Z. Zugelter, *Time Domain Transmission Line Measurements with the Speedy Delivery Signal*, Ph.D. dissertation, 2010.

[59] B. Pettinelli, A. Cereti, A. Galli, and F. Bella, "Time Domain Reflectometry: Calibration Techniques for Accurate Measurement of the Dielectric Properties of Various Materials," *Rev. Sci. Instrum.*, vol. 73, pp. 3553–3562, 2002.

[60] A. Cataldo, L. Catanuricci, L. Tarricone, F. Attivissimo, and A. Trotta, "A Frequency-Domain Method for Extending TDR Performance in Quality Determination of Fluids," *Meas. Sci. Technol.*, vol. 18, pp. 675–688, 2007.

[61] A. Merzouki, *Étude et mise en œuvre d'une méthode de caractérisation diélectrique en domaine de temps, utilisant le changement d'admittance entre une ligne coaxiale et une cellule cylindrique. Applications.*, Ph.D. thesis, Université de Bordeaux I, 1992.

[62] Cole, R.H., *Evaluation of dielectric behavior by time domain spectroscopy*, II. Complex permittivity J. Phys. Chem., 79, pp. 1469-1474, 1975.

[63] Y**.** Dutuit, La transformation de Fourier discrète en spectroscopie temporelle. Rev phys. Appl., **14**. 639, 1973.

[64] N. Bouzit , Caractérisation diélectrique de matériaux hétérogènes par spectroscopie temporelle: Application à l'étude de composites polyesters chargés par des titanates,"PhD thesis, Ferhat Abbas University, Setif, 2002.

[65] H. Khouni, Modélisation et Simulation Numérique de Mélanges de Matériaux Diélectriques binaire et ternaire, PhD thesis, Ferhat Abbas University, Setif, 2017**.**

[66] A. Merzouki, Activity Report, University of Bordeaux I, 1980.

[67] P. F. Combes, Microwaves Vol. 1: Lines and Cavities, pp. 241-248, Dunod, 1996.

[68] S. Ramo, J. R. Winnery, T. Van Duzer, Fields Waves in Communication Electronics, p 411-518, 2èmeEd John Wiley & Sons, 1984.

[70] C. Ang, Z. Yu, R. Guo, et A. Bhalla, Calculation of dielectric constant and loss of two-phase composites, J. Appl. Phys. 93, 3475, 2003.

[71] X. Zhao, Y. Wu, Z. Fan, et F. Lei, Three-dimensional simulations of the complex dielectric properties of random composites by finite element method**,** J. Appl. Phys. 95, 8110, 2004.

[72] J. Chaskalovic, "Méthode des éléments finis pour les sciences de l'ingénieur", Tec et Doc, Lavoisier, 2004.

[73] L. Zhou et L. E. Davis,Finite-element method with edge elements for waveguides loaded with ferrite magnetized in arbitrary direction, IEEE Trans. on MTT. 44, No. 6, June (1996).

[74] P. Silvester, Finite Element for Electrical Engineers, (Cambridge University Press, Cambridge, 1996.

[75]A. Mejdoubi and C. Brosseau, Dielectric response of perforated two-dimensional lossy heterostructures: A finite-element approach, J.Appl.Phys. 100, 094103 (2006).

[76] Comsol AB, Comsol Multiphysics Reference Manual, Stockholm, Sweden.

[77] D. Djouada, N. Bouzit, R. Delfouf, L. Chioukh, J. P. Martinez Jimenez, "Dielectric Characterization of Heterogeneous Composites Using Time Domain Spectroscopy and Microwave Test Benches in Microwave Frequency." ECS J. Solid State Sci. Technol., 12, 063003; 2023.

[78] Fellner-Feldegg, H., The measurement of dielectrics in time domain. J. Phys. Chem., 73, pp. 616-623, 1969.

[79] Fellner-Feldegg, H. et Barnett, E.F., Reflexion of a voltage step from a section of transmission line filled with a polar dielectric. 74, pp. 1962-1965, 1970.

[80] R. H. Cole, Dielectric response by real time analysis of time domain spectroscopy data. J. Phys. Chem., 78, pp. 1140-1141, 1974.

[81] G. Moradi, A. Abdipour, Measuring the Permittivity of Dielectric Materials Using TDR Approach, Progress In Electromagnetics Research, PIER 77, pp.357–365, 2007.

[82] L. Chioukh, N.Bouzit,R. Delfouf, and D. Djouada , Etude comparative des propriétés dielectriques de composites hétérogènes (polymère/céramique) par spectroscopie temprorelle et banc de mesure en band X| 1er Séminaire National sur les Matériaux, Energie et Eaux: MEEAD'24, Sep 26, Jijel, Algeria 2024.

[83] L. Chioukh , N. Bouzit, and R. Delfouf, Microwave dielectric study of binary composite materials using high frequency x-band technique | Le 2ieme Séminaire International en Génie Industriel et Mathématiques Appliquées, Skikda,t, 24 Octobre, 2022.

[84] N. Bourouba, K. Lalla, J. P. Martinez Jimenez, and N. Bouzit, "Dielectric behavior of ternary mixtures: epoxy resin plus titanates ($MgTiO_3$, $CaTiO_3$, or $BaTiO_3$) associated with oxides (CaO, MnO_2, or ZnO)," *Eur. Phys. J. Appl. Phys.*, vol. 65, p. 10202, 2014.

[85] H. Khouni, N. Bouzit, J. P. Martinez Jiménez, and M. Bouamar, "Study of dielectric behavior of ternary mixtures of epoxy/titanates ($MgTiO_3$, $CaTiO_3$, $SrTiO_3$, and $BaTiO_3$) with carbon black," *Eur. Phys. J. Appl. Phys.*, vol. 76, p. 20201, 2016.

[86] M. Bouchaour, J. P. Martinez Jimenez, N. Bouzit, and N. Bourouba, "Dielectric behavior of a quaternary composite (RE, BT, MnO_2, CaO) in the band (DC–2 GHz)," *Eur. Phys. J. Appl. Phys.*, vol. 84, p. 10201, 2018.

[87] R. Delfouf, N. Bouzit, N. Bourouba, J. P. Martinez Jimenez, A. Brahimi, H. Khouni, and T. Arab, “Dielectric characterization and modeling of composite materials based on epoxy resin/black iron oxide/titanates in several frequency ranges,” *ECS J. Solid State Sci. Technol.*, vol. 11, p. 073006, 2022.

[88] O. Youssef, B. Seddik, B. Chrif, and H. Mohamed, “Dielectric properties of ceramic composite materials based on alumina reinforced by titanium carbide,” *FME Transactions*, vol. 48, no. 4, pp. 908–913, 2020.

[89] N. Jebbor, *Étude numérique et expérimentale de propriétés diélectriques de matériaux composites*, Thèse de Doctorat, Université Moulay Ismaïl, Maroc, 2014.

[90] A. Mejdoubi, *Étude par simulation numérique des propriétés diélectriques d'hétérostructures multiphasiques contenant des inclusions de forme arbitraire*, Thèse de Doctorat, Université de Bretagne Occidentale, France, 2007.

[91] D. Eberly, *Intersection of Ellipses*, Geometric Tools, Redmond, WA, USA, 2020.

[92] R. Chelghoum *et al.*, “Dielectric Behavior Characterization of RE/$BaTiO_3$ Using Time Domain Spectroscopy: Application on High-Performance Dielectric Resonator Antennas,” *ECS Journal of Solid State Science and Technology*, vol. 13, no. 4, p. 043018, 2024.

[93] L. Chioukh, N. Bouzit, and H. Khouni, “Dielectric behavior investigation of composite material based on Epoxy-BaTiO3: A comparative study of finite element numerical modeling and experimental results,” in *Proc. 1st International Conference on Technological of Materials (ICTAM'24)*, Oct. 30, 2024.

Publications and Communications

1. Publications:

[1] **L. Chioukh**, H. Khouni, and N. Bouzit, "The influence of filler particle size, concentration and distribution on dielectric properties of epoxy resin-ceramic composites using mixture laws," *Indian J. Pure Appl. Phys.*, vol. 63, no. 5, 2025. DOI: 10.56042/ijpap.v63i5.15087

[2] D. Djouada, N. Bouzit, R. Delfouf, **L. Chioukh**, and J. P. M. Jiménez, "Dielectric characterization of heterogeneous composites using time domain spectroscopy and microwave test benches in microwave frequency," *ECS J. Solid State Sci. Technol.*, vol. 12, no. 6, p. 063003, Jun. 2023. DOI: 10.1149/2162-8777/acdaf5

2. Communications

National:

[1] **L. Chioukh,** N.Bouzit,R. Delfouf, and D. Djouada , Etude comparative des propriétés dielectriques de composites hétérogènes (polymère/céramique) par spectroscopie temprorelle et banc de mesure en band X| 1er Séminaire National sur les Matériaux, Energie et Eaux: MEEAD'24, Sep 26, Jijel, Algeria 2024.

International:

[1] **L. Chioukh**, N. Bouzit, and H. Khouni, "Dielectric Behavior Investigation of Composite Material Based on Epoxy/ BaTiO3: A Comparative Study of Finite Element Numerical Modeling and Experimental Results,". *The 1st International Conference on Technological Applications of Materials*, 30 oct, Setif, 2024.

[2**] L. Chioukh**, N. Bouzit, and R. Delfouf, Microwave dielectric study of binary composite materials using high frequency x-band technique | Le 2ieme Séminaire International en Génie Industriel et Mathématiques Appliquées, Skikda, 24 Octobre, 2022.

Abstract

This thesis focuses on the analysis, characterization, and modeling of the dielectric properties of composite materials under quasi-static conditions. Two-dimensional simulations were performed using the finite element method on binary composites consisting of an epoxy resin matrix and ellipsoidal ceramic inclusions randomly distributed according to three statistical distributions (normal, log-normal, and Rayleigh). The study was conducted on three composites with distinct charge permittivities (ε_i = 80, 400, and 3600) by varying key parameters such as charge concentration, particle distribution, and particle size and morphology to assess the impact of each parameter on the overall effective permittivity of the material. The values obtained from the FEM simulation were compared to several classical and modified analytical models, allowing the identification of the most relevant distributions for predicting dielectric behavior. The results from this work offer essential elements for the optimization of materials for energy storage and conversion, sensors, and various electronic applications, by providing a thorough understanding of their performance before experimental realization.

Key words: characterization, modeling, dielectric, composite materials, quasi-static, finite element method, epoxy resin, ceramic, distributions.

Résumé

Cette thèse est consacrée à l’analyse, la caractérisation et la modélisation des propriétés diélectriques de matériaux composites en régime quasi statique. Des simulations 2D ont été réalisées à l’aide de la méthode des éléments finis sur des composites binaires constitués d’une matrice en résine époxy et d’inclusions céramiques ellipsoïdales réparties aléatoirement selon trois lois statistiques (normale, log-normale et Rayleigh). L’étude a été réalisée sur Trois cas de composites présentant des permittivités de charge distinctes (ε_i = 80, 400 et 3600) en changeant de paramètres clés tels que la concentration de la charge, la distribution des particules, ainsi que la taille et la morphologie des particules afin d’évaluer l’impact de chaque paramètre sur permittivité effective globale du matériau. Les valeurs obtenues par la simulation FEM ont été comparées à plusieurs modèles analytiques classiques et modifiés, permettant d’identifier les lois les plus pertinentes pour la prédiction du comportement diélectrique. Les résultats issus de ce travail offrent des éléments essentiels pour l’optimisation des matériaux destinés au stockage et à la conversion d’énergie, aux capteurs, ainsi qu’à diverses applications électroniques, en fournissant une compréhension approfondie de leurs performances avant leur réalisation expérimentale.

Mots clés: caractérisation, modélisation, diélectrique, matériaux composites, quasi-statique, méthode des éléments finis, résine époxy, céramique, distributions.

ملخص

تركز هذه الرسالة على تحليل وتوصيف ونمذجة الخواص العازلة للمواد المركبة في ظروف شبه ساكنة. أُجريت محاكاة ثنائية الأبعاد باستخدام طريقة العناصر المحدودة على مركبات ثنائية تتكون من مصفوفة راتنج إيبوكسي وشوائب سيراميكية إهليلجية موزعة عشوائيًا وفقًا لثلاثة توزيعات إحصائية (توزيع طبيعي، وتوزيع لوغاريتمي طبيعي، وتوزيع رايلي). أُجريت الدراسة على ثلاثة مركبات ذات سماحية شحنة مميزة80 ، و400، و3600 من خلال تغيير معلمات رئيسية مثل تركيز الشحنة، وتوزيع الجسيمات، وحجم الجسيمات وشكلها، لتقييم تأثير كل معلمة على سماحية المادة الفعالة الكلية. قورنت القيم الناتجة عن محاكاة العناصر المحدودة بالعديد من النماذج التحليلية الكلاسيكية والمعدلة، مما سمح بتحديد التوزيعات الأكثر ملاءمة للتنبؤ بسلوك المواد العازلة. تقدم نتائج هذا العمل عناصر أساسية لتحسين المواد المستخدمة في تخزين الطاقة وتحويلها، وأجهزة الاستشعار، والتطبيقات الإلكترونية المختلفة، من خلال توفير فهم شامل لأدائها قبل التنفيذ التجريبي.

الكلمات المفتاحية: توصيف، نمذجة، عازل، مواد مركبة، شبه ساكن، طريقة العناصر المحدودة، راتنج الإيبوكسي، سيراميك، توزيعات